FLOW CHARACTERIZATION INSIDE AIRWAYS WITH UNSTEADY BREATHING PATTERNS

By

MANIKANTAM G. GADDAM

B.E. in Mechanical Engineering
Osmania University
Hyderabad, TG, India
2014

M.S. in Mechanical and Aerospace Engineering
Oklahoma State University
Stillwater, OK, USA
2016

Submitted to the Faculty of the
Graduate College of the
Oklahoma State University
in partial fulfillment of
the requirements for
the Degree of
DOCTOR OF PHILOSOPHY
July, 2021

FLOW CHARACTERIZATION INSIDE AIRWAYS WITH UNSTEADY BREATHING PATTERNS

Dissertation Approved:

Dr. Arvind Santhanakrishnan

Dissertation Advisor

Dr. Khaled Sallam

Dr. Omer San

Dr. Yu Feng

Name: MANIKANTAM G. GADDAM

Date of Degree: JULY, 2021

Title of Study: FLOW CHARACTERIZATION INSIDE AIRWAYS WITH UNSTEADY BREATHING PATTERNS

Major Field: MECHANICAL AND AEROSPACE ENGINEERING

Abstract: Flow through human airways is characterized by unsteady flows, with flow separations at airway bifurcations. The oscillatory nature of airflow, unequal durations of inhalation time (IT), and exhalation time (ET) can facilitate gas exchange in higher generations of the human airway. Normal respiratory rate (RR) in adults ranges between 10-15 breaths per minute (bpm). RR varies in exercise conditions, mechanical ventilation strategies such as high-frequency oscillatory ventilation (HFOV), metabolic activities and pathological state to facilitate alveolar gas exchange. Previous studies characterized flows at steady inhalation and exhalation through airways. The individual effects of varying inhalation duration and breathing flow rate on flow through airways remains unknown. Our study focus on various unsteady breathing patterns inside idealized airway models. The goal of this study is to characterize the effects of unsteady internal airflow through idealized airway geometries. Various scenarios of unsteady breathing patterns were simulated in ANSYS 2020 R2 to characterize the fluid dynamics involved in such an unsteady airflow mechanism. The first study includes unsteady breathing patterns such as normal, moderate, and high-frequency ventilation with variation in inhalation time (IT) to breathing time (BT) ratio. The second study includes abnormal breathing patterns such as tachypnea ($\approx$ 1.5x increase in RR), bradypnea ($\approx$ 1.5x decrease in RR), hyperpnea (deep breathing with abnormally large peak flow rate), and hypopnea (shallow breathing with abnormally low peak flow rate); and final study includes single nostril inhalation as in yoga pranayama breathing techniques. Simulations were performed for each breathing pattern as in internal airflow studies. Our results showed that secondary flow was effective transport mechanism for flow inside idealized human airways. Airway local geometry plays a key role in flow distribution in higher generations. Discrepancy in the oscillatory flow relation $Re/Wo^2 = 2L/D$ (L = stroke length; D = trachea diameter) was observed for IT/BT $\neq$ 50%, as L changed with IT/BT. We developed a modified dimensionless stroke length term including IT/BT. While viscous forces and convective acceleration were dominant for lower Wo, unsteady acceleration was dominant for higher Wo. Time to peak jet length during inhalation increased with increase in breathing time. Single nostril and double nostril inhalation showed equal ventilation at higher generations in an idealized airway geometry.

TABLE OF CONTENTS

LIST OF TABLES

Table Page

Table Page

LIST OF FIGURES

Figure Page

Figure Page

Figure Page

NOMENCLATURE

Δp ..... Pressure drop
ν ..... Kinematic viscosity of air
θ ..... Breathing phase
A_{in} ..... Inlet area
A_N ..... Nostril inlet area
D ..... Tracheal diameter
d_i ..... Diameter of i^{th} generation
J_S ..... Jet streaming
L ..... Stroke length
L_j ..... Jet length
Q ..... Flow rate
R_1 ..... Instantaneous inhaled particle deposition
R_2 ..... Cumulative inhaled particle deposition
R_3 ..... Instantaneous exhaled particle ratio
R_4 ..... Cumulative exhaled particle ratio
Re ..... Reynolds number, $Re{=}VD/\nu$
Re_T ..... Tracheal Reynolds number, $Re{=}U_T D/\nu$
V, U_T .... Average tracheal velocity
Wo ..... Womersley number, $Wo{=}\frac{D}{2}\sqrt{\frac{2\pi}{\nu}}$

CHAPTER I

INTRODUCTION

Respiration is a combination of inhalation of oxygen rich air and exhalation of carbon dioxide rich air. Respiratory rate (RR) in humans ranges between 10-15 breaths per minute (bpm), and RR changes in conditions such as exercise, mechanical ventilation strategies such as high-frequency oscillatory ventilation (HFOV), and in diseases. In normal breathing, unequal durations of inhalation time (IT), exhalation time (ET), and the oscillatory nature of airflow facilitate the gas exchange in higher generations. Jan et al. (1989) developed a flow regime chart by relating the Womersley number (Wo) with the product of the ratio of stroke length (L) to hydraulic diameter (D) of the trachea. They have conducted experiments with oscillating breathing for various Reynolds numbers (Re with an equal ratio of inhalation and exhalation durations. Three sub-flow regimes were determined based on the regional effects of viscosity, unsteadiness, and convective acceleration. But, the fluid dynamic implications of altering inhalation time relative to the total breathing time (BT) remained fundamentally unclear.

Respiratory rate (RR) and depth (peak airflow rates) of breaths are controlled to facilitate gas exchange by chemical interactions within the neural system and malfunctions between them leads to disorders in breathing (Cherniack and Fishman, 1975). Dysfunctional or abnormal breathing patterns are used to describe such breathing disorders (Boulding et al., 2016). RR is an indication of human disease through involuntary nasal breathing (Cherniack and Fishman, 1975; Ott, 1912). However, humans can breathe through the nose or mouth, and a combination of both during illness and facilitate gas exchange at higher airway generations (Gilbert, 2014). Previous investigations showed an instance

of quick and less effort mouth breathing (Gilbert, 2014), or altered manipulated breathing (Tiller et al., 1987) as a response to these triggered breathing patterns. There are several breathing patterns, including eupnea (normal breathing (NC), RR_{NC} = 10-15 breaths per minute (bpm), tidal volume (TV_{NC}) = 350-650 mL and inhalation to breathing time (IT/BT) = 33.3%), tachypnea (TC, $RR_{TC} \approx$ 1.5 to 2x RR_{NC}), bradypnea (BC, $RR_{BC} \approx$ 1/(1.5 to 2)x RR_{NC}), hyperpnea (HC, $RR_{HC} = RR_{NC}$, $TV_{HC} > TV_{NC}$), hypopnea (SC, $RR_{SC} = RR_{NC}$, $TV_{SC} < TV_{NC}$)), and many other (refer to (Whited and Graham, 2019) for definitions and physiological details). Early evaluation of such abnormal breathing patterns aids clinicians in disease detection and failure to detect abnormal breathing patterns can even cause death (Whited and Graham, 2019). Studies investigating fluid dynamics of abnormal breathing patterns are essential to characterize lung ventilation.

Understanding the flow inside airways during the entire breathing cycle is important in particle deposition studies such as drug administration through inhalation in lung diseases (Patton and Byron, 2007; Kleinstreuer et al., 2014). Most particle deposition as in drug inhalation involves a breath-hold after inhalation (Haghnegahdar et al., 2018; Feng et al., 2015; Kleinstreuer and Feng, 2013*b*). Breathing patterns as in yoga also include breath-hold between inhalation and exhalation assuming to increase the chances of gas exchange. To what extend such breath-hold time affects the fluid dynamics inside the airways was never studied.

The goal of this study is to characterize the effects of unsteady airflow through airway. Unsteady-internal airflow exists during normal, abnormal, and diseased situations due to involuntary contraction and expansion of respiratory muscles. Besides, an individual can voluntarily alter the internal airflow by alternate nasal breathing like in yoga breathing techniques. The following dissertation was segregated based on the above scenarios and studied further.

Due to the complex geometry of the human airway, an idealized airway geometry was proposed by Weibel et al. (1963). In the current study, idealized human airway models

were designed based on the testing conditions, and simulations were performed. Computations were performed in ANSYS 2020 R2 to characterize the flow inside the airways in all unsteady internal flows. The results of this study provide a detailed fluid dynamic understanding of the effects of unsteady breathing during (a) normal, moderate, and high frequency oscillating ventilation, (b) abnormal breathing patterns, and (c) single-double nostril breathing with breath hold.

1.1 Specific Aims

The geometry of human airways varies with age, sex, and between individuals. Many studies considered simplified geometries (Weibel et al., 1963; Horsfield et al., 1971; Feng et al., 2016) with steady flows for both experiments and simulations. Flow inside the airways is complex, and such investigations through realistic geometries were few. The unsteady internal airflow through the airway decides the amount of ventilation to higher airway generations. The following specific aims (SAs) characterize the effect of unsteady flow through idealized airways.

- **SA 1: Effects of varying inhalation duration and respiratory rate on human airway flow.** Simple oscillating breathing velocity profiles were developed using known peak velocities, variable inhalation to breathing ratios (IT/BT) to generate normal, moderate, and HFOV breathing patterns. These velocity profiles were used to characterize the effect of IT/BT and breathing frequencies on airflow. All the conditions were simulated in ANSYS Fluent 2020 R2 using velocity profiles, with peak inhalation and exhalation at Re=4200, with breathing frequencies 10 bpm, 100 bpm and 1000 bpm. The current study showed secondary flow strength to be higher compared to axial flow strength in a breathing cycle. Variation of IT/BT ratio and its effect on regime map was discussed.

- **SA 2: Fluid dynamics of abnormal breathing patterns.** Normal breathing is a combination of effortless relaxation and contraction of chest and diaphragm mus-

cle moments. The airflow is relatively unsteady and constitutes a normal rhythmic pattern at 10-20 breaths per minute. However, physiological and pathological conditions can lead to abnormal breathing patterns. To investigate the lung ventilation in the disorders a parametric study was conducted varying the peak inhalation flow rates, peak exhalation flow rates, and breathing time in the idealized airway model. Jet length and jet streaming in various breathing patterns were measured. Our study showed that time to peak jet length during inhalation increased in inhalation phase with increase in breathing time.

- **SA 3: Unsteady oscillating breathing with breath-hold and alternate nostril-breathing techniques.** Breath-hold is common in most of the yoga techniques, intake of aerosol drugs, smoking, and many other applications. The current study aims to obtain the importance of such a breath-holding process during the inhalation at 6 s with 2 s breath-hold through single and double nostrils to replicate the yoga techniques. Three dimensional transient simulations were conducted in ANSYS Fluent 2020 R2 in idealized airway geometry with the standard nasal cavity. Single nostril breathing simulations showed lower oxygen deposition compared to double nostril breathing during breath hold. Velocity contours in upper trachea showed increased velocity at center of the sectional plane while the single left sided nostril breathing has peak velocity at right side. Future prospective studies on yoga breathing patterns were discussed.

CHAPTER II

LITERATURE

2.1 Airways

2.1.1 Geometry

Human airway is complex in geometry and varies from person to person (Kleinstreuer and Zhang, 2010). Either CT/ MRI images or specific geometric information was used to construct airway branches (Ma and Lutchen, 2009). Most commonly used geometry models are Weibel symmetry model (WSM) (Weibel et al., 1963), Weibel asymmetric model (WAM), Horsfield asymmetric model (HSM) (Horsfield et al., 1971) and subject specific airway configuration. Selection of geometry was mainly based on computational limitations, and also based on the study region of interest.

The most commonly used Weibel symmetry model consists of symmetric daughter branches with equal branch angles along sagittal plane (shown in Fig.2.1 A). Although it is an idealized airway model, it is easy to construct and use. While in the asymmetry model, the branching angle is asymmetric along sagittal plane. Patient specific airway configurations were mostly used to accurately predict the toxic and particle depositions aiming for the subject-specific treatments.

Lung models (Fig. 2.2) with various generations were developed by Lízal et al. (2010) for particle deposition, and flow analysis. In addition, these developed models permits comparison between numerical and experimental results. Lízal et al. (2010), suggested need for development of realistic lung models for measurement capabilities and for more accurate analysis. With the current technologies and manufacturing techniques, airways models

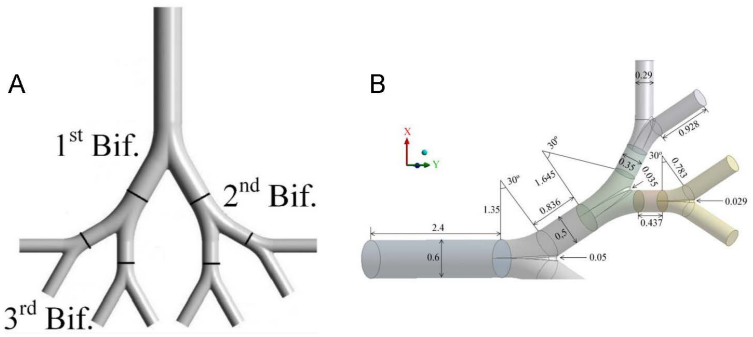

Figure 2.1: Symmetry airway model up to 4th generation (lengths in right side picture are in inches) (Augusto et al., 2016).

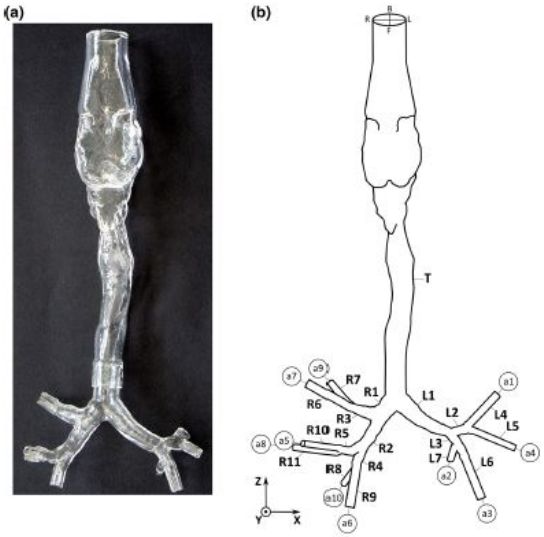

Figure 2.2: (a) Geometry of the realistic physical cast of the human airways. (b) Computational model of the respiratory tract with trachea (T), and left (L) and right (R) tracheobronchial trees and airway terminations a1–a10 (Elcner et al., 2016).

were 3D printed with nearly see through materials such as watershed material (Banko et al., 2015), machined acrylics, cast silicone for experimental studies. However each techniques for manufacturing has its own limitations.

2.2 Steady Flows and Particle Deposition

People breathe at low flow rates through nose that precludes from turbulence in the airway passage. However, air velocity changes on individuals inhalation/ exhalation pattern which changes due to temporary changes such as talking, eating and many more. Doorly et al.

(2008), found majority of inhaled air enters into middle and inferior regions of nasal cavity due to less obstacles. Secondary flows was observed in the middle part of nasal cavity. They found that flow through nasal cavity was influenced with parameters such as inflow conditions, airway geometry, size and orientation of internal nasal valve.

Lin et al. (2007), Zhang and Kleinstreuer (2002) found skewed velocity profiles at the curved portion from oral airway to pharynx due to the centrifugal force. Secondary flows are developed in oral airways because of abrupt geometry change. These secondary flows are more dominated during its passage through pharynx and larynx due to the uneven expansion and contraction of geometries. Turbulence can be felt due to oral inhalation but the intensity increases due to soft palate, decreases till the glottis and increases with glottis geometry. Finally, complex flows are developed in the oral airways and these propagate to bronchial airway. Turbulence formed at the throat disappears as it flow through trachea but instabilities are added again at the bifurcation due to change in geometries from parent to daughter airways (Kleinstreuer et al., 2008). As the airflow splits in the each daughter airway, boundary layers can be observed on the inner walls. Also velocity profiles are skewed in daughter tubes and flow in same generation daughter tubes can be different. Secondary flows were observed in daughter tubes and onset of them can be calculated using Dean number which depends on geometry of tube and the length of tube curvature. Womersely number determines the secondary flow fields and importance of unsteadiness in laminar oscillatory flows.

Studies with Weibel symmetric model showed (Zhang and Finlay, 2005) deposition of micro particles in direction of gravitational force and nano particles all over the airway model. Micro particle deposition was non-uniform on the airway model and nano particles deposited uniformly on the symmetric lung airway model. Nowak et al. (2003) simulated air-flow through generalized Weibel model and subject specific model for steady state inhalation, steady state exhalation and time-dependent breathing cycles. They concluded that Weibel model is insufficient in predicting aerosol deposition. So Weibel model is unrealis-

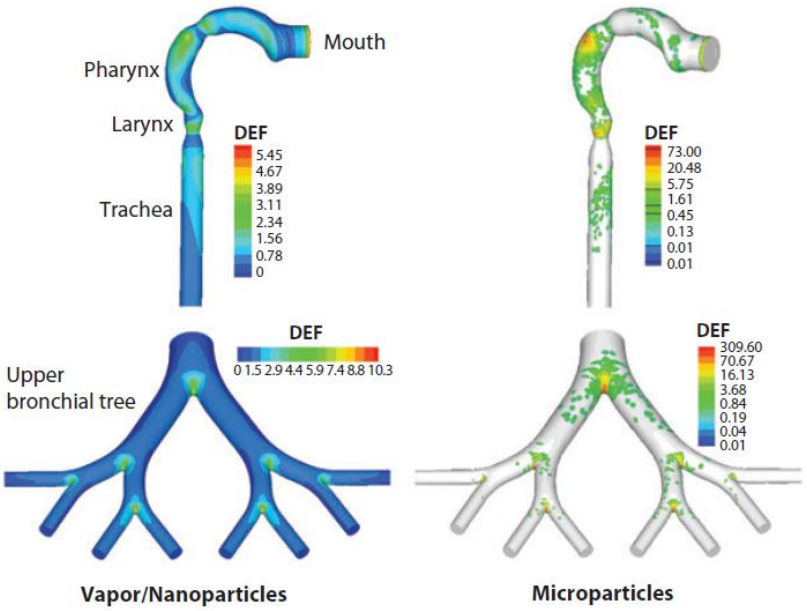

Figure 2.3: Nanoparticle and microparticle deposition in Weibel model Zhang and Finlay (2005).

tic and suggested Weibel asymmetric model for particle deposition studies.

Weibel asymmetric model approximates the real time airway geometry conditions and has a asymmetry in lung airway with lobes on either sides. Computations were performed to study the flow with range of Re 200-1600 corresponding to breathing rates of 0.27 -2.16 L/s of air. Liu et al. (2003) found that ratio of airflow rates through medial branches to that of parent branch remained constant and partially supported explanation of no change in human breathing due to different airway sizes.

Balásházy and Hofmann (1995) studied influence of asymmetry in bronchial branching such as asymmetric daughter branches diameter and asymmetry in branching angle. Asymmetric branch diameters showed no general trend in total deposition and the asymmetry in branching angle has greater influence in total deposition (Hofmann et al., 1995). However, these asymmetric models does not meet the requirements of human airway and investigations were started in patient specific models. In addition, advancements in the current computation technology patient specific models were been used to investigate drug particle inhalation and design an effective ventilator for a subject.

Kolanjiyil and Kleinstreuer (2017) found particle deposition to be more in alveoli compared to the upper thoracic cavity. In this study, a patient specific human airway was used up to 3 generations, it was modified future with triple bifurcation and alveoli sags were added to branches to obtain a whole lung model. Computations were performed on whole lung airway model with square wave breathing conditions mimicking inhale and exhale conditions at 15 L/min flow rate. 50,000 particles with 3 micron were injected at the oral inlet. This study was on spherical particles and real-time particle exposure includes non-spherical particles such as fibers, ellipsoidal, etc.

In Nicolaou and Zaki (2016), glass fiber deposition was experimented in a realistic human respiratory up to G7. Glass fibers of constant diameter, 1.03 ± 0.45 microns, were introduced in the model and deposition efficiency (ratio of number of deposited fibers in a specific region to number of fibers entering this region) was calculated. It was found that deposition efficiency increased with increasing particle stokes number due to impaction. Particles in the airway experience different flow time scales, motivates instantaneous stokes number as parameter to calculate deposition fraction instead of global stoke number. Computations on 90-degree mouth-throat simulations showed effective stokes number to be function of deposition efficiency (Belka et al., 2018)).

Pulmonary aerosol transport and its deposition was investigated by Islam et al. (2017) in deeper lung airways (up to 17 th generation) using Lagrange based Discrete Phase Model (DPM). Three flowrates (15, 30 and 60 L/min) with three spherical particle sizes (1, 5 and 10 micron) were used in computations and found that deposition percentage was more in the upper airways due to inertial impaction compared to deeper airways. Frederix et al. (2018), investigated size dependent poly-disperse aerosol (10 nm to 20 micron) deposition in a realistic cast of human upper airways and presented distribution on each generation for each aerosol size. Effective capturing of droplets was found in throat compared to other generations or airway structure. Feng et al. (2016), investigated multi-component droplet vapor mixtures in Weibel symmetry model with different puff topographies. They

saw secondary flows and dean type vortices in the model up to 3 generations. In addition at steady inhalation, stronger drawing lead to lower vapor and liquid deposition for all species of multicomponent vapor droplet aerosol mixture.

Aerosol transport studies were conduct by Lizal et al. (2012), using fluorometry and gravimetry. Fluorometry experiments were performed with di (2-ethylhexyl) sebacate(DEHS) vapours on fluorescein nuceli to compare results from other research. Results showed the limitations of DEHS particles for fluorometry due to fluorescence of impurities present in it.

Russo et al. (2008), simulated particle deposition in trachea and main bronchi with cartilaginous rings. Airway model was designed based on anatomical structures and 'D' shaped cross-section along the trachea.Computations were performed for 15, 30, 60 lpm's,at random and uniform particle distribution in ANSYS 2020 R2. All these studies are steady simulations and experiments, and studies with unsteady transient flow through airways effecting airflow fluid dynamics were limited.

2.3 Unsteady Pulmonary Flows

All the breathing patterns are realistically unsteady in nature, with higher peak exhalation compared to peak inhalation. The duration of inhalation/exhalation is about 2/3. Breathing is involuntary exapansion and contraction of lung muscles causing inhalation and exhalation. The normal breathing is about 10-20 bpm and this changes as per metabolic activity. We have characterized the unsteady internal pulmonary flows based on breathing frequency, breathing pattern and breath-hold parameters.

2.3.1 Breathing Frequencies

Based on breathing frequencies, three types of breathing patterns can be observed namely normal, moderate and high frequency ventilation condition. Große et al. (2007) analized steady and unsteady flow field in a realistic silicone model with first bifurcation. At steady

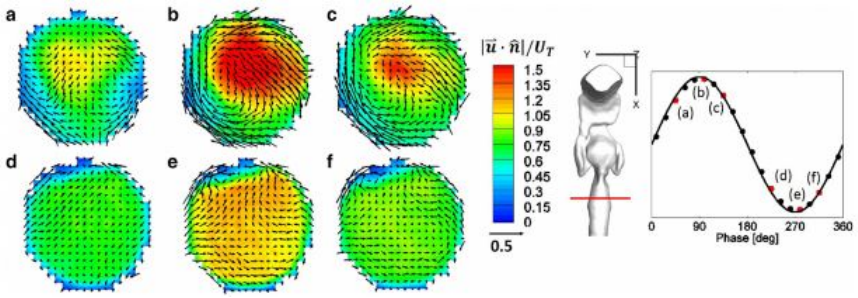

Figure 2.4: Flow in the trachea showing streamwise velocity contours with in-plane velocity vectors, normalized by the mean speed in the trachea. The view is looking downstream during inhalation with the posterior side of the model at the top of the figure and the anterior side of the model at the bottom of the figure. Selected phases are at 45 (a), 99° (b), 135° (c), 225° (d), 279° (e), and 315° (f). These correspond to the phases highlighted by the red squares . (For interpretation of the references to color in this figure legend, the reader is referred to the web version of this article) (Banko et al., 2015).

inspiration, flow was independent of Reynolds number while for unsteady inspiration, the critical Reynolds number (describes the onset of vortices in first bifurcation) decreased at higher Reynolds number. Numerical simulations were conducted on Horsfield asymmetric airway model for two breathing conditions, namely normal and maximal exercise condition were conducted by Calay et al. (2002). They found secondary motions to be stronger in the normal breathing conditions. In addition, they found separation regions near the carinal ridges for maximum exercise condition but not in the normal breathing condition.

Velocities in the airway network are low and decrease as the flow go deep into higher generations. Calay et al. (2002) stated that the maximum velocity found in any case would yield Mach number to be less than 0.1, ensuring incompressibility of air through airways making it viscous flow.

Banko et al. (2015), studied regime relevant to deep inspiration at steady inspiratory flow through anatomically accurate model of human airways. Mean velocity field was obtained using magnetic resonance velocimetry. It was found that, both stream-wise dispersion and secondary flows were effective transport mechanisms (Fig. 2.4) for flow in human airways.

To study the effect of unsteadiness, Soni and Aliabadi (2013) investigated particle de-

position using CFD simulations and released particles at different inhalation times. Results showed different particle deposition patterns for different particle release times. In addition, they found particle deposition increased with particles released in later phase of inhalation and geometry played a major role in the particle deposition.

Micro particle deposition during inhalation and the breath holding were simulated by Imai et al. (2012) in a airway model with sixth generation. They found increased deposition ratio for 5-micron particles and deposition further increased with increase in the breath holding time. Also, Darquenne et al. (2000) found that deposition of 1 micron particles was greater with longer breath holding in normal gravity compared with micro gravity.

Ramuzat and Riethmuller (2002), performed PIV investigations of Oscillating flows in 3D lung model to provide dynamic and temporal information on flow patterns. Effect of both Reynolds number and Womersley numbers on flow structure and boundary layer development in function of time was highlighted. Steady streaming displacement for a complete cycle showed that, particles, which are close to wall in trachea, have tendency to fall down and particle at the center of the tube at same height has the tendency to move up during a breathing cycle. In addition, particle in center of daughter tube has a tendency to move towards the wall whereas particle at same height near the bifurcation tend to stay at same place.

Flow through the human airway is characterized by regions of flow separation and the formation of secondary flow structures (Chen et al., 2014; Stylianou et al., 2016). The oscillatory nature of airflow can facilitate gas exchange in higher generations of the human airway (Chen et al., 2014; Jan et al., 1989). Normal respiratory rate (RR) in humans ranges between 10-15 breaths per minute (bpm). This RR increases during exercise and also in mechanical ventilation strategies such as high frequency oscillatory ventilation (HFOV) (Zhang and Kleinstreuer, 2002; Choi et al., 2010; Han et al., 2016). Further, inhalation time (IT) is about 45% of the total breathing time under normal breathing conditions (Zhang and Kleinstreuer, 2002). Characterizing the airflow inside the airways during the entire breath-

ing cycle is important in particle deposition studies such as for inhaled drug administration, and in lung diseases. Patton and Byron mentioned targeted drug delivery as a new method of treatment for diabetes, lung cancer, and many others. Training on inhaler holding, and inhalation techniques are common in clinical practice (Patton and Byron, 2007). Kleinstreuer et al. reviewed on target drug delivery and applications (Kleinstreuer et al., 2014). Preliminary studies conducted on subjects with COPD and asthma on proper inhalation of the prescribed drug showed improved health (Gregoriano et al., 2018) and increased aerosol deposition with increased inhalation time (Holsbeke et al., 2014). Kleinstreuer and Feng, reviewed on aerosol particle depositions (Kleinstreuer and Feng, 2013*b*,*a*). Many studies also have been conducted on e-cigarette depositions and can be found elsewhere (Haghnegahdar et al., 2018; Feng et al., 2015; Kleinstreuer and Feng, 2013*b*). Most of these particle deposition studies used steady flow rates for simulations and studies on unsteady flow rates are limited.

Regime relevant to deep inspiration was studied at steady inhalation flow through an idealized and anatomically accurate model of human airways and found that both streamwise dispersion and secondary flows were effective transport mechanisms for flow in human airways Banko et al. (2015, 2016). Unsteady physiological flow through subject-specific airways were investigated to measure the axial and lateral dispersion (defined by integral parameters) and compared against the idealized double bifurcation geometry (Jalal et al., 2020). Jalal et al. (2020) found asymmetric time dependent flow structures that were sensitive to local airway anatomy. Große et al. (2007) analyzed steady and unsteady flow field in a realistic silicone model with the first bifurcation using time-resolved particle image velocimetry; and found that at steady inspiration the flow was independent of Reynolds number and asymmetrical geometric bifurcation played a major role in flow streaming inside airways (Große et al., 2007). However, all these studies used simple oscillatory flow through airways with IT/BT = 50% and how do varying IT/BT ratios affect streamwise dispersion, and secondary flows were never investigated.

Jan et al. mapped flow regimes based on order-magnitude analysis onto a log-log graph to include various terms in axial flow and secondary momentum equations. They identified three flow regimes based on the regional domination of viscosity, unsteadiness, and convective acceleration Jan et al. (1989). Their flow regime map was developed by relating the Womersley number (Wo) with the product of the ratio of stroke length (L) to hydraulic diameter (D) of the trachea when using a sinusoidal breathing profile with IT/BT= 50% only. This map was developed to provide a) reference for what approach/solver might be used in modeling flow in airways b)investigate the fluid dynamic phenomena that affect the gas exchange at high frequency ventilation. To characterize the realistic fluid dynamics inside airways there is a need for a modified regime chart to include various IT/BT ratios.

HFOV was proposed by Lunkenheimer et al. (1972), to generate both active inspiration and expiration for eliminating entrained gas and decompress the gas in airway models. High-frequency oscillatory ventilation technique emerged to overcome the injuries caused due to conventional ventilation for patients with acute lung injury and acute respiratory distress syndrome (ARDS) (Chen et al., 2014). HFOV studies on airways showed changes in local air distribution and pressure variations at resonant frequency (Fredberg et al., 1984). They speculated to control lung ventilation by varying frequencies. Clinical studies on ARDS showed improved gas exchange with HFOV without compromise in oxygen delivery (Fort et al., 1997). Zhang et al. performed computations using realistic breathing pattern (Wo = 2.4) with IT/BT =46% and HFOV flow with IT/BT =50% and characterized fluid flow in fourth-generation airway (Zhang and Kleinstreuer, 2002). To what extent does active inspiration and expiration affect the air distribution in upper airways due to various breathing frequencies and the fluid dynamic implications of altering IT relative to total breathing time (BT), remains fundamentally unclear.

2.3.2 Abnormal Breathing

Breathing is controlled by neural system and the way we breathe changes with disease, and abnormalities. Jafari et al. (2010), aimed to design a system helping physicians in detection of abnormalities based on flow volume curves. They segregated unsteady breathing patterns into normal, obstructive, restrictive and mixed flow patterns with 97.6 % accuracy using neural network.

According to Whited and Graham (2019), breathing is controlled by neural system and regular breathing cycle originates in medulla. Different types of normal and abnormal breathing patterns (Fig. 2.5) include Eupnea (normal breathing), Sighing (an involuntary inspiration with 1.5-2 times higher tidal volume), Dyspnea (Subjective sensation of difficulty breathing), Apnea (Absence of breathing), Orthopnea (Patients incapable of breathing comfortably lying flat), Cheyne-Stokes (Cresendo- decrescendo respiration with period of apnea), Bradypnea (Respiration rate is lower than normal respiration of that age), Tachypnea (Respiration is higher than normal respiration of that age), Hyperpnea (increased volume without increased breathing rate), Agonal breathing (Slow and shallow irregular respirations because of anoxic brain), Hyperventilation (Over ventilation above needed for body expiration), Hypoventilation (under ventilation below needed for body expiration), Kussmaul respiration (Deep sighing respiratory pattern at a normal or slower rate), Biot respiratory pattern (Regular deep respiration interspersed with apnea), Apneustic breathing (this pattern is result of injury to the upper pons by stroke or trauma), and central neurogenic hyperventilation (breathing pattern caused by head trauma, severe brain hypoxia). All the above literature shows that flows in lungs are expected to be complex and does have a basic terminology of measurements.

Breathing in pathological conditions were studied by Grimby and Stiksa (1970) in obstructive lung disease patients. Twelve patients with obstructive lung disease were investigated to understand the flow volume curves and breathing patterns during exercise. They found higher flow volumes in higher exercise rate compare to at rest, or maximal expiration

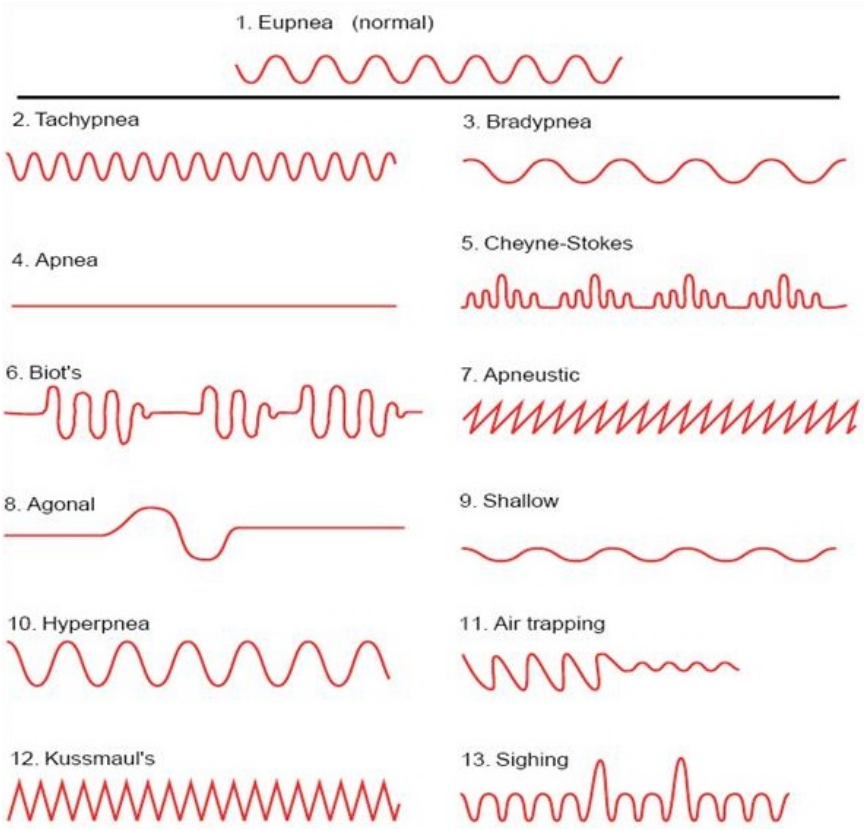

Figure 2.5: Important normal and abnormal breathing patterns (Med Care Tip©).

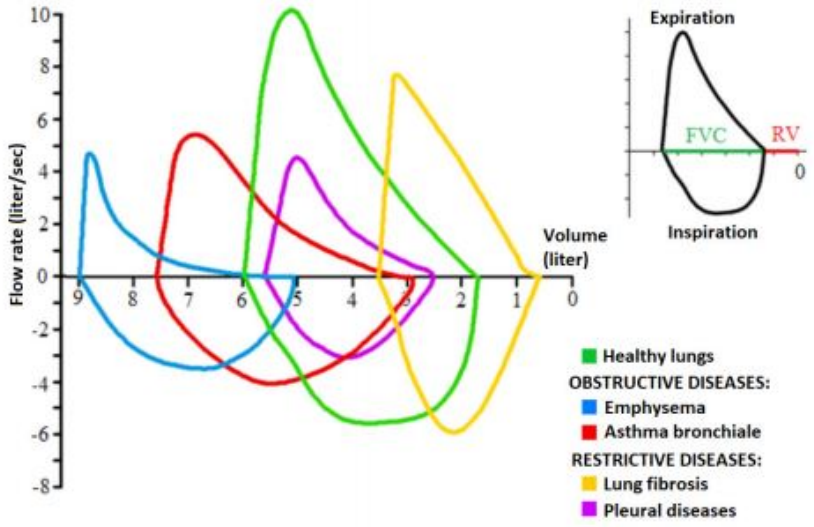

Figure 2.6: Flow-Volume loop (output of the spirometry) showing flow volume curve (FVC) manoeuvre for healthy and diseased lungs (Lizal et al., 2018).

flow volume curve. Lizal et al. (2018), observed variations of flow in human airways due to diseased conditions. Lung disease change shape of airways, influencing breathing pattern and so the particle deposition. A lung simulator was designed to investigate particle deposition under conditions such as asthma, emphysema and healthy lungs but no information is available on flow patterns and particle deposition. Lung flow volumes (Fig. 2.6) were obtained using the above studies of Choi et al. (2009), and Neves et al. (2015).

Patton and Byron (2007) mentioned targeted drug delivery as a new method of treatment for diabetes, Lung cancer etc., while information available on flow characterization of such realistic complex breathing patterns on particle deposition is limited. Realistic breathing patterns of abnormal breathing pattern plays crucial role in early detection of disease, need to be investigated on factors of gas exchange.

2.3.3 Breath Hold and Nasal Breathing

Studies suggested yogic exercises can support to withstand stress stimuli. Yoga is an ancestral philosophy from India, to integrate mind, soul and body. It is combination of both physical postures, breathing, and meditation (Barnes-Holmes et al., 2004). Yogic exer-

Figure 2.7: Representation of pranayama breathing performed with *nasika mudra* (hand posture) (Hakked et al., 2017).

cise such as pranayama, breathing exercise, is good to maintain proper health effecting the pulmonary function (Muktibodhananda, 2002), Taimni (1961), Saoji et al. (2019)).

Effects of pranayama were investigated in large number of individuals (Reddy et al., 2015; Panwar et al., 2012); to compare effects, between different yoga techniques of Suryanamakara and pranayama (Kondam et al., 2017, 2020), slow and fast pranayama (Dinesh et al., 2015), and benefits on lactate kinetics (Benavides-Pinzón and Torres, 2017). Effect of pranayama in COPD was investigated by Meenakshi (2017); Kaminsky et al. (2017). All these studies found better lung functioning with use of pranayama techniques. Hakked et al. (2017), found increased lung function with use of pranayama techniques in young swimmers.

Pranayama means control of prana, a vital life force or breath. Pranayama is combination of voluntarily controlled inhalation (puraka), breath hold (anthar kumbhaka) and exhalation (rechaka) (Reddy et al., 2015). *Puraka* helps to stimulate the system, *anthar kumbhaka* helps to distribute the air, and *rechaka* releases the vitiated air from the body (Sonne and Davis, 1982). Various number of Pranayama techniques are known, of which the current study investigates on Surya bhedan Pranayama (continuous breathing with inhalation through left nostril, followed by exhalation through left nostril), Nadi Shuddi Pranayama

(alternate left nostril breathing cycle and right nostril breathing cycles), Ujjayini Pranayama (inhalation through left nostril and followed by exhalation through right nostril in each cycle), and Anulom vilam Pranayama (inhalation through left nostril, followed by exhalation through right nostril, inhalation through right nostril followed by exhalation through left nostril and so on). All these studies were studied spirometry based, and how does the airflow inside such scenarios were never investigated.

2.4 Current Work

Current dissertation aims to address the effect of breathing frequencies with variations in inhalation to exhalation ratio in unsteady flows such as normal, moderate and high frequency oscillating ventilation strategies. In addition, unsteady parametric flow study was conducted at variable peak flow rates of inhalation, exhalation and breathing cycle duration to study the effects of abnormal breathing patterns and its implications on gas-exchange. Most of the clinical scanning techniques, yoga breathing techniques requests for a breath hold during the process. How do this breath hold effect the fluid flow, and oxygen deposition in the airways was investigated?

CHAPTER III

SA 1: EFFECTS OF VARYING INHALATION DURATION AND RESPIRATORY RATE ON HUMAN AIRWAY FLOW

3.1 Abstract

Studies of flow through the human airway have shown that inhalation time (IT) and secondary flow structures can play important roles in particle deposition. However, the effects of varying IT in conjunction with the respiratory rate (RR) on airway flow remain unknown. Using three-dimensional numerical simulations of oscillatory flow through an idealized airway model (consisting of a mouth, glottis, trachea, and symmetric double bifurcation) at a trachea Reynolds number (Re) of 4200, we investigated how varying the ratio of IT to breathing time (BT) from 25% to 50% and RR from 10 breaths per minute (bpm) corresponding to a Womersley number (Wo) of 2.41 to 1000 bpm (Wo = 24.1) impacts airway flow characteristics. Irrespective of IT/BT, axial flow during inhalation at tracheal cross-sections was non-uniform for Wo = 2.41, as compared to centrally concentrated distribution for Wo = 24.1. For a given Wo and IT/BT, both axial and secondary (lateral) flow components unevenly split between left and right branches of a bifurcation. Irrespective of Wo, IT/BT and airway generation, lateral dispersion was a stronger transport mechanism than axial flow streaming. Discrepancy in the oscillatory flow relation $Re/Wo^2 = 2L/D$ (L = stroke length; D = trachea diameter) was observed for IT/BT $\neq$ 50%, as L changed with IT/BT. We developed a modified dimensionless stroke length term including IT/BT. While viscous forces and convective acceleration were dominant for lower Wo, unsteady acceleration was dominant for higher Wo.

3.2 Introduction

Flow through the human airway is characterized by regions of flow separation and the formation of secondary flow structures (Chen et al., 2014; Stylianou et al., 2016). The oscillatory nature of airflow can facilitate gas exchange in higher generations of the human airway (Chen et al., 2014; Jan et al., 1989). Normal respiratory rate (RR) in humans ranges between 10–15 breaths per minute (bpm), corresponding to a Womersley number (Wo) range of 2.41–2.95 based on the following relation:

$$Wo = \frac{D}{2}\sqrt{\frac{\omega}{\nu}}, \tag{3.1}$$

where $\omega = 2\pi/\text{BT}$ is the angular frequency based on breathing time (BT, where BT = 60/RR seconds), D is the tracheal diameter, and ν is the kinematic viscosity of air. RR can be altered from the resting range of 10–15 bpm during exercise (such as walking RR = 20–60 bpm (Loring et al., 1990) and yoga RR = 3–7 bpm (Stancak Jr et al., 1991)), and also in mechanical ventilation strategies, such as high-frequency oscillatory ventilation (HFOV) (Zhang and Kleinstreuer, 2002; Choi et al., 2010; Han et al., 2016). Further, inhalation time (IT) is about 45% of BT under normal breathing conditions (Zhang and Kleinstreuer, 2002). Characterizing the airflow inside the human airway during the entire breathing cycle is important for understanding particle deposition characteristics in lung diseases (e.g., chronic obstructive pulmonary disease or COPD), during the use of e-cigarettes, and in inhaled drug therapy (Patton and Byron, 2007; Kleinstreuer et al., 2014). Previous studies of inhaled drug delivery in human subjects with COPD and asthma have shown improved respiratory outcomes (Gregoriano et al., 2018) and increased aerosol deposition with increased inhalation time (Holsbeke et al., 2014). However, computational fluid dynamics (CFD) studies examining particle deposition relevant to aerosols (Kleinstreuer and Feng, 2013*a*,*b*) and e-cigarettes (Haghnegahdar et al., 2018; Feng et al., 2015; Kleinstreuer and Feng, 2013*b*) typically consider either steady flow rates or only the inhala-

tion phase for simulations. Studies examining unsteady breathing patterns over an entire breathing cycle are limited.

The respiratory system consists of airways with complex geometrical cross-sections, including the nasal cavity (Lin et al., 2007; Borojeni et al., 2020), mouth, pharynx, larynx, glottis (Cheng et al., 1999), and the trachea that further bifurcates up to 16–23 Generations (G) (Choi et al., 2009) in addition to inter-subject geometry variability (Borojeni et al., 2020; Kleinstreuer and Zhang, 2010). Due to the geometrical complexity, idealized geometries of the nasal cavity (Liu et al., 2009), mouth-to-glottis section (Feng et al., 2016), and airway generations (Weibel et al., 1963; Horsfield et al., 1971) have been used in several studies. Weibel proposed an idealized airway geometry consisting of circular tubes at each generation (Weibel et al., 1963). This geometry bifurcated symmetrically along the sagittal plane and was able to capture key aspects of airflow and its features (Pedley et al., 1971; Grotberg, 2001). A review on using idealized airway models can be found elsewhere (Kleinstreuer and Zhang, 2010). In addition to airway geometry, head rotation and posture can also influence airway fluid dynamics. Idealized airway model studies have included mouth-to-glottis geometry in the sagittal plane that incorporate head rotation (Feng et al., 2016), and clinical studies of HFOV have reported prone positions to improve gas exchange, as compared to the supine position (Papazian et al., 2005). Finally, voluntary exercises, such as freestyle swimming and some yoga breathing techniques, can be conducted with head rotation (Walsh et al., 2008).

Previous studies examining the fluid dynamics of deep inspiration were conducted by prescribing steady inhalation flow through idealized (Jalal et al., 2016) and anatomically accurate physical models (Banko et al., 2015; Borojeni et al., 2020). Borojeni et al. (2020) recently used computational fluid dynamics simulations to establish physiological ranges of nasal airflow variables, and documented inter-subject variability. Steady inhalation studies with varying airflow parameters (such as Re, Wo) identified both axial (streamwise) and secondary (transverse) flow dispersion to be effective transport mechanisms (Jalal et al.,

2016; Banko et al., 2015). Unsteady physiological flow through subject-specific airways has also been experimentally investigated (Adler and Brücker, 2007; Große et al., 2007; Banko et al., 2016; Jalal et al., 2020). Jalal et al. (2020) found that with respect to idealized airway models (Jalal et al., 2016), realistic airway geometry produced stronger secondary flows, as well as increased axial and secondary flow dispersion. Secondary flows in realistic airways propagated deeper in the bronchial tree, and were stronger during exhalation as compared to inhalation (Jalal et al., 2020). Jalal et al. (2018) conducted magnetic resonance velocimetry (MRV) experiments on an idealized double bifurcation airway model across a range of Re and Wo in the convective region of the flow regime diagram of Jan et al. (1989). Strong secondary flows were observed for $Wo \geq 6$ during crossover from the inhalation to exhalation phase (Jalal et al., 2020). Große et al. (2007) conducted particle image velocimetry (PIV) measurements of steady and oscillating flows at the first bifurcation of an anatomical silicone model of the human airway. At steady inhalation, they found that the asymmetrical bifurcation promoted the formation of flow structures that were responsible for continuous axial transport to the lung (Große et al., 2007). Oscillating flow studies showed that the size of secondary flow structures strongly depended on the instantaneous values of Re and Wo (Große et al., 2007). Two-dimensional PIV measurements of oscillating flow through an asymmetric idealized model (based on (Weibel et al., 1963) and Horsfield et al. (1971)) at normal and HFOV conditions showed mass exchange at higher frequencies (Adler and Brücker, 2007). Experimental studies of HFOV flow through a subject-specific airway model (Soodt et al., 2011, 2013) reported homogeneous ventilation at higher generations with increasing RR (and hence Wo). However, the above studies of oscillatory flow through the human airway only considered IT/BT = 50%. While IT/BT varies in normal conditions and is not strictly equal to 50% (e.g., IT/BT = 46% (Zhang and Kleinstreuer, 2002)), IT/BT as low as 20% has been used in mechanical ventilation of patients with chronic obstructive pulmonary disease (COPD) and asthma (Ahmed and Athar, 2015; Boros et al., 1977; Loring et al., 1990). Further, breathing exercises that in-

volve voluntary manipulation of the normal rhythm (e.g., hatha yoga) also result in changes to IT/BT. The effects of varying IT/BT on axial dispersion and secondary flows currently remains unknown.

In terms of the physical mechanisms driving flow and gas exchange in different portions of the human airway, Jan et al. (1989) used order-of-magnitude analysis to examine the relative importance of various terms in axial flow and secondary momentum equations. Based on the regional domination of viscosity, unsteadiness, and convective acceleration, they developed a flow regime map by relating Wo^2 with the product of the ratio of stroke length (L) to hydraulic diameter (D) of the trachea when using a sinusoidal breathing profile with IT/BT = 50%. This map was developed to: (a) identify what approximation can be used in modeling flow in different regions of the airway; and (b) investigate the fluid dynamic phenomena that affect gas exchange in HFOV with equal inhalation and exhalation durations. To extend the applicability of their map to realistic breathing patterns in normal and HFOV conditions, this regime chart needs to be modified to account for variations in IT/BT.

HFOV was proposed by Lunkenheimer et al. (1972) to generate both active inspiration and expiration for eliminating entrained gas and gas decompression in airway models. The HFOV technique has since been used to overcome the injuries caused due to the use of conventional ventilation for patients with acute lung injury and acute respiratory distress syndrome (ARDS) (Chen et al., 2014). Fredberg et al. (1984) observed changes in local air distribution and pressure variations at resonant frequency with the use of HFOV, and speculated that lung ventilation can be controlled by varying frequencies. Clinical studies on ARDS patients have shown improved gas exchange with HFOV without compromise in oxygen delivery (Fort et al., 1997). Zhang and Kleinstreuer (2002) performed computations using realistic breathing patterns under normal conditions (Wo = 2.4) with IT/BT = 46% and HFOV (Wo = 23.3) with IT/BT = 50%, and characterized fluid flow in the fourth-generation airway. However, the extent to which active inspiration and expiration at larger

Wo (characteristic to HFOV) affect the flow characteristics in upper airways remains fundamentally unclear.

In this study, we examine the effects of varying *Wo* and IT/BT on airway flow characteristics. Three-dimensional (3D) computational fluid dynamics (CFD) simulations were performed by prescribing an oscillatory inflow profile in an idealized double bifurcation airway model (two generations) with a mouth-to-glottis section. The aims of this study were to: elucidate the flow physics under varying inhalation to breathing time, and modify the flow regime diagram of Jan et al. (1989) to incorporate effects of varying IT/BT.

3.3 Methods

An idealized airway model Weibel et al. (1963) with the addition of an idealized mouth-to-glottis section (previously used in a particle deposition study (Feng et al., 2016)) was designed in Solidworks (Dassault Systèmes SolidWorks Corporation, Waltham, MA) (Figure 3.1A). The airway includes the following: (i) a circular mouth-inlet of 20 mm diameter; (ii) a circular glottis of 8 mm diameter; (iii) a smooth trachea with a uniform, circular cross-section of 120 mm length and diameter (D) = 18 mm; and (iv) two generations (G) G1 and G2 of diameters 12.2 and 8.3 mm, respectively. The lengths of G1 and G2 were equal to 47 mm and 19 mm, respectively. All the bifurcation angles of the airway geometry were identically equal to 70°. The airway geometry was symmetric with respect to the coronal plane (defined along x-y Plane at $z = 0$ m, Figure 3.1A). Meshing was performed in ANSYS 2020 R2 by importing an STL geometry file into ICEM-CFD. The surface was modified to create parts such as an inlet, walls, and outlets using the angle method, and a material region was created. Octree mesh was created using minimum and maximum element sizes, along with curvature refinement. Walls were selected to generate prism layers with growth rate = 1.1, and volume mesh was computed. A total of three different meshes, each consisting of tetrahedral cells with five prism layers on walls, were generated for mesh independence tests. y_+ for all the meshes were <5, corresponding to peak velocity condition in the tra-

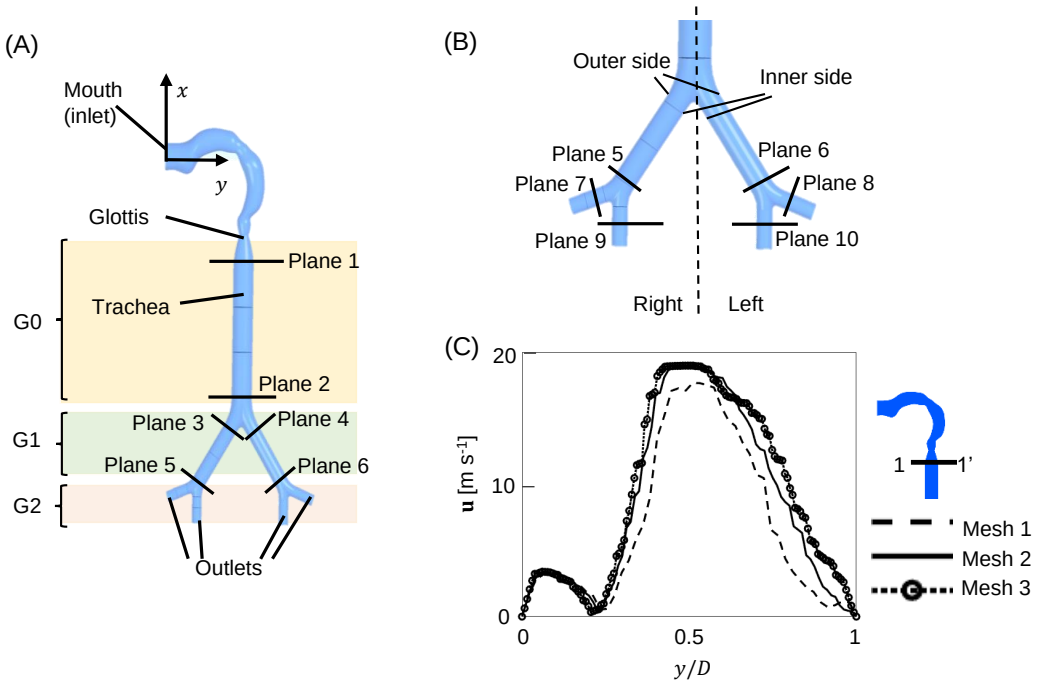

Figure 3.1: (A) Symmetric Weibel airway model with idealized mouth-to-glottis attachment. The coronal plane is defined along the x–y Plane at $z = 0$ m. Planes 1 and 2 comprise Generation 0 (G0), Planes 3–6 comprise Generation 1 (G1), and Planes 7–10 comprise Generation 2 (G2). See Table 3.2 for plane locations. (B) A magnified view of the bifurcations in G1 and G2 from Planes 5–10 is shown below, along with the anatomical left and right sides. $+z$-direction is into the page towards the dorsal (posterior) side; the $-z$-direction is out of the page towards the ventral (anterior) side. (C) 3D velocity ($\mathbf{u}$) was extracted at the upper trachea (line 1-1' at the coronal plane) and plotted as a function of non-dimensional diameter y/D for mesh independence tests (Table 3.1), where D = tracheal diameter = 18 mm.

chea. Previous studies have reported that $y_+ < 5$ in the glottis region and $y_+ < 1$ in the trachea are sufficient for resolving flow in the near-wall region when using the k-ω SST turbulence model (Zhang et al., 2009; Tu et al., 2012).

Three-dimensional CFD simulations of transient, incompressible flow through the above airway geometry were performed in ANSYS Fluent. k-ω SST turbulence model, used in previous studies of flow through the human airway (Cui and Gutheil, 2017; Zhang and Kleinstreuer, 2011), was chosen for all simulations in this study. Sinusoidal profiles were used as a simplified representation of realistic breathing waveforms (Choi et al., 2010). The

Reynolds number at the trachea during peak inhalation (Re_{T}) was defined as

$$Re_{\mathrm{T}} = \left(\frac{U_{\mathrm{T}}\, D}{\nu} \right), \tag{3.2}$$

where U_{T} is the mean flow speed in the trachea, ν is the kinematic viscosity of air (1.46 $\times$ 10^{-5} $\mathrm{m^2\ s^{-1}}$), and D is the tracheal diameter = 18 mm. Re_{T} was maintained constant in all breathing waveforms at Re_{T} = 4200, which is in the physiological range (Banko et al., 2015; Kleinstreuer and Feng, 2013*a*). The peak inhalation flow rate ($Q_{\mathrm{in,peak}}$) was determined using the relation:

$$Q_{\mathrm{in,peak}} = \frac{Re_{\mathrm{T}}\, \nu\, A_{\mathrm{T}}}{D}, \tag{3.3}$$

where ν is the kinematic viscosity of air (1.46×10^{-5} $\mathrm{m^2\ s^{-1}}$) and A_{T} is the cross-sectional area along the transverse cross-sectional Plane 2 with diameter D = 18 mm. Inhalation and exhalation volumes were kept equal for a given RR and IT. The peak exhalation flow rate ($Q_{\mathrm{ex,peak}}$) was defined based on IT, BT, and $Q_{\mathrm{in,peak}}$ using the equation below:

$$Q_{\mathrm{ex,peak}} = Q_{\mathrm{in,peak}} \left(\frac{\mathrm{IT}}{\mathrm{BT} - \mathrm{IT}} \right), \tag{3.4}$$

such that $Q_{\mathrm{ex,peak}}$ = $Q_{\mathrm{in,peak}}$ when IT = 0.5 BT, and $Q_{\mathrm{ex,peak}} < Q_{\mathrm{in,peak}}$ when IT $<$ 0.5 BT. Instantaneous profiles of inhalation velocity ($V_{\mathrm{in}}(t)$) and exhalation velocity ($V_{\mathrm{ex}}(t)$) were defined using the equations:

$$V_{\mathrm{in}}(t) = \frac{Q_{\mathrm{in,peak}}}{A_{\mathrm{in}}}\ \sin\left(\frac{\pi t}{\mathrm{IT}} \right),\ 0 < t \leq \mathrm{IT} \tag{3.5}$$

$$V_{\mathrm{ex}}(t) = \frac{Q_{\mathrm{ex,peak}}}{A_{\mathrm{in}}}\ \sin\left(\frac{\pi(\mathrm{IT} - t)}{\mathrm{BT} - \mathrm{IT}} \right),\ \mathrm{IT} < t < \mathrm{BT}, \tag{3.6}$$

where A_{in} is the area of the inlet. The above relations were used to develop nine oscillatory profiles of time-varying inflow velocity (**u**), prescribed perpendicular to the inlet,

and prescribed as initial conditions. The tests conducted here include three RRs (10 bpm, 100 bpm, and 1000 bpm (later being clinically impractical in adults)), each for IT/BT = 25%, 33%, and 50% (Loring et al., 1990; Shanholtz and Brower, 1994; Ahmed and Athar, 2015; Boros et al., 1977) to examine fluid dynamics across several orders of magnitude variation in *Wo*. We expect that our findings can inform future studies of low Reynolds number (*Re*) airway flows (such as in children), where HFOV is clinically used at higher frequencies than in adults (e.g., RR = 960 bpm in neonates (Varnholt et al., 1992; Yang et al., 2020)). All the oscillatory velocity profiles consisted of positive velocities for inhalation phases (θ from 0° to 180°) and negative velocities for the exhalation phase (θ from 180° to 360°).

Boundary conditions included zero pressures at the outlets and no-slip walls. To characterize the oscillatory flow relative to viscous effects, *Wo* was calculated for each condition using Equation (3.1), where $\nu = 1.46 \times 10^{-5}$ m^2 s^{-1} was used as the kinematic viscosity of air. U_T denotes mean flow speed in the trachea, and was calculated to be 3.4 m s^{-1} by equating flow rates at the inlet and the trachea via mass conservation for an incompressible flow:

$$U_\mathrm{T} = \left(\frac{V_\mathrm{in,peak}}{A_\mathrm{T}} \right) A_\mathrm{in}, \tag{3.7}$$

where $V_\mathrm{in,peak}$ is the peak inhalation velocity calculated from Equation (3.5).

After prescribing the velocity profile, each simulation was standard-initialized with initial x-velocity, y-velocity, and z-velocity to be equal to 0 m s^{-1}. Simulations were conducted at the High-Performance Computing Center at Oklahoma State University using 16 processor units. The solution method included a coupled scheme, and second-order spatial discretization. A uniform time-step of 10^{-3} s was used for running simulations for one breathing cycle. All the processing results were auto-saved at 12.5% inhalation time to maintain uniformity across all breathing frequencies and IT/BT ratios.

Mesh independence tests were performed on the airway model for different mesh sizes (Table 3.1) at a time-step of 10^{-3} s for HFOV velocity profiles (*Re* = 4200, *Wo* = 24.1,

Table 3.1: Mesh parameters used for mesh independence tests.

	Element size [m]	**Number of cells**	**Simulation time [min]**
Mesh1	1e-3	594,746	62
Mesh2	5e-4	2,550,857	118
Mesh3	3e-4	8,599,521	580

IT/BT = 50%) for one breathing cycle. This particular case was used in mesh independence tests to decrease the solution time. Three-dimensional velocity (**u**) was extracted from each converged simulation along a line 1-1' at the upper trachea in the coronal plane (z = 0 m; see inset in Figure 3.1C). Figure 3.1C shows the extracted velocity magnitude along the line 1-1' for Mesh 1 (dashed line), Mesh 2 (solid line), and Mesh 3 (dotted line with circle markers) as a function of non-dimensional diameter y/D, where D = 18 mm is the trachea diameter. The velocity of Mesh 2 was different compared to Mesh 1, as the smaller element size increased the spatial resolution. However, the spatial resolution of Mesh 2 was nearly the same as that of Mesh 3, but the simulation time of Mesh 3 was four times longer than Mesh 2, due to the larger number of cells. Since the velocity profiles at 1-1' for Meshes 2 and 3 were nearly identical (Figure 3.1C), Mesh 2 was selected for use in this study. In addition, the solution from each mesh study was analyzed further by measuring bulk velocity at a lower trachea (Plane 2). Average velocities of 3.4256 m s^{-1}, 3.4281 m s^{-1} and 3.4298 m s^{-1} was found, respectively, in mesh independence test simulations. Since the error in average velocity from Mesh 3 to Mesh 2 (0.05%) was less than the error between Mesh 3 and Mesh 1 (0.1%), Mesh 2 was selected for all simulations and time-step independence studies.

Time-step validation for higher Wo was conducted on the finalized Mesh 2. For time-step size validation, three different time-step sizes (0.0005 s, 0.001 s, and 0.00375 s) were used with inlet velocity profile corresponding to Re = 4200 and Wo = 24.1 at IT/BT = 50% with the same computational setup as described earlier. Velocity profiles were extracted from the completed simulations along the coronal plane in the upper trachea (Plane 1 in Table 3.2). The three velocity profiles showed no major variation at the center of the airway,

Table 3.2: Location of planes used for data analysis and corresponding sectional airway diameters.

Plane	Description	(X, Y, Z) [mm]	$(\theta_X, \theta_Y, \theta_Z)$ [°]	Diameter [mm]
Plane 1	Upper trachea (G0)	(-78, 0, 0)	(90, 0, 0)	18
Plane 2	Lower trachea (G0)	(-170, 0, 0)	(90, 0, 0)	18
Plane 3	Generation 1 (G1)	(-200, 65, 0)	(55, 35, 0)	12.2
Plane 4	Generation 1 (G1)	(-200, 82, 0)	(-55, 35, 0)	12.2
Plane 5	Generation 1 (G1)	(-238, 35, 0)	(55, 35, 0)	12.2
Plane 6	Generation 1 (G1)	(-238, 108, 0)	(-55, 35, 0)	12.2
Plane 7	Generation 2 (G2)	(-244, 24, 0)	(20, 70, 0)	8.3
Plane 8	Generation 2 (G2)	(-244, 120, 0)	(-20, 70, 0)	8.3
Plane 9	Generation 2 (G2)	(-250, 32, 0)	(90, 0, 0)	8.3
Plane 10	Generation 2 (G2)	(-250, 110, 0)	(90, 0, 0)	8.3

with minor differences in near-wall velocity (see Figure S1 in Supplementary Materials). As the error in velocity prediction was better in δt = 0.001 s when comparing δt = 0.00375 s and simulation time for δt = 0.001 s was lower compared to δt = 0.0005 s, the time-step of δt = 0.001 s was used for all the simulations reported in this study.

Steady inhalation with similar boundary conditions, as described for transient simulations, were simulated at inlet flow rates of 10, 15, 30, 45, and 60 L min^{-1}. Pressure drop (Δp) was estimated for both validation (steady flow simulations) and varying *Wo* and IT/BT (transient flow simulations) in ANSYS Fluent.

Solution files from ANSYS Fluent were imported to ANSYS CFD-POST for further analysis and generating results. All *Wo*-tested, velocity magnitude contours were extracted along the planes in Table 3.2 and visualized in Tecplot 360 (Tecplot Inc., Bellevue, WA, USA). The *Q*-criterion previously used in a study of steady airflow through a similar geometry (Cui and Gutheil, 2017) was used to identify flow vortex structures at various breathing conditions. Q = 100,000 s^{-2} was used for isosurfaces at peak inhalation, and Q = 15,000 s^{-2} was used for isosurfaces at peak exhalation.

Integral parameters (I_1, I_2) have been used in previous studies of flow through the human airway to examine the relative importance of axial flow streaming and lateral dispersion mechanisms (Banko et al., 2016; Jalal et al., 2016). Axial (i.e., streamwise direc-

tion) flow uniformity at a cross-sectional plane was quantified using the integral parameter I_1 (Banko et al., 2016; Jalal et al., 2016):

$$I_1 = \left(\frac{\iint_A (\mathbf{u} \cdot \widehat{\mathbf{n}})^2 dA}{U_T^2 A} \right)^{1/2}, \tag{3.8}$$

where $\mathbf{u}$ is the 3D velocity field for a specific phase-point in the cycle, $\widehat{\mathbf{n}}$ is the unit normal vector at a given cross-section of the airway, and A is the cross-sectional area. Lateral dispersion arising on account of secondary (i.e., transverse direction) flow at a cross-sectional plane was quantified using integral parameter I_2 (Banko et al., 2016; Jalal et al., 2016):

$$I_2 = \left(\frac{\iint_A \|\mathbf{u} - (\mathbf{u} \cdot \widehat{\mathbf{n}})\hat{\mathbf{n}}\|^2 dA}{U_T^2 A} \right)^{1/2}. \tag{3.9}$$

I_1 and I_2 were calculated to examine the effects of varying Wo and IT/BT at G0, G1 and G2 (Figure 3.1A, Table 3.2).

3.4 Results

3.4.1 Model Validation

We conducted steady flow simulations to compare with published results from studies of idealized, as well as subject-specific airway models (Rahimi-Gorji et al., 2016; Gemci et al., 2008; Qi et al., 2017). A pressure drop in the airway as a function of the inhalation flow rate is shown in Figure 3.2A, comparing the results of our simulations with those of previous CFD studies that considered a whole airway model (Rahimi-Gorji et al., 2016) and upper airway truncated models (only including the trachea and higher generations) (Gemci et al., 2008; Qi et al., 2017). From the steady flow simulations of our idealized airway model, a pressure drop was observed to increase with an increasing inhalation flow rate. The trend of pressure drop variation with inhalation flow rate was comparable to those reported in previous studies. When compared to previous studies, our results showed a higher pressure

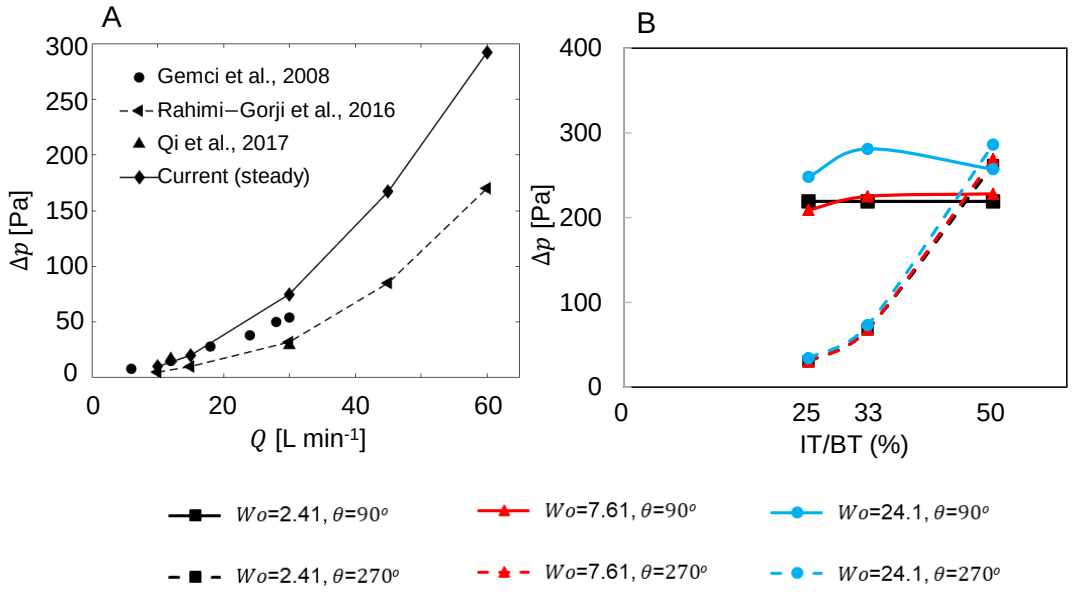

Figure 3.2: (**A**) Airflow rate (Q) vs. pressure drop (Δp) in airway models from previous studies and current steady state (diamond markers) simulations for model validation. (**B**) Pressure drop (Δp) in airways at peak inhalation and peak exhalation for various Wo and IT/BT conditions from transient simulations in this study. $\theta = 90^{\circ}$ indicates peak inhalation, and $\theta = 270^{\circ}$ indicates peak exhalation.

drop at larger inhalation flow rates. Variation in pressure drop values between the studies are most likely caused by the use of different airway geometries. Pressure drop (Δp) in airways at peak inhalation ($\theta = 90^{\circ}$) and peak exhalation ($\theta = 270^{\circ}$) are shown in Figure 3.2B for different Wo and IT/BT conditions. For a given Wo, the pressure drop remained almost the same in all IT/BT ratios at peak inhalation, while the pressure drop increased with increasing IT/BT at peak exhalation. In addition, with increase in Wo, a pressure drop at peak exhalation remained constant for the given IT/BT ratio. For a given IT/BT ratio, with an increase in Wo, the pressure drop at peak inhalation remained constant from Wo = 2.61 to 7.61 and later increased at Wo = 24.1.

3.4.2 Inhalation Flow Fields with Varying Breathing Frequency

Figure 4.2 shows the detailed view of the flow field at different planes along the trachea (G0) and G1 specified in Table 3.2. Flow at each planar location is visualized via contours of plane-normal (i.e., axial) velocity magnitude (non-dimensionalized by U_{T}) overlaid with

velocity vectors of secondary (i.e., transverse direction) flow at various instants of inhalation (A = early inhalation; B = peak inhalation; C = late inhalation). All the contours are shown from the top view, such that Planes 1 and 2 are parallel to Plane y–z, and Planes 3 and 4 are rotated locally to show the perpendicular views.

The presence of a jet in the trachea can be seen through the coronal, increasing in strength from the start of inhalation until peak inhalation ($\theta = 90^\circ$) and later decreasing until the end of inhalation ($\theta = 180^\circ$). A strong jet core was observed throughout inhalation (refer Movie SA1.1). Additionally, the jet core was concentrated towards the ventral side of the trachea at Phase A, moved towards the dorsal side at Phase B, and returned towards the ventral side at Phase C. Compared to Plane 1, axial flow magnitude was lower at Planes 2 to 4. Similar to Plane 1, axial flow at Planes 2 to 4 increased in strength until peak inhalation and later decreased in strength. Irrespective of the specific inhalation phase, secondary flow was strongest at Plane 1. At Plane 4, secondary flow vectors opposite to that of Plane 3 were observed during all phases (A to C). Stronger axial velocity at Plane 3 compared to Plane 4 (both at peak inhalation) shows axial flow is asymmetrically distributed after the first bifurcation.

Non-dimensional axial velocity contours and secondary flow fields are shown in Figure 4.3 for $Wo = 24.1$ at IT/BT = 25% at various instants of inhalation for Planes 1–4. Flow in Plane 1 showed uniform axial flow at the beginning of inhalation (Phase A), and centrally concentrated axial flow at peak inhalation (Phase B) and late inhalation (Phase C). The secondary flow at Plane 1 moved toward the left of the trachea from peak inhalation to late inhalation. Additionally, at Plane 1, axial flow in the coronal plane increased in strength from Phase A to Phase B, followed by a decrease in strength until Phase C. Axial flow at Plane 2 was uniform throughout inhalation with increased secondary flow velocity vectors from early inhalation until peak inhalation. Secondary flow at Plane 2 was directed from the dorsal and ventral sides and directed outward towards the left and right side of the trachea across inhalation. Planes 3 and 4 showed similar magnitudes of axial flow veloci-

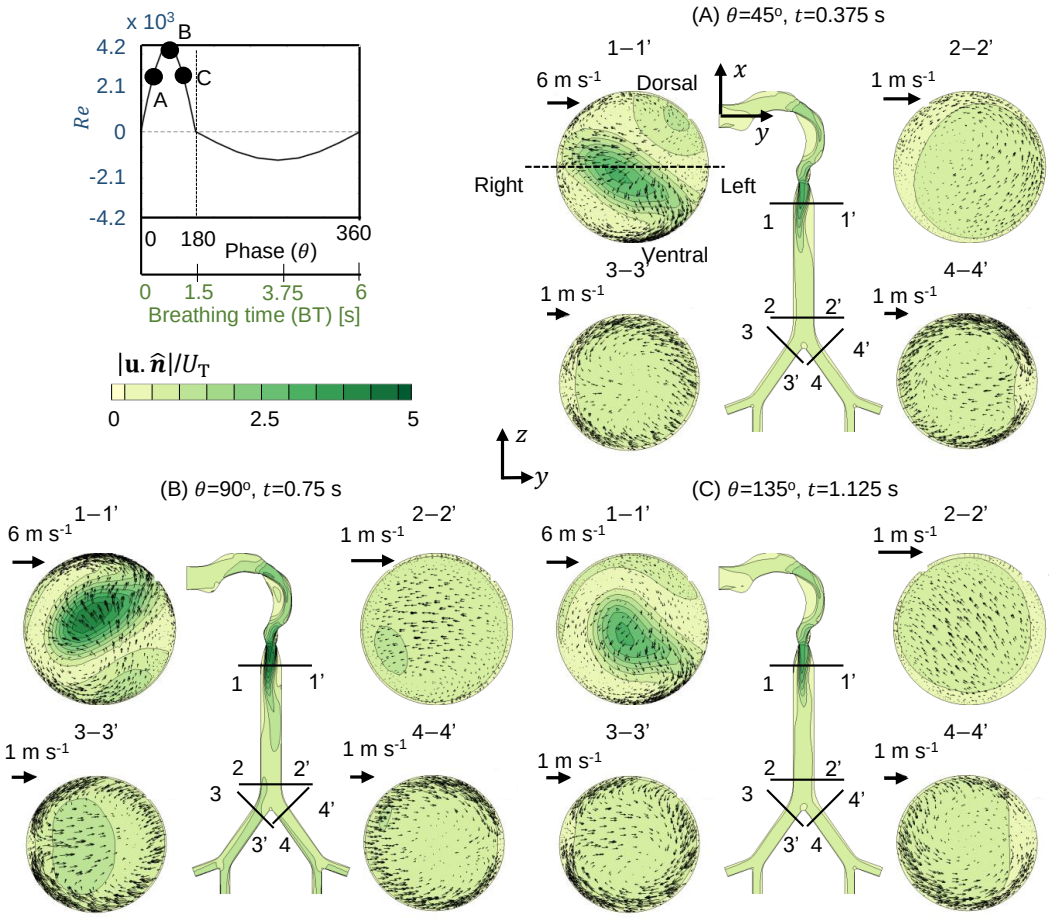

Figure 3.3: Contours of magnitude of the plane-normal velocity component (nondimensionalized with mean flow speed in trachea, U_T) with superimposed in-plane velocity vectors for Planes 1–4 at various time-points during inhalation for Wo = 2.41 at IT/BT = 25%. A is at Phase $\theta = 45^\circ$ (= 25% IT), B is at Phase $\theta = 90^\circ$ (= 50% IT), and C is at Phase $\theta = 135^\circ$ (= 75% IT). Views for Plane 3 and Plane 4 were rotated at 35° and −35°, respectively, viewed perpendicular to each plane. The reference vector for in-plane velocity components is shown for each plane.

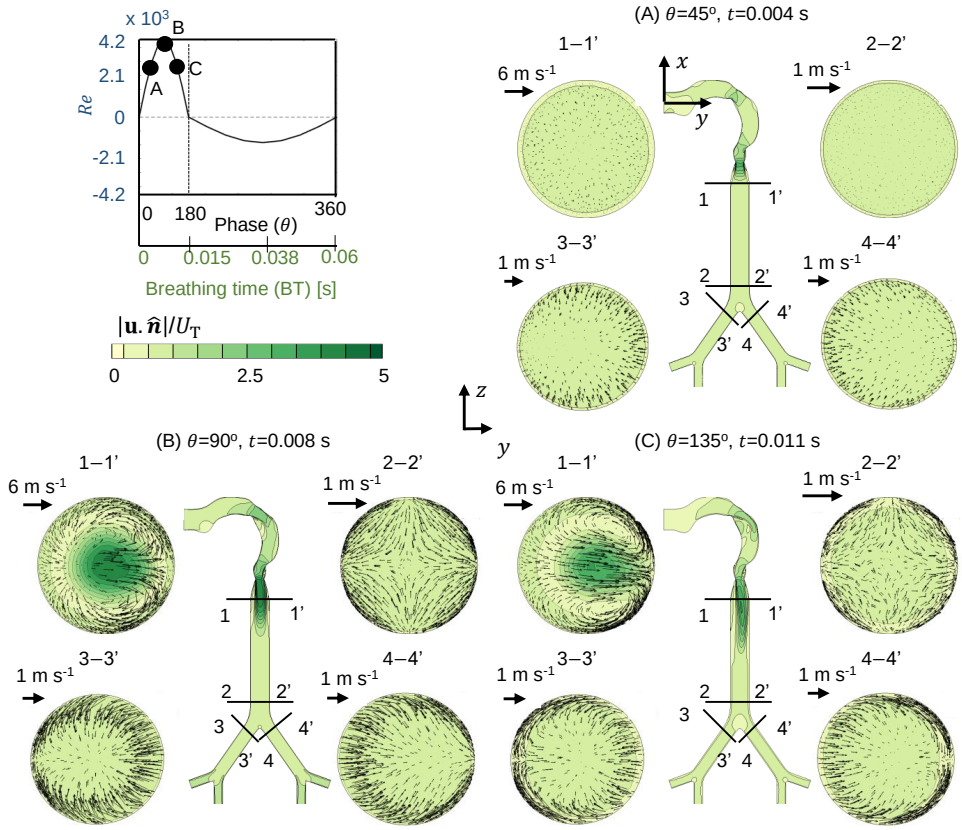

Figure 3.4: Contours of magnitude of plane-normal velocity component (nondimensionalized with mean flow speed in trachea, U_T) with superimposed in-plane velocity vectors for Planes 1–4 at various time-points during inhalation for Wo = 24.1 at IT/BT = 25%. A is at Phase $\theta = 45°$ (= 25% IT), B is at Phase $\theta = 90°$ (= 50% IT) and C is at Phase $\theta = 135°$ (= 75% IT).

ties during phases A to C. Flow separation zones at Planes 3 and 4 can be observed due to airway bifurcation at late inhalation (Phase C).

At IT/BT = 25%, for both Wo = 2.41 and Wo = 24.1 conditions, strong axial flow (refer Figures 4.2,4.3) and strong secondary flow were observed in the trachea at Plane 1. Increase in Wo weakened axial flow across Planes 1 and 2 during early inhalation (Phase A), while at peak inhalation, Plane 1 showed similar velocity magnitude even with an increase in Wo. During peak inhalation (Phase B) and late inhalation (Phase C) at Plane 1, axial flow was concentrated near the center of the airway at Wo = 24.1, as opposed to asymmetric distribution at Wo = 2.41. During peak inhalation (Phase B) at Planes 3 and 4, axial flow was stronger near the inner wall of the bifurcation for Wo = 2.41, as

compared to uniformly distributed axial flow for Wo = 24.1 (discussed later under velocity profiles). Across the inhalation phases considered for analysis, non-uniform axial flow distribution was observed along Planes 1–4 for Wo = 2.41. In contrast, axial flow appears to be uniformly distributed at Planes 1–4 during Phase A; centrally concentrated at Plane 1 during Phase B; and uniformly distributed for Planes 2–4 across phases B and C for Wo = 24.1. For Wo = 2.41 and IT/BT = 25%, axial flow at peak inhalation at Plane 3 was higher compared to Planes 2 and 4, while in Wo = 24.1, flow through Planes 3 and 4 was equal, and was higher compared to Plane 2 (discussed later under integral parameters).

3.4.3 Exhalation Flow Fields with Varying Womersley number

Figure 3.5 shows nondimensional axial velocity magnitude contours overlaid with secondary flow fields during exhalation at Planes 1-4 for $Wo = 2.41$ at IT/BT = 25%. The coronal planes showed strong axial flow in mouth-to-glottis section with maximum axial velocity magnitude at Phase B. Uniform axial flow and non-uniform secondary flow can be observed across all planes during exhalation time (ET). Weak secondary flow was observed during exhalation at Plane 1 for $Wo = 2.41$ at IT/BT = 25%. Multiple counter-rotating zones of secondary flow were observed near the wall at Plane 2 during all three phases of exhalation (D, E, F). Exhalation flow at Planes 3 and 4, located in a higher generation (G1) of the airway, show similar secondary flow fields from Phase D ($\theta = 225^{\circ}$, 25% ET) until Phase F for $Wo = 2.41$ (IT/BT = 25%).

Figure 4.4 shows nondimensional axial velocity magnitude contours overlaid with secondary flow fields during exhalation at Planes 1–4 for Wo = 24.1 at IT/BT = 25%. Compared to exhalation flow in the mouth-to-glottis section for Wo = 2.41 at IT/BT = 25%, weaker axial flow can be observed for Wo = 24.1 at the same IT/BT (refer Movie SA1.1,1.3). At Plane 1 of Wo = 24.1 at IT/BT = 25%, the region of strong axial flow (near anatomical right) at Phase D decreased in size with increasing time until Phase F. In addition, two rotational secondary flow fields were observed at early exhalation (Phase D) until peak

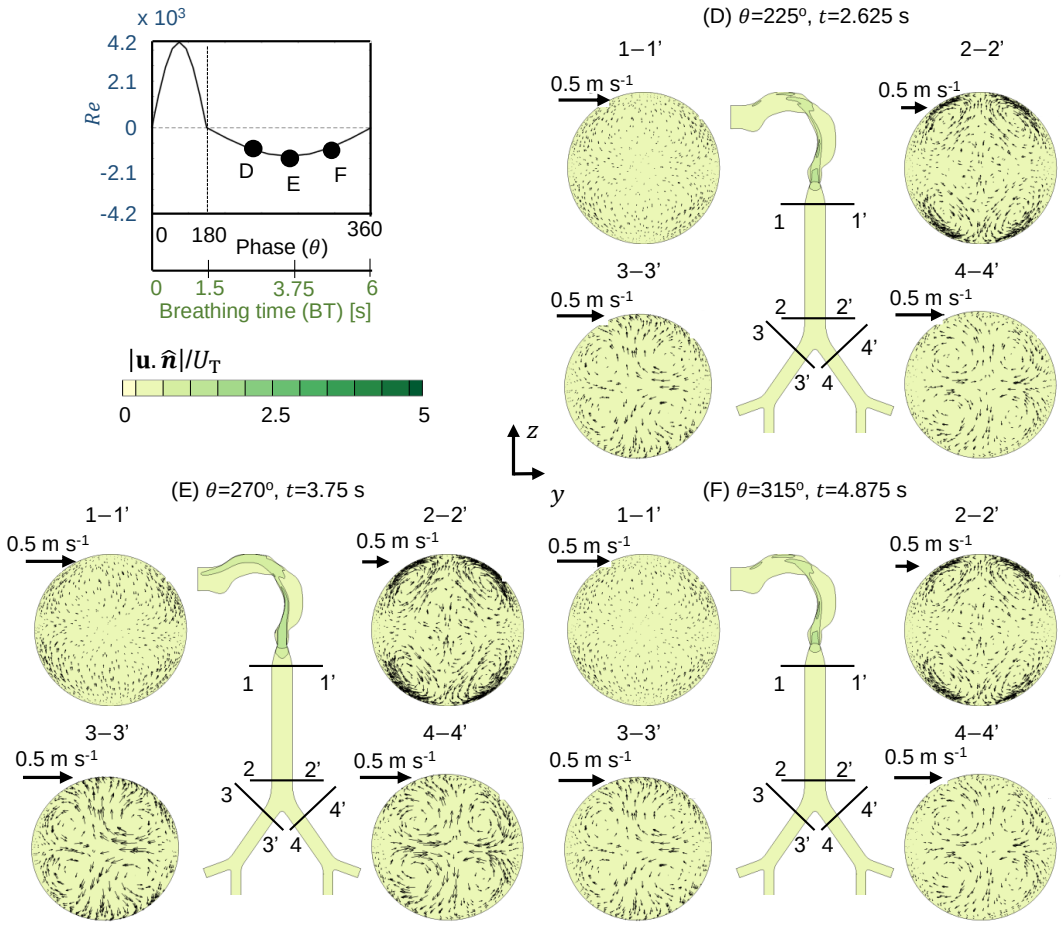

Figure 3.5: Contours of magnitude of a plane-normal velocity component (nondimensionalized with mean flow speed in trachea, U_{T}) with superimposed in-plane velocity vectors for Planes 1–4 at various time-points during exhalation for Wo = 2.41 at IT/BT = 25%. D is at Phase $\theta = 225^{\circ}$ (= 25% ET), E is at Phase $\theta = 270^{\circ}$ (= 50% ET) and F is at Phase $\theta = 315^{\circ}$ (= 75% ET).

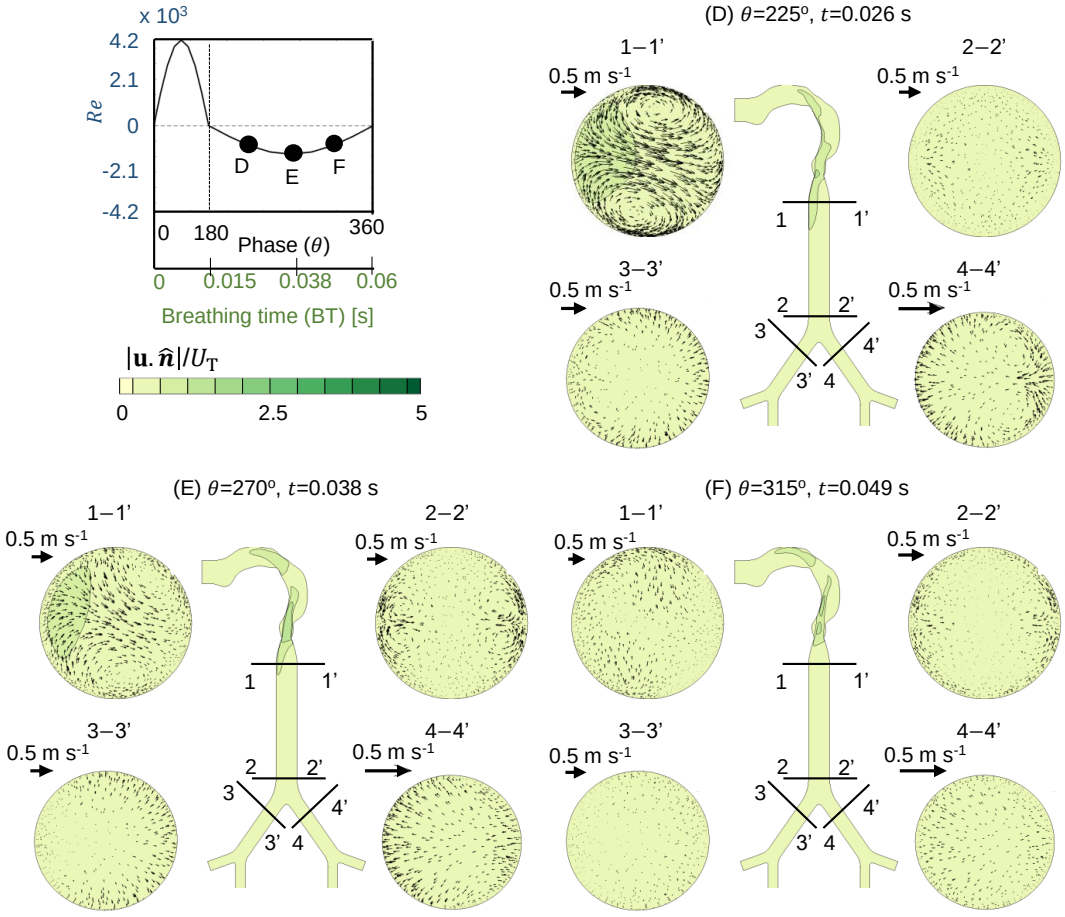

Figure 3.6: Contours of magnitude of plane-normal velocity component (nondimensionalized with mean flow speed in trachea, U_T) with superimposed in-plane velocity vectors for Planes 1–4 at various time-points during exhalation for Wo = 24.1 at IT/BT = 25%. D is at Phase θ = 225° (= 25% ET), E is at Phase θ = 270° (= 50% ET) and F is at Phase θ = 315° (= 75% ET).

exhalation (Phase E), while at Plane 2, secondary flow was initially weak at Phase D, increased at Phase E, and later decreased until late exhalation (Phase F). As compared to Planes 1 and 2, secondary flow was weakened at Planes 3–4 throughout exhalation for Wo = 24.1 at IT/BT = 25%.

3.4.4 Inhalation and Exhalation Flow Fields with Varying IT/BT

Figure 4.5 shows the detailed view of the flow field at Planes 1–2 (trachea, G0) and Planes 3–4 (G1) for Wo = 2.41 and IT/BT = 50%. The coronal planes showed an increase in

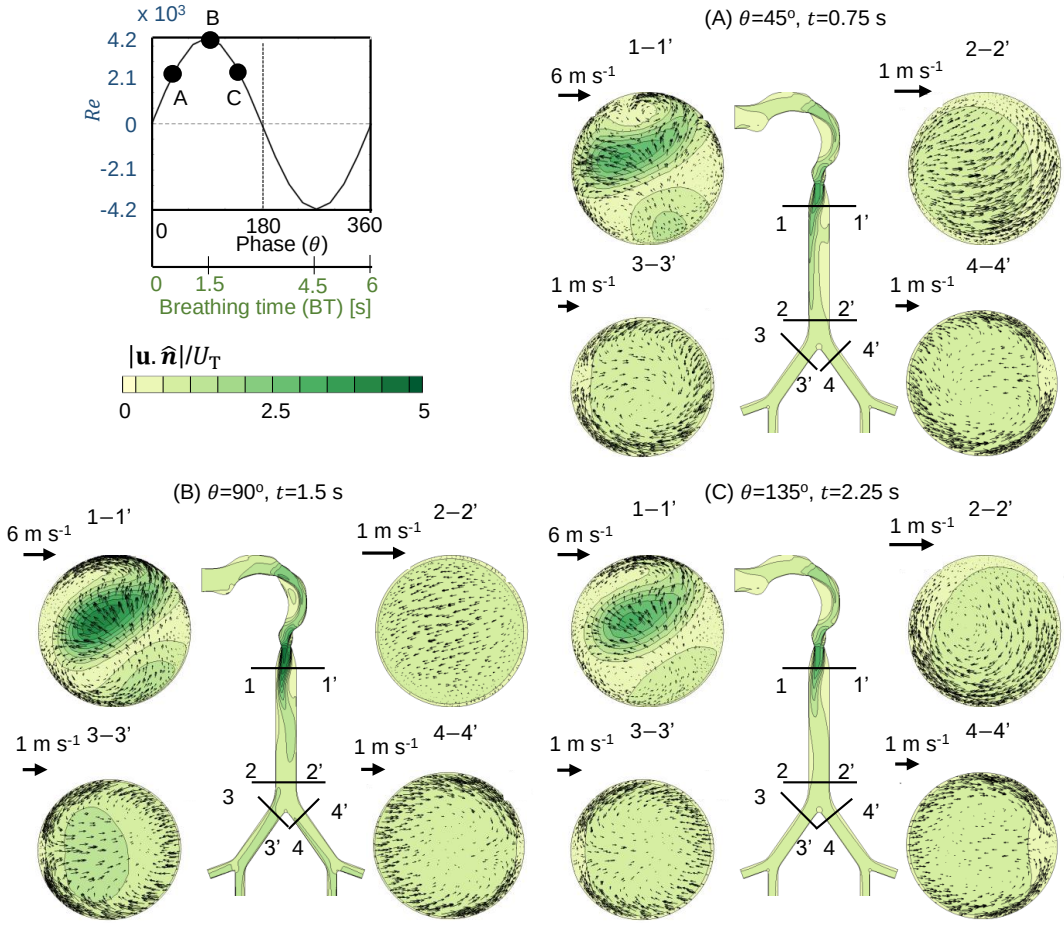

Figure 3.7: Contours of magnitude of the plane-normal velocity component (nondimensionalized with mean flow speed in trachea, U_T) with superimposed in-plane velocity vectors for Planes 1–4 at various time-points during inhalation for Wo = 2.41 at IT/BT = 50%. A is at Phase $\theta = 45^\circ$ (= 25% IT), B is at Phase $\theta = 90^\circ$ (= 50% IT), and C is at Phase $\theta = 135^\circ$ (= 75% IT).

axial velocity from Phase A until Phase B, and later decreased at Phase C. Compared to Planes 2–4, Plane 1 showed stronger axial velocity magnitude and secondary flow at each inhalation phase. Further, the strong axial flow region was located near the right-dorsal side of Plane 1 during inhalation. At Plane 2, axial velocity magnitude increased until peak inhalation (Phase B) and later decreased at Phase C. The strong axial flow region at Plane 2 was located near the ventral side (bottom of contour) for phases A and C and uniformly distributed during peak inhalation (Phase B).

During peak inhalation (Phase B) at the coronal plane, axial flow was stronger in the

anatomical right side of the airway compared to the left side of the airway. At Plane 3, with an increase in inhalation time, axial velocity magnitude increased until peak inhalation (Phase B) and later decreased at Phase C. Strong axial flow was observed at Plane 3 during Phase B as compared to Phase A, near the inner walls of the bifurcation (anatomical left side). At Plane 4, uniformly distributed flow with small flow separation near the outer airway walls at Phase A, a uniform axial flow at Phase B and axial flow similar to Phase A was observed in Phase C. At Planes 3 and 4, nearly similar secondary flow patterns can be seen throughout inhalation.

Figure S2 (Supplementary Materials) shows the detailed view of the flow field for Wo = 2.41 at IT/BT = 33% during inhalation at Planes 1–2 (trachea, G0) and Planes 3–4 (G1). The magnitude of axial velocity at each plane increased until peak inhalation (Phase B) and later decreased at Phase C. At peak inhalation, secondary flow with a rotational flow pattern was observed near the wall at Plane 1 (phases A, B, and C), Plane 2 (Phase A), and Plane 3 (phases A, B, and C). Secondary flow was not observed during peak inhalation at Plane 4. coronal planes showed unequal flow distribution at first bifurcation during peak inhalation (Phase B), similar to those observed for Wo = 2.41 at IT/BT = 25% and 50%.

Axial flow patterns were altered with increasing Wo to 24.1 for IT/BT = 50% (Figure 4.6), as compared to those previously observed for Wo = 2.41 for the same IT/BT. coronal planes showed increased axial flow from Phase A to Phase C during inhalation. Higher generations (G3) at peak inhalation had a stronger axial flow strength compared to G1 for Wo = 24.1 and IT/BT = 50%. During inhalation, uniform axial flow can be observed at Planes 2–4 with increased secondary flow strength from G1 to G2. Across phases A to C, very weak secondary flow with uniformly distributed axial flow was observed during inhalation.

Figure S3 (Supplementary Materials) shows the detailed view of the flow field during inhalation at Planes 1–2 (trachea, G0) and Planes 3–4 (G1) for Wo = 24.1 and IT/BT = 33%. At Plane 1, axial velocity magnitude increased until peak inhalation (Phase B) and

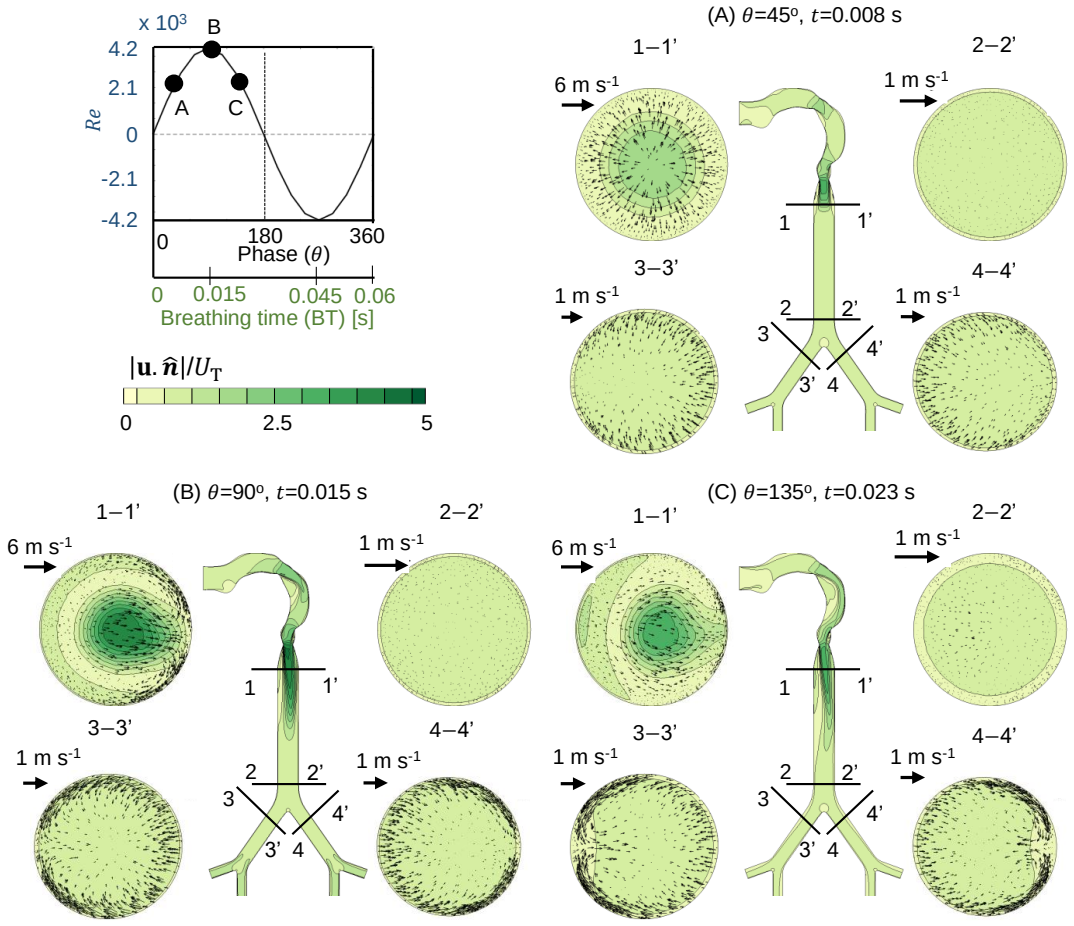

Figure 3.8: Contours of magnitude of plane-normal velocity component (nondimensionalized with mean flow speed in trachea, U_T) with superimposed in-plane velocity vectors for Planes 1–4 at various time-points during inhalation for Wo = 24.1 at IT/BT = 50%. A is at Phase θ = 45° (= 25% IT), B is at Phase θ = 90° (= 50% IT), and C is at Phase θ = 135° (= 75% IT).

later decreased at Phase C. Axial velocity was strongest at the center of Plane 1. Secondary flow patterns at Planes 2 to 4 for IT/BT = 33% were similar to those for IT/BT = 50% (at the same planes and Wo). When comparing IT/BT = 33% to IT/BT = 50%, only minor differences were observed between the cross-sectional distribution of axial flow at Planes 2 to 4. Additionally, a slight decrease in the jet can be noticed from the flow contours of the coronal plane.

With increasing IT/BT from 25% (Figure 4.2) to 50% (Figure 4.5) at the lower Wo of 2.41, axial flow of similar magnitude was observed at Plane 1 at all phases, respectively.

However, peak axial flow was concentrated towards the ventral side during early and late inhalation for 25% IT/BT compared to the dorsal side at the same phases in 33% (Figure S2 in the Supplementary Materials) and 50% IT/BT conditions. In addition, at lower *Wo*, all planes showed nearly similar velocity magnitudes, respectively at each phase, with a change in the IT/BT ratio. Secondary flow at lower *Wo* from IT/BT = 25% to 50% showed increased velocity vectors during early inhalation and decreased secondary flow velocity vectors during peak until late inhalation. An increase in IT/BT slightly affected the axial flow in the upper trachea in the early inhalation (Phase A). Over all, the effect of IT/BT at lower *Wo* showed a minimal effect on axial flow and secondary flow during the early inhalation phase.

With an increase in IT/BT at the higher *Wo* of 24.1, axial flow magnitude in the trachea increased both axial flow (compare Figure 4.3, Figure S3 in the Supplementary Materials, Figure 4.6) and secondary at early inhalation. In addition, axial flow remained the same during peak and late inhalation with an increase in the IT/BT ratio, while the secondary flow decreased respectively at each plane. Contours from the coronal plane showed increased axial jet flow in the upper trachea with increasing IT/BT for both *Wo*, respectively.

Figure S4 shows nondimensional axial velocity magnitude contours overlaid with secondary flow fields during exhalation at *Wo* = 2.41 for IT/BT = 50%. Strong axial flow can be observed at Phase D until peak exhalation (Phase E) and later decreased at late exhalation (Phase F). Plane 1 showed nonuniform secondary flow throughout the exhalation. In addition, secondary flow increased in strength at peak exhalation (Phase E) compared to Phase D, and later decreased during 75% exhalation (Phase F). Multiple rotational flow patterns were observed near the wall of Plane 2 during all three phases of exhalation (D, E, F). Secondary flow patterns during the exhalation remained nearly same in Planes 3 and 4, respectively, with higher strength in Plane 4 compared to Plane 3.

Drastic differences in exhalation flow can be observed for *Wo* = 23.7 with an increase in IT/BT = 25% to 50%. Axial flow increased with an increase in IT/BT ratio, as observed

from all planes of Figures 4.4 and S4 at each phase. Further, axial velocity increased in magnitude with increasing time from Phase D to Phase E and later decreased until Phase F in the mouth-to-glottis section. Secondary flow decreased at the early exhalation phase in the upper trachea with an increase in the IT/BT ratio. Additionally, the secondary flow strength increased in the lower trachea during Phase E (peak exhalation) and Phase F (late exhalation) with an increase in the IT/BT ratio.

To conclude, during exhalation at Planes 1 to 4 for both *Wo*, axial flow increased with increasing IT/BT from 25% (Figures 3.5 and 4.4) to 50% (Figures S4 and S5 in the Supplementary Materials). This increase in axial flow was mainly due to increasing *Re* with increasing IT/BT during exhalation. Further, increase in IT/BT increased the secondary flow strength in the lower portion of the trachea for each *Wo*, respectively.

3.4.5 Velocity Profiles

3D velocity (**u**) was extracted along the coronal plane during peak inhalation at planes 1-10 for *Wo*=2.41 and 24.1 at IT/BT=25% and 50% and are presented in **Figures 3.9, 3.10** and **Figure S6** (Supplementary Material). Velocity profiles for *Wo*=2.41 at IT/BT=25% and 50% showed narrow distribution, while a *Wo* wider distribution of velocity was observed in the upper trachea (line 1) for *Wo*=24.1 at IT/BT=25% and 50%. However, the flow in the trachea decreased at plane 2 (line 2) compared to the upper trachea (line 1) for all conditions. Comparing across *Wo*, velocity magnitude at plane 2 for *Wo*=2.41 was greater than that of *Wo*=24.1 for each IT/BT ratio. Velocity profiles showed variation in axial flow between planes 3 and 4 at *Wo*=2.41 for both IT/BT. In comparison, axial flow from velocity profiles for *Wo*=24.1 at planes 3 and 4 was uniform and of the same magnitude (**Figure 3.10**).

The right bifurcation (lines 5, 7 and 9 in Planes 5, 7 and 9, respectively) showed higher axial flow compared to the left bifurcation (lines 6, 8 and 10 in Planes 6, 8 and 10, respectively) at *Wo* = 2.41 for IT/BT = 25% and 50% (refer to Figure S6 (Supplementary

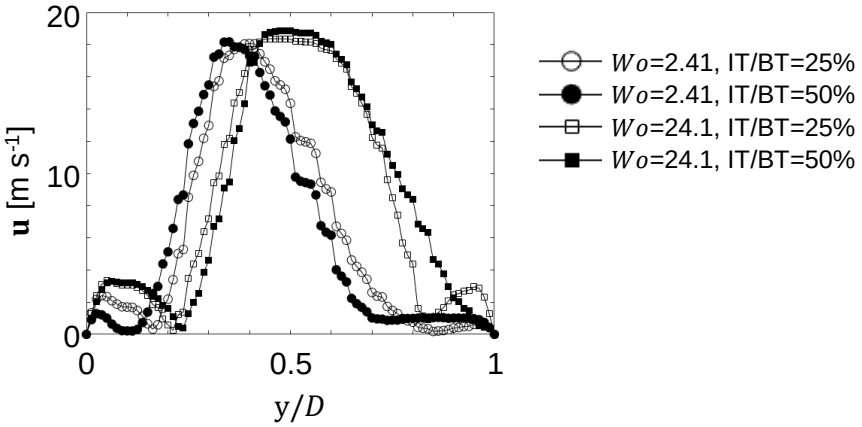

Figure 3.9: Three-dimensional velocity (**u**) extracted at the upper trachea (line 1-1' at the coronal plane) as a function ofnondimensional diameter y/D, where D = trachea diameter = 18 mm.

Materials)), while for Wo = 24.1, nearly uniform axial flow was observed between left and right bifurcation for both IT/BT conditions.

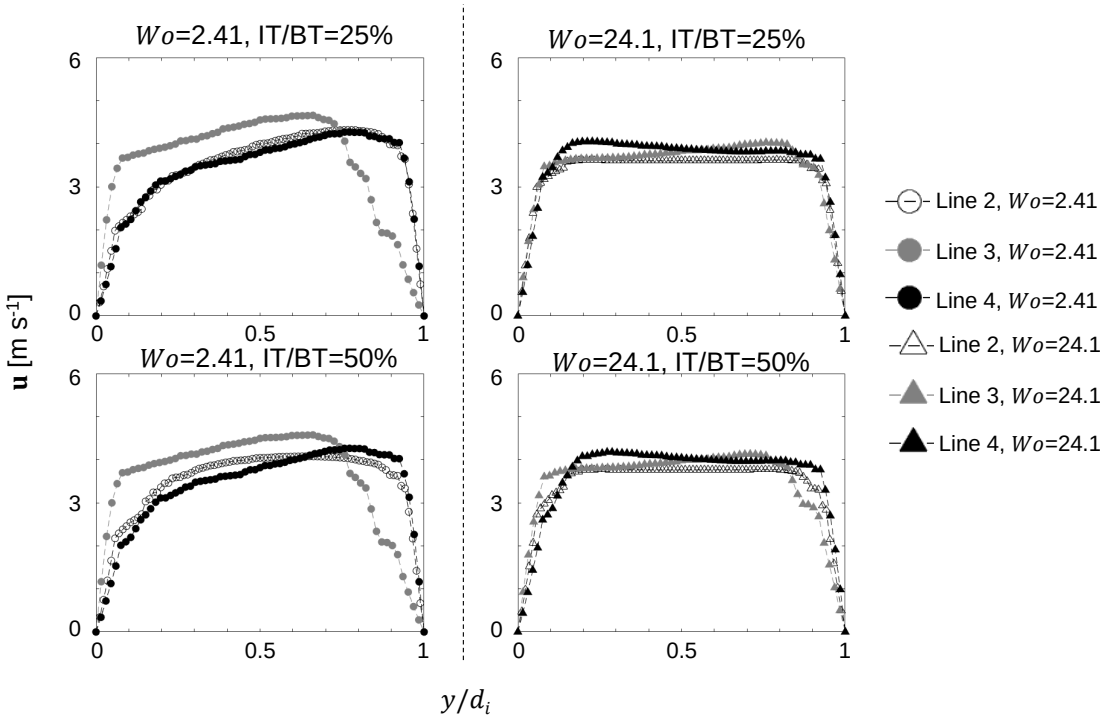

Figure 3.10: Velocity profiles at Planes 2–4 for varying Wo and IT/BT conditions. Three-dimensional velocity (**u**) extracted at lines 2–4 (refer Figure 3.1) is shown as a function ofnondimensional diameter y/d_i, where d_i is the airway cross-sectional diameter in Plane i (refer to Table 3.2).

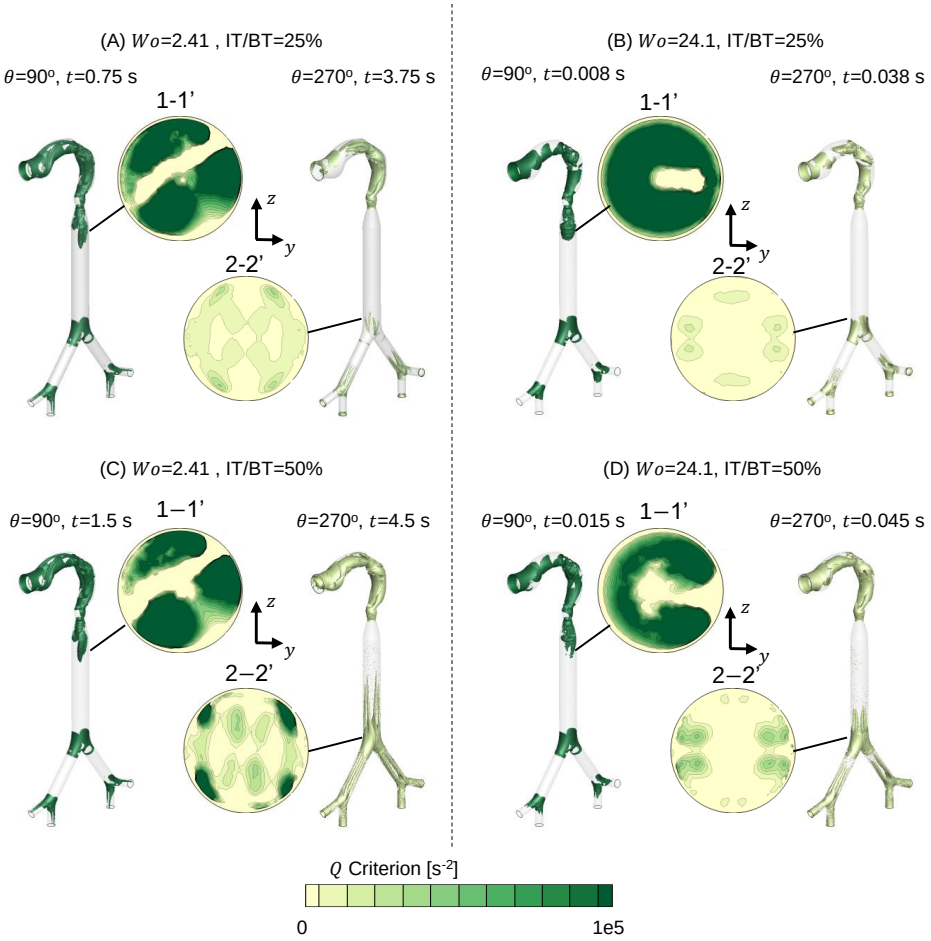

Figure 3.11: Q-criterion isosurface at peak inhalation (Q = 100,000 s^{-2}) and peak exhalation (Q = 15,000 s^{-2}) for all breathing conditions (A) Wo = 2.41, IT/BT = 25% (B) Wo = 24.1, IT/BT = 25% (C) Wo = 2.41, IT/BT = 50%, and (D) Wo = 24.1, IT/BT = 50% are shown along with Plane 1 (peak inhalation) and Plane 2 (peak exhalation).

3.4.6 Secondary Flow Vortices

Secondary flow vortices were identified using the Q criterion, and are shown in Figure 3.11 for Wo = 2.41 and Wo = 24.1 at IT/BT = 25% and 50%, during peak inhalation (θ = 90°) and peak exhalation (θ = 270°). Isosurfaces at Q = 100,000 s^{-2} (peak inhalation) and Q = 15,000 s^{-2} (peak exhalation) were used for visualization of secondary flows at Plane 1-1' (at peak inhalation) and Plane 2-2' (at peak exhalation). For Wo = 2.41 at peak inhalation (θ = 90°), the secondary flow distribution in the trachea remained unaltered with an increase in IT/BT, while a small change in secondary flow pattern can be seen for Wo = 24.1 with an increase in the IT/BT ratio. For Wo = 2.41, isosurface contours at Plane 1 showed two

regions with secondary flow vortices near the anatomical left-ventral side and a smaller region along the anatomical right-dorsal side. For Wo = 24.1, secondary flow was observed along the walls at peak inhalation from Plane 1 for all IT/BT conditions.

At peak exhalation for Wo = 2.41 at IT/BT = 25%, small secondary flow vortices were observed near the bifurcation of the parent generation, while for Wo = 24.1 and IT/BT = 25%, secondary flow vortices were observed in G1 only. Increasing IT/BT for both Wo increased the length of the secondary flow regions (axial dimension) vortex structures. Comparing across all conditions, Wo = 2.41 at IT/BT = 50% showed a larger distribution of secondary flow regions (refer to Movie SA1.1–3).

3.4.7 Integral Parameters

To quantify axial flow streaming and strength of secondary flow, integral parameters (Banko et al., 2016) were calculated using Equations (3.8) and (3.9) for all Wo and IT/BT conditions at the planes in Table 3.2. Integral parameter I_1 at Planes 2–4 are shown in Figures 3.12 and 3.13. Axial flow streaming (I_1) during inhalation was stronger than I_1 during exhalation (Figure 3.12) for IT/BT = 25%, while I_1 variation at Planes 2–4 was similar when comparing inhalation to exhalation for IT/BT = 50%. For Wo = 2.41 and 7.61, axial flow streaming was asymmetric after the first bifurcation, and for Wo = 24.1, axial flow streaming remained almost the same in both planes. At first bifurcation, within the G1, I_1 at the right bifurcation (Plane 3) was higher compared to the left bifurcation (Plane 4) in Wo = 2.41 (both IT/BT) and 7.61 (IT/BT = 50%), while I_1 was higher in the left bifurcation for Wo = 7.61 (IT/BT = 25%) and remained almost the same in Wo = 24.1 in both IT/BT conditions. During inhalation or exhalation for a given Wo, I_1 increased from start to mid-phase (inhalation or exhalation) and later decreased until the end of the phase (inhalation or exhalation). With increase in IT/BT to 50%, a similar trend was observed for I_1. At a fixed cross-sectional location (Planes 2–4), changing either Wo or IT/BT did not impact much of axial flow streaming (I_1) during inhalation. For each Wo comparing across the

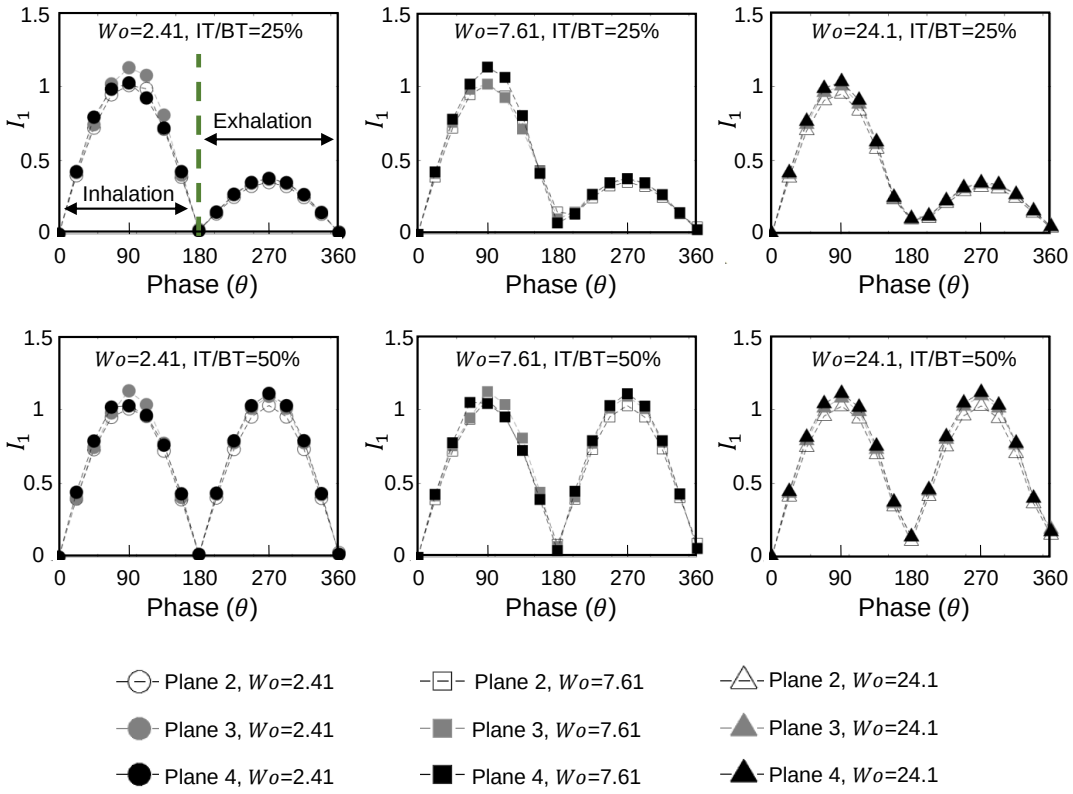

Figure 3.12: Integral parameter I_1 calculated using Equations (3.8) at Planes 2–4 for all breathing conditions at IT/BT = 25% (top row) and IT/BT = 50% (bottom row). Wo = 2.41 (- -●- -); Wo = 7.61 (- -■- -); Wo = 24.1 (- -▲- -). Open, gray-filled, and black-filled markers correspond to Planes 2, 3 and 4, respectively.

IT/BT, the I_1 during exhalation was higher at IT/BT = 50% following the trend of an inlet velocity profile.

Figure 3.13 shows integral parameter I_1 at Planes 5–10. Across all conditions, strong axial flow streaming was observed throughout the breathing cycle. The phase-variation of I_1 during either inhalation or exhalation was identical to the corresponding phase-variation observed in Planes 2–4, that is, an increase from the start of inhalation (start of exhalation) to the peak value at mid-inhalation (or mid-exhalation) and decreasing until the end of inhalation (end of exhalation). For Wo = 2.41 (both IT/BT) and Wo = 7.61 (IT/BT = 50%), the right bifurcation (Planes 5, 7, 9) showed increased axial flow streaming compared to the left bifurcation (Planes 6, 8, 10), while for Wo = 7.61, the right bifurcation (Planes 5, 7, 9) showed decreased axial flow streaming compared to the left bifurcation (Planes 6, 8, 10) at

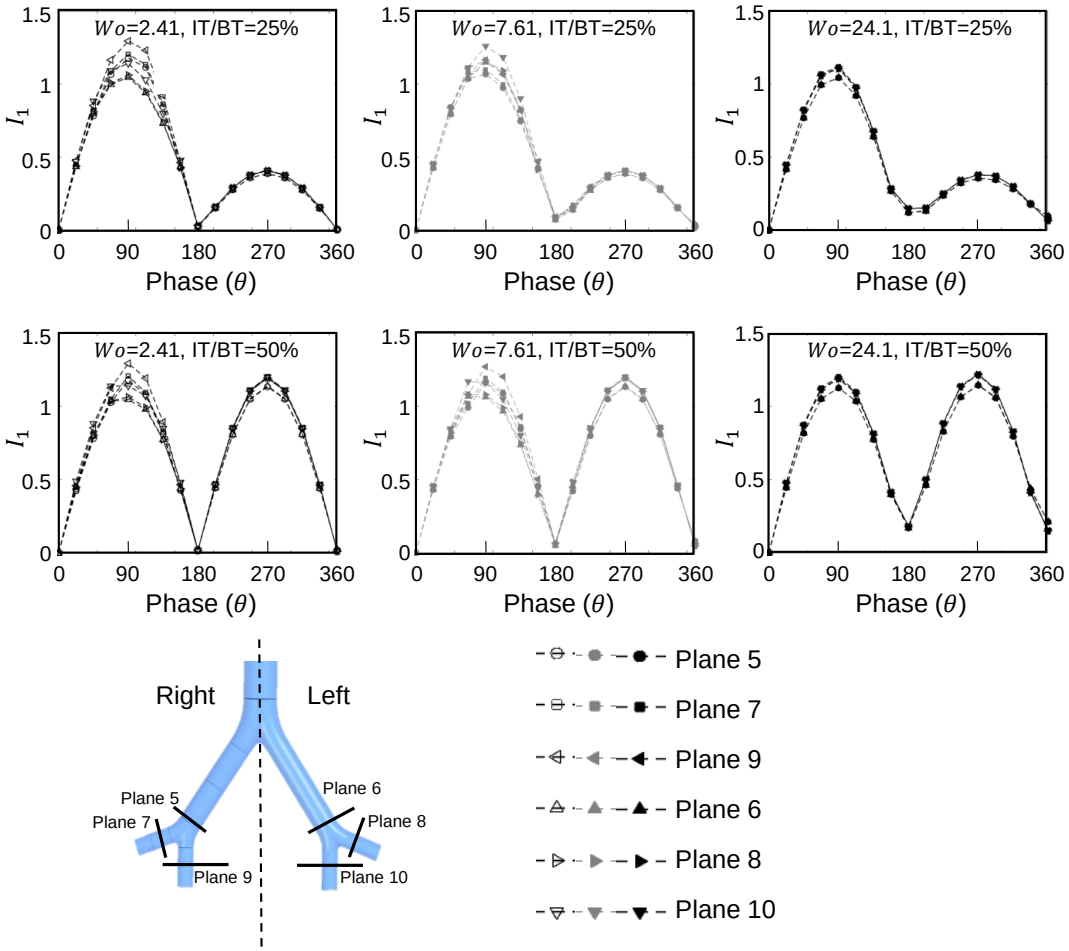

Figure 3.13: Integral parameter I_1 calculated at Planes 5–10 for all breathing conditions at IT/BT = 25% (top row) and IT/BT = 50% (bottom row). Planes 5 (- -●- -), 7 (- -■- -), and 9 (- -◀- -) are from the right bifurcation. Planes 6 (- -▲- -), 8 (- -▶- -) and 10 (- -▼- -) are from the left bifurcation. Open, gray-filled, and black-filled markers represent *Wo* conditions of 2.41, 7.61, and 24.1, respectively.

IT/BT= 25%, and *Wo* = 24.1 (both IT/BT) showed equal axial flow streaming between the left (Planes 6, 8, 10) and right (Planes 5, 7, 9) bifurcation planes, respectively. For all the conditions, within the G2, I_1 at the right bifurcation showed to be higher or equal in Plane 9 compared to Plane 7, and at the left bifurcation, Plane 10 had higher or equal I_1 compared to Plane 8. The left–right asymmetry of I_1 that was noted at Planes 3 and 4 (Figure 3.12) was also sustained in the higher-generation G2 (Planes 7–10). Additionally, the I_1 during exhalation was higher at IT/BT = 50% in all conditions following the velocity profile.

Figure 3.14 shows phase-variation of the integral parameter I_2 at Planes 2–4, which is indicative of the lateral dispersion or the strength of the secondary flow. Across all conditions (*Wo*, IT/BT), I_2 variation throughout the cycle at Planes 2–4 followed the same order as that of I_1 (Figure 3.12). I_2 values were greater than I_1 values at any of these Planes, irrespective of *Wo* and IT/BT, where I_1 and I_2 were compared. While axial flow streaming was present at Planes 2–4 for all *Wo* and IT/BT examined here (Figure 3.12), secondary flows appear to be stronger. For a given IT/BT, increasing *Wo* resulted in increasing I_2 at the end of inhalation ($\theta = 180^{\circ}$). Specific to *Wo* = 23.7, the secondary flow was also observed at the end of exhalation ($\theta = 360^{\circ}$) for IT/BT = 50%. At a fixed cross-sectional location (Planes 2–4), individually changing either *Wo* or IT/BT did not impact secondary flow streaming (I_2) during inhalation. For each *Wo*, comparing across the IT/BT, the I_2 during exhalation was higher at IT/BT = 50% following the velocity profile.

Figure 3.15 shows phase-variation of integral parameter I_2 at Planes 5–10. In general, I_2 variation along Planes 5–10 mirrored those of I_1 (Figure 3.13). Similar to I_1, even I_2 increased from the start of inhalation (start of exhalation) to reach peak value at mid-inhalation (mid-exhalation) and decreased until the end of inhalation (end of exhalation). Additionally, similar to I_1 (Figure 3.13), for *Wo* = 2.41 (both IT/BT) and *Wo* = 7.61 (IT/BT = 50%), the right bifurcation (Planes 5, 7, 9) showed increased secondary flow streaming compared to the left bifurcation (Planes 6, 8, 10), while for *Wo* = 7.61, the right bifurcation (Planes 5, 7, 9) showed decreased secondary flow streaming compared to the left bifurcation (Planes 6, 8, 10) at IT/BT = 25%, and *Wo* = 24.1 (both IT/BT) showed equal secondary flow streaming between the left (Planes 6, 8, 10) and right (Planes 5, 7, 9) bifurcation planes, respectively. For all the conditions, within the G2, I_2 at the right bifurcation showed higher or equal in Plane 9 compared to Plane 7, and at the left bifurcation, Plane 10 had higher or equal I_2 compared to Plane 8. A similar pattern was also observed for I_2 variation across the planes for all *Wo* and IT/BT conditions. Overall, I_2 was greater than I_1 across Planes 2–10 for all IT/BT and *Wo*, suggesting that secondary flows are stronger

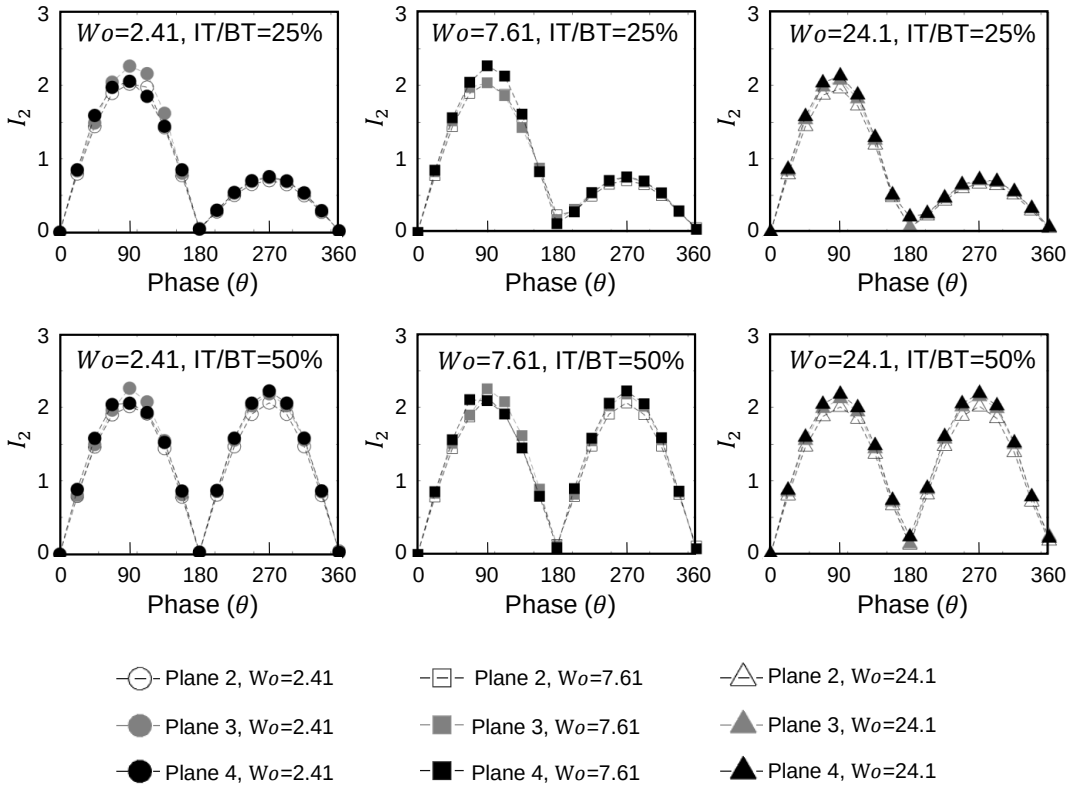

Figure 3.14: Integral parameter I_2 calculated at Planes 2–4 for all breathing conditions at IT/BT = 25% (top row) and IT/BT = 50% (bottom row). Refer to Figure 3.12 for marker definitions.

transport mechanisms than axial streaming.

For a given condition at each phase, integral parameters over the complete breathing cycle showed an increase (both I_1 and I_2) with an increase in airway generation number. This increase was mainly due to incompressible flow simulations, such that flow velocity increased in higher generations with smaller diameters than the parent airway diameter. As a result, the value of integral parameters increased from G0 to G2, which was not observed in previous subject-specific model studies (Banko et al., 2015; Jalal et al., 2020; Banko et al., 2016). For a symmetric airway model with parent airway diameter (D) = 18 mm, the expected daughter airway diameter using Murray's law (daughter airway diameter, (d_o) = $D/2^{1/3}$) is 14.2 mm, which was approximately the same parent airway to the daughter airway diameter relation in Banko et al. (2016, 2015). However, the idealized Weibel airway model used here has a daughter airway diameter less than those estimated using

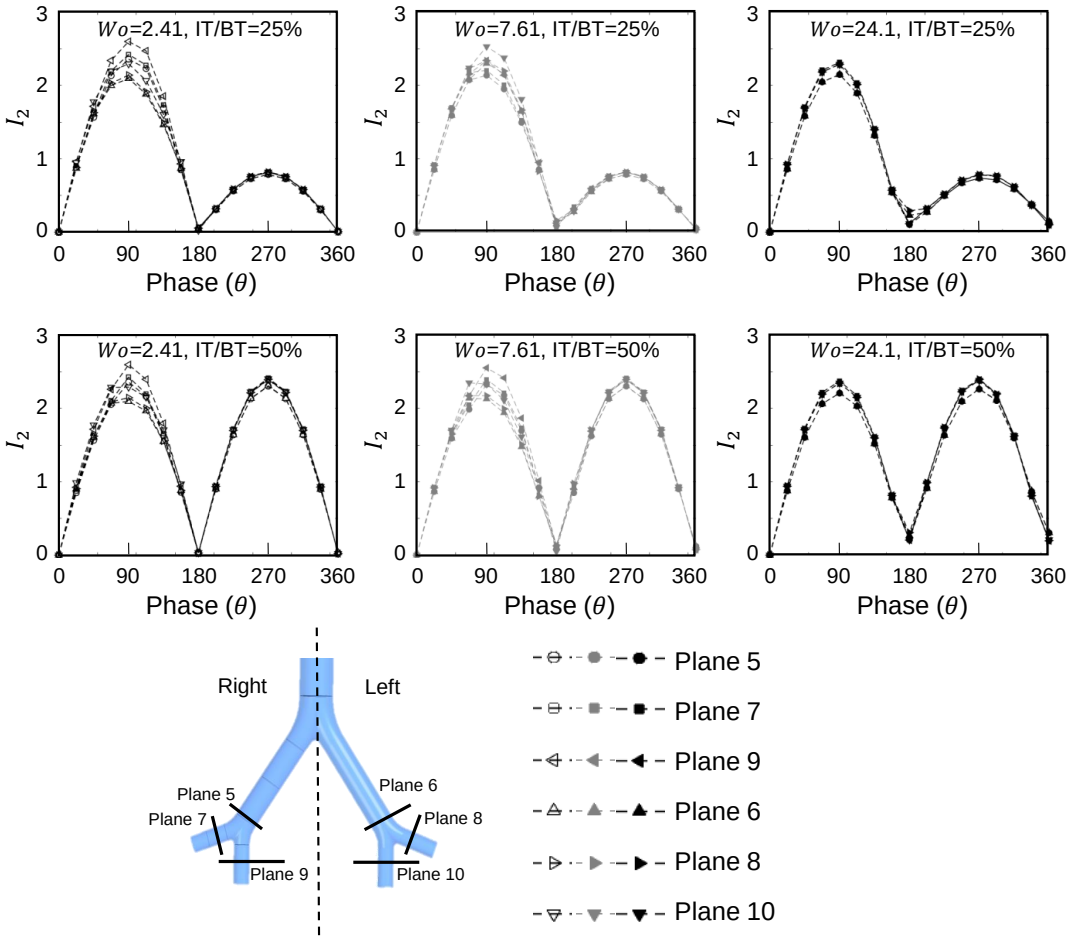

Figure 3.15: Integral parameter I_2 calculated at Planes 5–10 for all breathing conditions at IT/BT = 25% (top row) and IT/BT = 50% (bottom row). Refer to Figure 3.13 for marker definitions.

Murray's law-based minimum daughter airway diameter (12.2 mm). Therefore, the flow velocity increased in daughter airways that in turn increased the integral parameters of higher generations. Despite the parent-to-daughter airway diameter ratios in the Weibel model deviating from ratios predicted using Murray's law, we observed identical trends of increasing axial flow streaming and decreasing lateral dispersion for all generations as those reported by Banko et al. (2016).

At a given cross-section, I_1 and I_2 for Wo = 7.61 and IT/BT = 50% showed nearly no variation at peak inhalation and peak exhalation across all generations, which was in disagreement with the Wo = 7 findings of (Banko et al., 2016) (I_1 was more significant

at peak inhalation and I_2 was larger at peak exhalation). Our idealized symmetric airway geometry is likely the reason for this disagreement compared to the asymmetric subject-specific airway of Banko et al. (2016). Current results for I_1 and I_2 trends agreed with those reported by Banko et al. (2016) for higher generations, such as I_1 and I_2 increasing and decreasing in a manner identical to the prescribed inflow velocity profile throughout a breathing cycle. Interestingly, I_1 and I_2 values showed noticeable variation between the planes at all generations (e.g., $I_{1,\mathrm{G0}} < I_{1,\mathrm{G1}} < I_{1,\mathrm{G2}}$), suggesting that decreased airway diameters from the previous generation possibly increased the velocity of the flow, as well as the flow strengths. I_1 and I_2 showed variations between the left- and right-side airways of the same generation for curved mouth-to-glottis orientations, such that local flow features can be responsible for lagging/leading axial flow streaming and lateral dispersion relative to the inflow profile, depending on the bronchial path and the generation number. This observation was also previously noted by Banko et al. (2016).

3.5 Discussion

Particle deposition and gas exchange within the human respiratory system are intricately dependent on flow through the airway. While previous studies have identified that axial flow streaming and lateral dispersion are effective transport mechanisms in the human airway (Banko et al., 2015, 2016; Jalal et al., 2016, 2018, 2020), the effects of varying inhalation duration (IT/BT) in conjunction with the respiratory rate (RR) on airway flow characteristics remain unknown. The majority of airway fluid dynamics studies have either focused only on inhalation, or examined both inhalation and exhalation with IT/BT = 50%. Inter-subject variability of IT/BT $<$ 50% can occur in voluntary and involuntary breathing exercises. Further, clinical therapies, such as HFOV, allow for patient-specific tuning of IT/BT and RR. Studies of varying IT/BT alongside RR can help identify fundamental differences in axial and lateral flow patterns, potentially valuable for improving airway flow distribution in HFOV therapy. We examined the role of varying IT/BT from 25% to

50% and RR from 10 bpm to 1000 bpm using 3D CFD simulations of airflow through an idealized double bifurcation airway model.

Axial and secondary flows were observed across all *Wo* and IT/BT conditions examined in this study (refer Movie SA1.1–3). Several differences can be observed when comparing flow fields at *Wo* = 24.1 to those at lower *Wo*. At the upper tracheal section (Plane 1) for IT/BT = 25%, asymmetric axial velocity distribution was observed for *Wo* = 2.41, as opposed to a centrally concentrated distribution of axial velocity for *Wo* = 24.1 during inhalation. The lower tracheal section (Plane 2) for IT/BT = 25% uniform axial velocity distribution for all *Wo*. Asymmetric distribution of axial velocity was observed following the first and second bifurcations at lower *Wo*.

Across all *Wo* and IT/BT conditions, *Wo* = 2.41 and 7.61 showed the strongest axial flow streaming (I_1) and lateral flow dispersion at Plane 9 and Plane 10 during inhalation, while during exhalation, all *Wo* and IT/BT = 50% showed both strongest axial flow streaming (I_1) and secondary flow strength (I_2) at Planes 7–10 (G2). The latter observation regarding I_2 was in partial agreement with findings of a previous MRV study of flow through an idealized double bifurcation model (Jalal et al., 2018), where secondary flows during inhalation and exhalation were reported to be strengthened with increasing *Wo*. Our results showed increased secondary flow strength at the end of inhalation, with an increase in *Wo* along with equal secondary flow strengths for planes in a given generation ($I_{2,\text{Plane 5}} = I_{2,\text{Plane 6}}$, $I_{2\text{Plane 7}} = I_{2,\text{Plane 8}} = I_{2,\text{Plane 9}} = I_{2,\text{Plane 10}}$). In terms of secondary flow fields, we observed the generation of vortices at all *Wo* during inhalation and exhalation. These secondary flow vortices can be expected to impact particle deposition in applications such as targeted drug delivery.

Similar to the observations of Banko et al. (2015, 2016) where *Wo* = 7 and IT/BT = 50%, a single-sided axial vortex (see Plane 1 at Phase B in Figures 4.2 and 4.5) was observed during peak inhalation in the trachea for *Wo* = 2.41 across all IT/BT ratios. Banko et al. (2016) noted that the vortex at peak inhalation was not previously observed in studies

using idealized symmetric geometries. Compared to idealized airway models, our airway geometry includes the mouth-to-glottis section in the coronal plane instead of the sagittal plane. Despite the left–right symmetry in our model starting from the glottis, the presence of a mouth-to-glottis section on the anatomical right side promoted single-sided axial swirls at lower *Wo* (vortex structure from Figure 3.11). The effect of the glottis can also be seen during inhalation, through axial flow velocity contours in all *Wo* and IT/BT in the upper trachea.

Choi et al. (2009) used large eddy simulations to examine the effect of upper airway truncation on the flow in the trachea, and found that the airways above the glottis were crucial for generating turbulence in the trachea. Our results showing the formation of vortex structures point to the importance of including the upper airway structure and its orientation relative to the sagittal plane, which was also noted previously by Lin et al. (2007). Obstructions such as tongue and upper mouth geometry that were not included in our model can also enhance turbulence in the airway flow, and has been noted by Lin et al. (2007). Further studies on subject-specific airways are needed to isolate how each of these anatomical structures impact fluid dynamics and examine the importance of *Wo* and IT/BT in generating asymmetric axial flow in the airway.

Finally, for a given peak inhalation Re_{T}, a change in IT/BT ratio for a given *Wo* affected the tidal volume. With an increase in IT/BT ratio, tidal inhalation volume increased. The exhalation tidal volume was matched with tidal inhalation volume to maintain equal volumes in both inhalation and exhalation for involuntary breathing frequencies, such that lower IT/BT ratio breathing has smaller *Re*-based exhalation velocity profiles. The lower exhalation velocity profile affected the axial flow streaming in all generations, showing lower strength of primary and secondary flows. Using varying IT/BT ratio might be beneficial with peak inhalation and exhalation of equal *Re*, such that exhalation tidal volume would be more than an inhalation tidal volume, resulting in a greater amount of gases that would have been expelled out, which is indeed necessary for some situations, such as in

ARDS (Lunkenheimer et al., 1972).

Modified Flow Regime Diagram

Jan et al. (1989) developed a diagram to classify the flow regime within different sections of the human airway, using an order of magnitude analysis starting from the Navier–Stokes' equations. This diagram was used to characterize the influence of fluid viscosity, unsteadiness, and convective acceleration in an idealized airway bifurcation for Wo ranging from 2.3 to 21.3. Their flow map examined Wo^2 versusnondimensional stroke length $2L/D$, where L is the stroke length (i.e., axial length of travel of a fluid particle) that can be calculated as the ratio of stroke volume (SV) swept in a cycle to the tracheal cross-sectional area) and D is the tracheal diameter. For a sinusoidal waveform (as considered in this study), Jan et al. (1989) showed that Re is related to dimensionless stroke length ($2L/D$) and Wo as $Re/Wo^2 = 2L/D$. However, their classification was restricted to oscillatory (sinusoidal) breathing cycle with IT/BT = 50%. Table 3.3 shows the SV, L, $2L/D$ evaluated for this study at the upper tracheal cross-section (Plane 1) across the various conditions of Wo and IT/BT, where Re = 4200, based on U_{T} and D. It can be seen that Re/Wo^2 does not equal $2L/D$ when IT/BT $\neq$ 50%.

To include the effect of IT/BT $\neq$ 50%, we examined the use of a modified dimensionless stroke length, where the parameter (BT/2 IT) is included as a multiple of $2L/D$ (i.e., $(2L/D)$(BT/2 IT)). The modified dimensionless stroke length matched Re/Wo^2 for all Wo and IT/BT conditions considered in this study (Table 3.3), showing the importance of including IT/BT to classify the operating flow regime accurately. To examine the operating flow regimes at the cross-sectional locations where we analyzed the 3D CFD data (Planes 1–10), we calculated local values of the Reynolds number (Re_{L}) and Womersley number (Wo_{L}) as follows:

$$Re_{\mathrm{L}} = \frac{V_{\mathrm{L}} D_{\mathrm{L}}}{\nu} \tag{3.10}$$

Table 3.3: Flow regime parameters evaluated at the upper tracheal section (plane 1): Re/Wo^2, dimensionless stroke length $2L/D$ and modified dimensionless stroke length $(2L/D)$(BT/2 IT). Stroke length (L) was calculated as: $\frac{\text{SV}}{\pi D^2/4}$, where SV=stroke volume and D=tracheal diameter=0.018 m . SV was obtained by integrating the time-varying volumetric flow rate at the inlet (Q_{in}) over a breathing cycle for each Wo and IT/BT condition, where $Q_{\text{in}}(t) = V_{\text{inlet}}(t)\, A_{\text{in}}$ (prescribed inlet velocity profile, $V_{\text{inlet}}(t)$, refer 3.5-3.6). Reynolds number (Re) based on D and mean flow speed in trachea (U_{T}) was calculated using equation defined as: Re=$\frac{U_{\text{T}}D}{\nu}$, where U_{T} (=3.4 m s^{-1}). Re was maintained constant at 4,200 across all test conditions. Womersley number (Wo) was calculated using equation (3.1). Note that breathing time (in seconds), BT=(60/RR), where RR=respiratory rate (in bpm).

RR [bpm]	Wo	IT/BT [%]	SV [m^3]	L [m]	$2L/D$	Re/Wo^2	$(2L/D)$(BT/2 IT)
10	2.41	50	1.66×10^{-3}	6.51	724	723	724
10	2.41	33	1.09×10^{-3}	4.3	478	723	724
10	2.41	25	0.83×10^{-3}	3.26	362	723	724
100	7.61	50	1.66×10^{-4}	0.65	72	72	72
100	7.61	33	1.09×10^{-4}	0.43	48	72	72
100	7.61	25	0.83×10^{-4}	0.33	36	72	72
1000	24.1	50	1.66×10^{-5}	0.07	7	7	7
1000	24.1	33	1.09×10^{-5}	0.04	5	7	7
1000	24.1	25	0.83×10^{-5}	0.03	4	7	7

$$Wo_{\text{L}} = \frac{D_{\text{L}}}{2}\sqrt{\left(\frac{2\pi}{\text{BT}}\right)\left(\frac{1}{\nu}\right)}, \tag{3.11}$$

where V_{L} and D_{L} denote the axial velocity and in-plane airway diameter, respectively, at a given cross-sectional plane (Table S1 in the Supplementary Materials). Re_{L} and Wo_{L} are interrelated via the modified dimensionless stroke length as: $Re_{\text{L}}/Wo_{\text{L}}^2 = (2L_{\text{L}}/D_{\text{L}})(BT/2\,IT)$.

The values of Re_{L} and Wo_{L} for a given test condition (i.e., Wo, IT/BT) were averaged over the different planes included within a particular generation (see Table 3.2 for plane locations). The regime diagram for classifying the flow regime at different generations is shown in Figure 3.16, where Wo_{L}^2 is plotted along the x-axis and the modified dimensionless stroke length ($(2L_{\text{L}}/D_{\text{L}})$(BT/2 IT)) is plotted along the y-axis. For a given Wo and generation number, varying IT/BT did not noticeably alter flow regime location when using the modified dimensionless stroke length. For Wo = 2.41, the trachea (G0) was in the turbulent zone of the regime diagram.

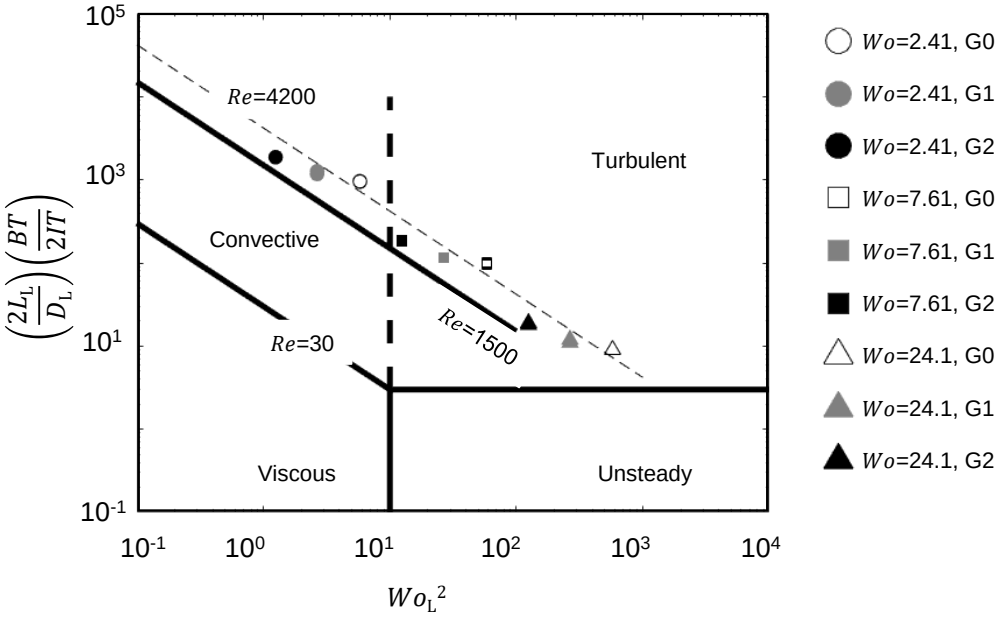

Figure 3.16: Modified regime diagram (originally proposed by (Jan et al., 1989)) for classifying the flow at the planes identified in Table 3.2, interrelating the local Womersley number and modified stroke length ($(2L_L/D_L)$(BT/2 IT)). Multiple markers of the same type indicate variations in IT/BT.

With increasing *Wo* beyond 2.41, flow through the trachea was in the unsteady convective zone, meaning that both unsteady and convective acceleration terms are important in the Navier–Stokes' equations. With increased generation number (i.e., moving further down the airway) for either *Wo* = 2.41 or *Wo* = 7.61, the flow regime tends towards the viscous-convective zone so that unsteady effects are not dominant (quasisteady). At *Wo* = 24.1, all three generations are in the weak turbulence ($Re/Wo \approx$ 100–200 (Jan et al., 1989)), such that unsteady effects on the flow field are the most dominant. Our flow regime results agree with MRV studies on a subject-specific anatomical model at *Wo* = 7 (Banko et al., 2016) and on a planar double bifurcation model at *Wo* = 6 and *Wo* = 12 (Jalal et al., 2018). At *Wo* relevant to HFOV, gas exchange and particle deposition at higher airway generations are expected to be most impacted by the unsteady acceleration of the flow. By contrast, viscous forces and convective acceleration are expected to be more influential at lower *Wo*.

Investigating the 3D fluid dynamics in anatomically accurate airway models and physiologically relevant breathing patterns can be computationally demanding. Inter-subject variability in geometry can present challenges (Borojeni et al., 2020) in identifying salient features of the fluid flow and in developing modified scaling relations as in this study. In this regard, studies of idealized airway models with sinusoidal breathing patterns can help in providing a basic understanding of flow physics at relatively low computational cost. The current study investigated the flow features inside the airways for an idealized airway geometry, varying clinically significant parameters (IT/BT and RR). The modified dimensionless stroke length identified in this work can be useful for fluid dynamic studies of clinically relevant situations where IT/BT variation (e.g., mechanical ventilation in COPD and asthma patients (Loring et al., 1990; Shanholtz and Brower, 1994; Ahmed and Athar, 2015; Boros et al., 1977) and RR variation (e.g., HFOV in neonates) are observed. Future studies using subject-specific geometries are needed to examine the clinical significance of our findings.

3.6 Conclusions

Using 3D CFD simulations, we examined the roles of varying respiratory rate and inhalation duration (IT/BT) on flow through an idealized human airway model consisting of a mouth-to-glottis section and two generations. Axial and secondary flows were observed throughout the model at all conditions of Wo and IT/BT. For Wo = 2.41, the strong non-axisymmetric axial flow was observed in the trachea during inhalation. For Wo = 24.1, centrally concentrated axial flow was observed during inhalation in the upper trachea, followed by uniformly distributed weak axial flow in the lower trachea. On account of secondary flow, lateral dispersion was found to be the dominant transport mechanism across all test conditions. For all Wo, increase in IT/BT ratio increased the axial flow at early inhalation. In addition, secondary flow after peak inhalation increased during small Wo, and decreased during large Wo. For all Wo increased IT/BT showed increased axial and

secondary flows strength during each phase of exhalation, respectively. As changing IT/BT changes the stroke length (L) of an oscillatory flow, we observed a breakdown in the theoretically expected $Re/Wo^2 = 2L/D$ relation for IT/BT $\neq$ 50%. We developed a modified dimensionless stroke length including IT/BT to correct this discrepancy. While a lower Wo regime was dominated by viscous forces and convective acceleration, unsteady acceleration was dominant for higher Wo.

A central limitation of our study is the simplification of our model geometry. A range of morphological complexities observed from G0–G2, including (but not limited to) asymmetric branching and non-circular lumen of the airway branches, are expected to alter the respiratory flows. The general trends reported here relative to Wo and IT/BT, specifically, the importance of secondary flows with increasing Wo as well as the modified dimensionless stroke length accounting for IT/BT, are expected to be applicable in anatomically realistic airways. Additional model simplifications, such as the use of rigid walled vessels and a sinusoidal flow profile, should also be noted as limitations of this study, while changes to velocity profiles have shown to modestly impact the flow physics (Choi et al., 2010), including airway wall motion has been reported to influence axial and secondary flows compared to rigid-walled airways (Wall and Rabczuk, 2008). Finally, RANS models (such as in this study) have well-known limitations in modeling unsteady turbulent flows and comparing our study findings with higher-fidelity turbulence models (e.g., large eddy simulations) are needed to examine how the choice of turbulence model impacts time-varying flow physics.

3.7 Supplementary

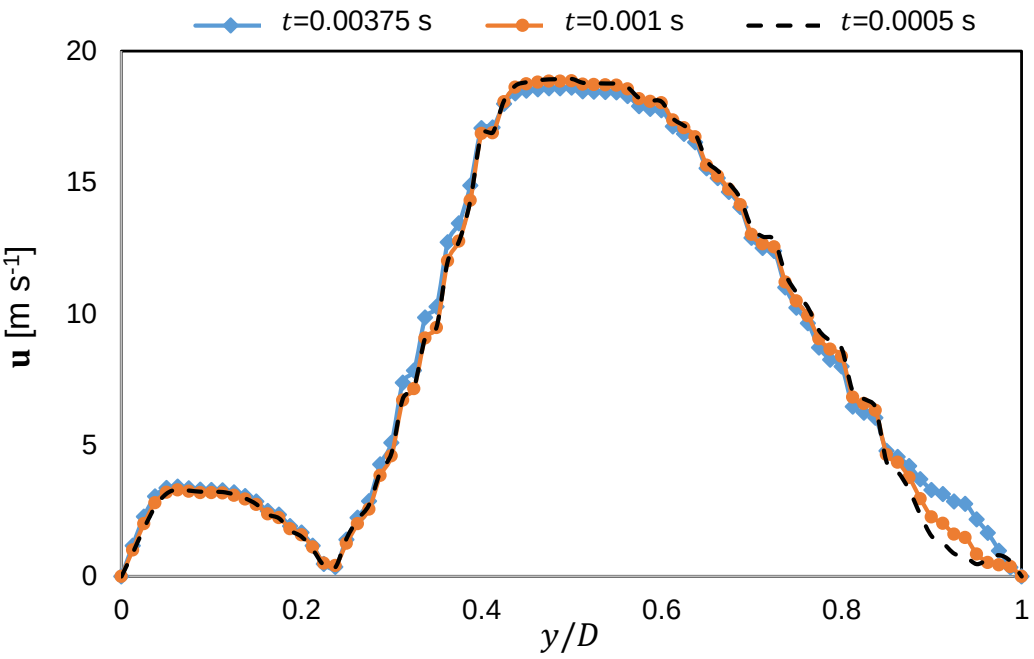

Figure S1. Time-step size independence test for Wo = 24.1 and IT/BT = 50%. Three-dimensional velocity (**u**) was extracted along the coronal plane in the upper trachea (plane 1 in **Table 2**) and plotted as a function ofnondimensional diameter y/D. D = trachea diameter = 18 mm.

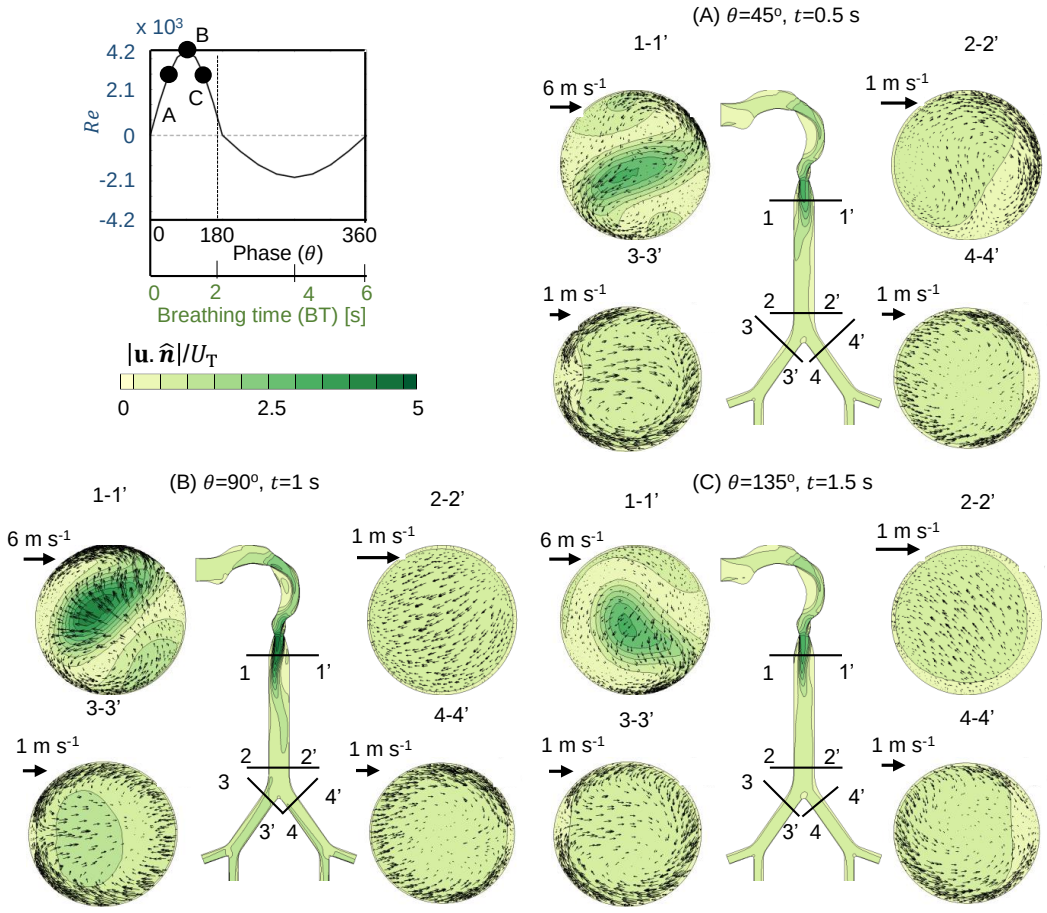

Figure S2. Contours of magnitude of plane-normal velocity component (non-dimensionalized with mean flow speed in trachea, U_T) with superimposed in-plane velocity vectors for planes 1–4 at various time points during inhalation for Wo = 2.41 at IT/BT = 33%. A is at phase $\theta = 45^\circ$ (= 25% IT), B is at phase $\theta = 90^\circ$ (= 50% IT) and C is at phase $\theta = 135^\circ$ (= 75% IT). Coronal plane shows the locations of each plane.

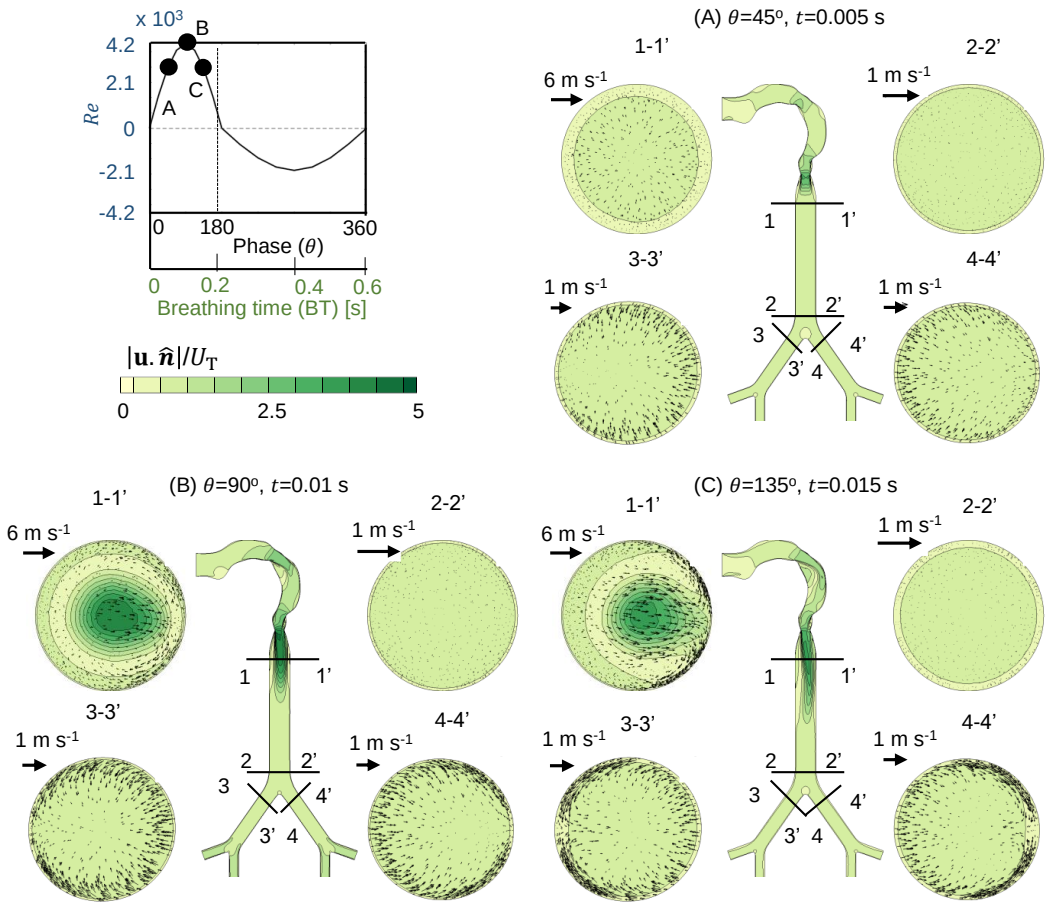

Figure S3. Contours of magnitude of plane-normal velocity component (non-dimensionalized with mean flow speed in trachea, U_T) with superimposed in-plane velocity vectors for planes 1–4 at various time points during inhalation for Wo = 24.1 at IT/BT = 33%. A is at phase $\theta = 45°$ (=25% IT), B is at phase $\theta = 90°$ (= 50% IT) and C is at phase $\theta = 135°$ (= 75% IT).

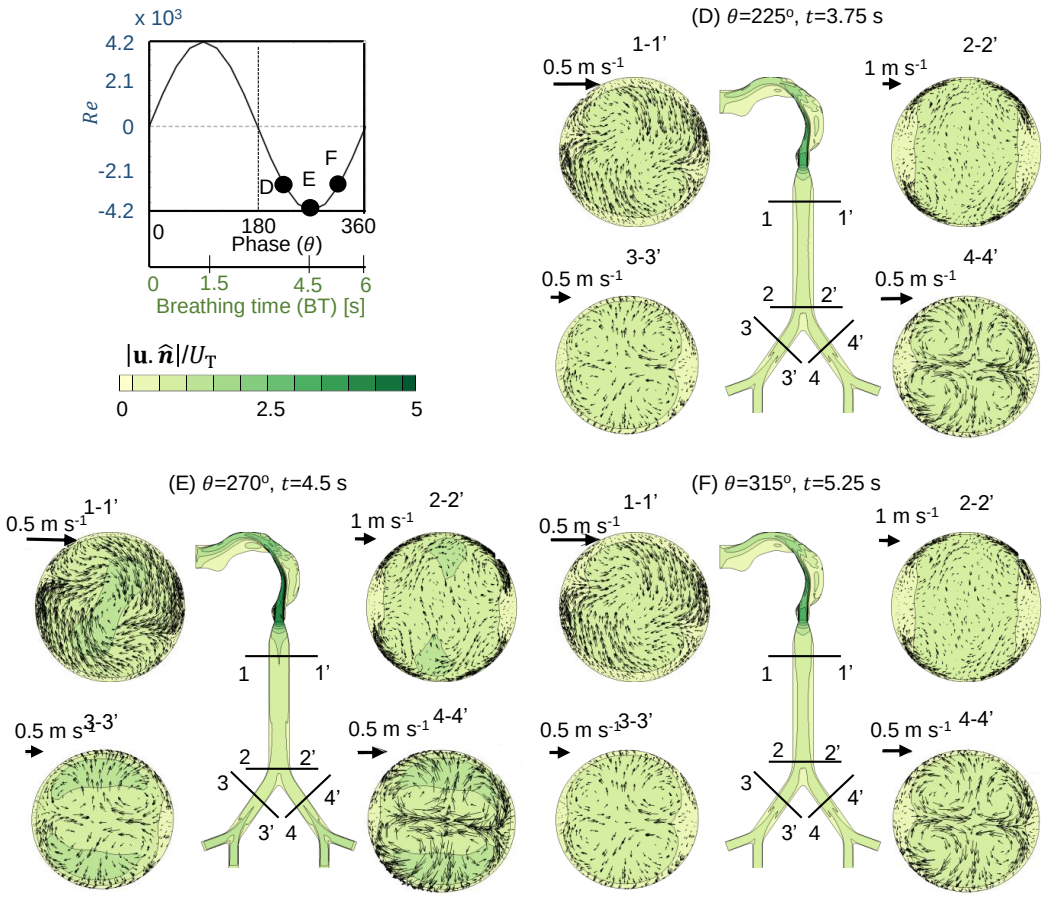

Figure S4. Contours of magnitude of plane-normal velocity component (non-dimensionalized with mean flow speed in trachea, U_T) with superimposed in-plane velocity vectors for planes 1–2 at various time points during exhalation for for Wo = 2.41 at IT/BT = 50%. D is at phase θ = 225° (= 25% ET), E is at phase θ = 270° (= 50% ET) and F is at phase θ = 315° (= 75% ET).

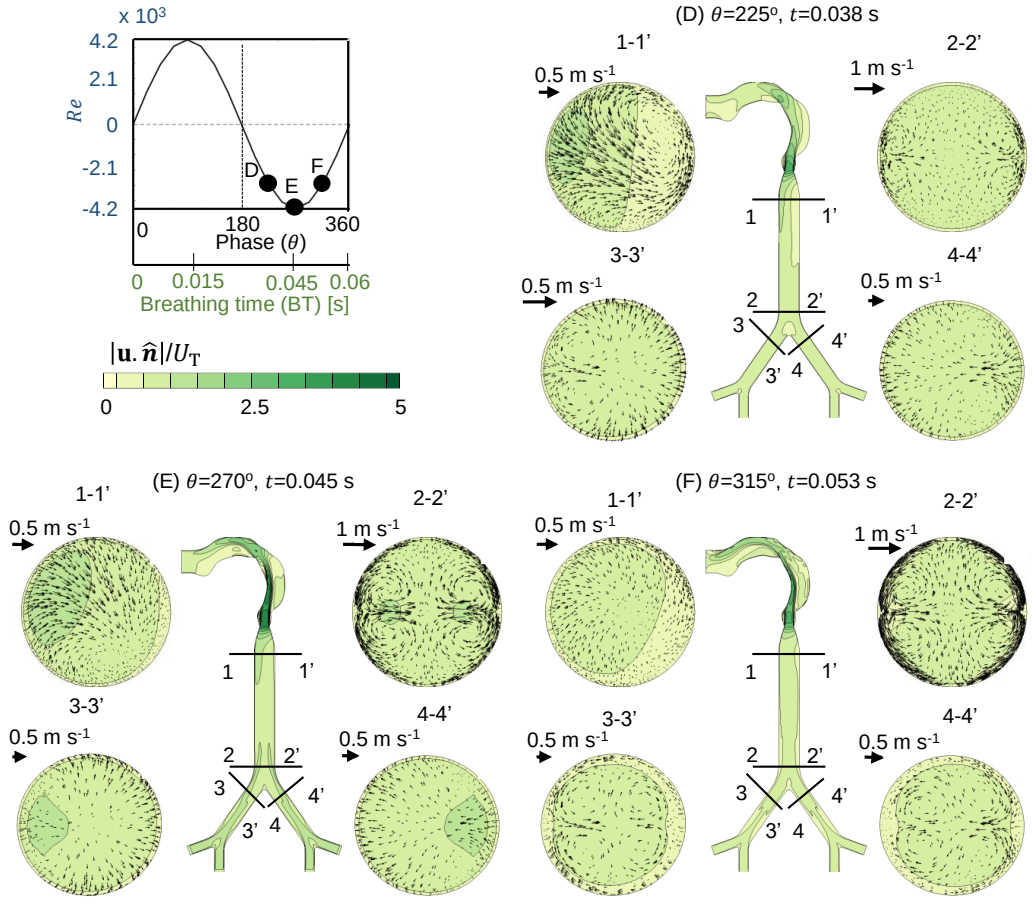

Figure S5. Contours of magnitude of plane-normal velocity component (non-dimensionalized with mean flow speed in trachea, U_T) with superimposed in-plane velocity vectors for planes 1–2 at various time points during exhalation for for Wo = 24.1 at IT/BT = 50%. D is at phase θ = 225° (= 25% ET), E is at phase θ = 270° (= 50% ET) and F is at phase θ = 315° (= 75% ET).

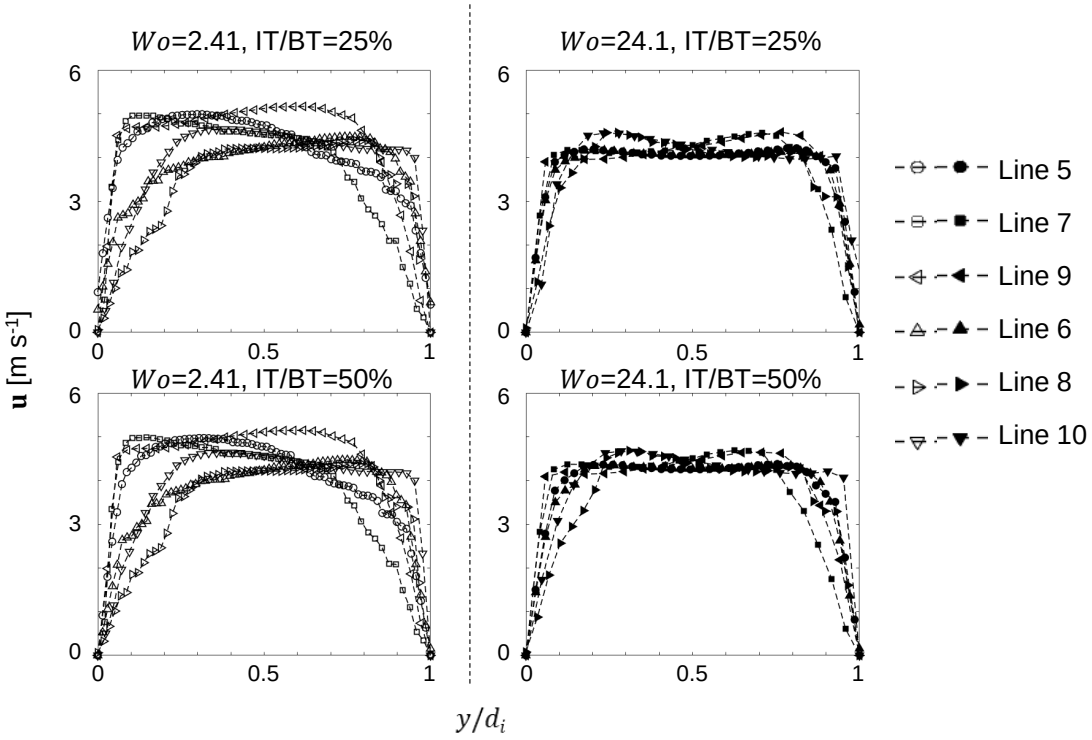

Figure S6. Velocity profiles along coronal plane at in planes 5-10 for varying *Wo* and IT/BT conditions. Three–dimensional velocity (**u**) was extracted along the line across the coronal plane diameter and plotted as a function ofnondimensional diameter y/d_i, where d_i is the airway cross-sectional diameter in i^{th} plane (refer **Table 2)**.

TABLE S1. Local Reynolds number (Re_L) and local Womersley number (Wo_L) at each plane listed in Table 2. Re_L and Wo_L were calculated as: $Re_L = \frac{V_L D_L}{\nu}$ and $Wo_L = \frac{D_L}{2}\sqrt{\frac{1}{\nu}\left(\frac{2\pi}{BT}\right)}$, where D_L is the local airway diameter at a given plane, V_L is the average local axial velocity, BT is the breathing time and ν is the kinematic viscosity of air ($\nu = 1.4\times10^{-5}$ m^2 s^{-1}).

Location	**Description**	$\boldsymbol{Re_L/Wo_L}$								
		Wo = 2.41, IT/BT = 25%	*Wo* = 2.41, IT/BT = 33%	*Wo* = 2.41, IT/BT = 50%	*Wo* = 7.51, IT/BT = 25%	*Wo* = 7.51, IT/BT = 25%	*Wo* = 7.51, IT/BT = 50%	*Wo* = 24.1, IT/BT = 25%	*Wo* = 24.1, IT/BT = 33%	*Wo* = 24.1, IT/BT = 50%
Plane 1	Upper trachea (G0)	6794/2.4	6947/2.4	6894/2.4	6653/7.62	7165/7.61	7418/7.61	6750/24.8	6620/24.8	6602/24.8
Plane 2	Lower trachea (G0)	4224/2.4	4228/2.4	4227/2.4	4210/7.61	4227/7.61	4247/7.61	4141/24.8	4224/24.8	4224/24.8
Plane 3	Generation (G1)	3274/1.63	3276/1.63	3275/1.63	2956/5.15	2947/5.15	3237/5.15	3015/16.3	3076/16.3	3079/16.3
Plane 4	Generation (G1)	3932/1.63	2933/1.63	2934/1.63	3235/5.15	3267/5.15	2984/5.15	3056/16.3	3118/16.3	3121/16.3
Plane 5	Generation (G1)	3311/1.63	3315/1.63	3313/1.63	2992/5.15	2932/5.15	3264/5.15	3058/16.3	3119/16.3	3119/16.3
Plane 6	Generation (G1)	2930/1.63	2931/1.63	2932/1.63	3229/5.15	3261/5.15	2980/5.15	3057/16.3	3119/16.3	3120/16.3
Plane 7	Generation (G2)	2348/1.11	2359/1.11	2354/1.11	2135/3.53	2130/3.53	2324/3.53	2260/11.18	2307/11.18	2311/11.18
Plane 8	Generation (G2)	2090/1.11	2104/1.11	2096/1.11	2284/3.53	2310/3.53	2118/3.53	2251/11.18	2298/11.18	2302/11.18
Plane 9	Generation (G2)	2535/1.11	2531/1.11	2533/1.11	2278/3.53	2271/3.53	2489/3.53	2239/11.18	2286/11.18	2290/11.18
Plane 10	Generation (G2)	2233/1.11	2221/1.11	2230/1.11	2468/3.53	2487/3.53	2270/3.53	2238/11.18	2285/11.18	2290/11.18

CHAPTER IV

SA 2: FLUID DYNAMICS OF ABNORMAL BREATHING PATTERNS

4.1 Abstract

Several physiological and pathological conditions can alter respiratory rate (RR) and peak airflow rate from those observed in normal conditions (NC). Studies of airflow patterns and particle transport in the human airway have mainly focused on NC. By contrast, the fluid dynamics of abnormal breathing patterns is not well understood. Using three-dimensional computational fluid dynamics (CFD) simulations on an idealized human airway model consisting of a mouth, glottis, trachea and symmetric double bifurcation, we examined airway flow characteristics and transport of massless particles for the following abnormal breathing patterns: tachypnea (TC; $\sim$ 1.5x increase in RR), bradypnea (BC; $\sim$ 1.5x decrease in RR), hyperpnea (HC; deep breathing with abnormally large peak flow rate), and hypopnea (SC; shallow breathing with abnormally low peak flow rate). Peak jet length (L_{j}) in the trachea during inhalation was lower in tachypnea and higher in normal with increase in breathing duration; and increased along with increase in peak inhalation flow rate ($L_{\mathrm{j,SC}} < L_{\mathrm{j,NC}} < L_{\mathrm{j,HC}}$). Cumulative exhaled particle ratio (defined as the ratio of cumulative exhaled particles accumulated at the mouth at an instant to the total number of particles introduced at the outlets) increased with breathing duration during early exhalation phase compare to normal and tachypnea, and along with increased peak exhalation flow rate ($R_{4,\mathrm{SC}} < R_{4,\mathrm{NC}} \approx R_{4,\mathrm{HC}}$).

4.2 Introduction

Involuntary and unlabored breathing in normal condition (NC), also known as *eupnea*, is defined as respiratory rate (RR) ranging from 10-15 breaths per minute (bpm), tidal volume (TV) ranging from 350-650 mL and inhalation time (IT) to breathing time (BT) ratio (i.e., IT/BT) ranging from 33-50%. RR and depth of breaths (latter indicative of peak airflow rates) in involuntary nasal breathing are controlled by chemical interactions within the neural system. Malfunctions in the neural system can lead to disorders in breathing (Cherniack and Fishman, 1975) and consequently impair gas exchange. Dysfunctional or abnormal breathing patterns are used as umbrella terms to commonly describe such breathing disorders (Boulding et al., 2016). Variations in RR from normal breathing is an indication of human disease (Ott, 1912; Cherniack and Fishman, 1975). However, humans can breathe through the nose and/or mouth during illness and facilitate gas exchange in higher airway generations (Gilbert, 2014). Previous investigations showed an instance of quick and less effort mouth breathing (Gilbert, 2014), or altered manipulated breathing (Tiller et al., 1987) as a response to these dysfunctional breathing patterns. There are several abnormal breathing patterns, such as *tachypnea* (denoted here as TC) where RR is 1.5x-2x greater than RR in NC, *bradypnea* (denoted here as BC) where RR is 1.5x-2x less than RR in NC, deep breathing or *hyperpnea* (denoted here as HC) where RR is in the same range as in NC but TV is greater than that of NC, and shallow breathing or *hypopnea* (denoted here as SC) where RR is in the same range as in NC but TV is less than that of NC (see Whited and Graham (2019) for more details). Early evaluation of such abnormal breathing patterns can aid clinicians in disease detection (Whited and Graham, 2019). The majority of studies examining flow patterns and particle deposition in the human airway have been restricted to NC (Zhang and Kleinstreuer, 2002; Soodt et al., 2013). Studies examining fluid dynamics of abnormal breathing patterns are needed to characterize lung ventilation in pathological conditions.

During breathing, O_2 rich air is inhaled and CO_2 rich air is exhaled with $\sim$5% of ex-

halation TV being released in every breath (Dhami et al., 2015), facilitating arterial and alveolar gas exchange. Levels of O_2 and CO_2 can vary due to ongoing physiological activities, causing either respiratory acidosis due to increase in blood CO_2 concentration or respiratory alkalosis due to decrease in blood CO_2 concentration (Eichenholz, 1965). Whited and Graham (2019) reported respiratory alkalosis in hyperpnea and respiratory acidosis in hypopnea. The level of CO_2 can also vary due to a person's metabolic condition, causing metabolic acidosis or metabolic alkalosis, potentially leading to decrease in cardiac output and arterial dilatation among others (Kraut and Madias, 2010). Studies investigating the effects of varying inhalation and exhalation flow rates on facilitating gas exchange are limited. Fluid dynamic studies estimating gas exchange as a function of varying inhalation and exhalation flow rates can be useful in identifying treatment guidelines.

The objective of this study was to characterize fluid dynamics and particle transport during abnormal breathing. Three-dimensional (3D) computational fluid dynamics (CFD) simulations were performed on an idealized human airway model for a range of oscillatory velocity profiles, varying peak inhalation and exhalation flow rates as seen in hyperpnea and hypopnea, as well as varying RR as seen in tachypnea and bradypnea. Since complex geometrical variations (e.g., changing curvature, contractions, expansions and bifurcations) were observed in the human airway (Haghnegahdar et al., 2018) along with inter-subject variability (Feng et al., 2016), an idealized airway was used for this study. Particle transport through the airway and implications for gas exchange were examined from the simulations.

4.3 Methods

A symmetric airway model with an idealized mouth-to-glottis section (Figure 4.1A), previously used in Feng et al. (2016) and Gaddam and Santhanakrishnan (2021), was designed in Solidworks software (Dassault Systèmes, SolidWorks Corporation, Waltham, MA). The airway geometry was symmetric with respect to the sagittal plane (x-y plane at z=0 m in Figure 4.1A). The coronal plane was defined perpendicular to the sagittal plane (i.e., x-z

plane at y=0.072 m in Figure 4.1A). The airway geometry consisted of glottis with circular cross-section (8 mm internal diameter), trachea corresponding to Generation 0 (G0) with a circular cross-section of internal diameter (D) of 18 mm, 1st generation (G1) with an internal diameter of 12.2 mm, and 2nd generation (G2) with an internal diameter of 8.3 mm. The lengths of generations G0, G1, and G2 were 120 mm, 48 mm, and 19 mm, respectively. The geometry file was loaded into ANSYS ICEM-CFD 2020 R2 for mesh generation. Volume meshes were subsequently developed using tetrahedral cells with 5 prism layers on the walls. The maximum y^+ for all the meshes at peak inhalation of HC was $<$5 and was observed near in very small region contraction from larynx to glottis. k-ω SST turbulence model was finalized for given y^+ conditions (refer to Zhang et al. (2009); Tu et al. (2012) for more details). Details of model selection are available in Gaddam and Santhanakrishnan (2021).

Transient, 3D flow simulations were performed using Fluent (ANSYS 2020 R2) k-ω SST turbulence model with the low Reynolds number correction. To examine particle transport, discrete phase method (DPM) was performed with massless particles (no density and no drag forces) introduced at two surfaces: one at the inlet at the start of inhalation (particle number=2,920) and the other at the outlets at the start of exhalation (particle number=2,746). Particles were one-way coupled with the fluid flow (i.e., flow influences particle transport, but not vice versa) and particle-particle interactions were neglected. The particles served to trace the airflow pattern (Tu et al., 2012) and were used to examine how flow can influence gas uptake (Segal et al., 2008). RR=15 bpm (corresponding to BT=60/RR=4 s), IT/BT=33.3% and TV=500 mL were used to define inlet oscillatory velocity profiles for NC simulations. The peak inhalation flow rate ($Q_{\text{in,peak}}$) was first calculated from TV using the relation:

$$Q_{\text{in,peak}} = TV\left(\frac{\pi}{2\,IT}\right). \tag{4.1}$$

For TV=500 mL and IT=33.3% of BT=4 s that were used to define NC, $Q_{\text{in,peak}}$=35.38 L min^{-1}. Peak exhalation flow rate ($Q_{\text{ex,peak}}$) corresponding to $Q_{\text{in, peak}}$ was next calculated

using the following equation:

$$Q_{\text{ex,peak}} = Q_{\text{in,peak}} \left(\frac{IT}{BT - IT} \right). \tag{4.2}$$

Sinusoidal velocity profiles were defined as a function of $Q_{\text{in,peak}}$ and $Q_{\text{ex,peak}}$ via the relations:

$$V_{\text{in}}(t) = \frac{Q_{\text{in,peak}}}{A_{\text{in}}} \sin\left(\frac{\pi t}{IT} \right),\ 0 < t < IT \tag{4.3}$$

$$V_{\text{ex}}(t) = \frac{Q_{\text{ex,peak}}}{A_{\text{in}}} \sin\left(\frac{\pi (IT - t)}{BT - IT} \right),\ IT \leq t < BT \tag{4.4}$$

where t is time, $V_{\text{in}}(t)$ is inhalation velocity profile prescribed at the mouth (Figure 4.1B), A_{in} is inlet (mouth) area based on diameter D_{in}=20 mm, and $V_{\text{ex}}(t)$ is exhalation velocity profile prescribed at the mouth (Figure 4.1B). Inlet velocity profiles for TC and BC were obtained from eqns (2)–(4) by varying RR (and hence BT and IT), and with the same $Q_{\text{in,peak}}$ as that of NC (Table 4.1). Inlet velocity profiles for SC were obtained from eqns (2)–(4) for $Q_{\text{in,peak}}$=20 L min^{-1} ($\sim$44% decrease in $Q_{\text{in,peak}}$ relative to that of NC), and with the same RR as that of NC (Table 4.1). Inlet velocity profiles for HC were obtained from eqns (2)–(4) for $Q_{\text{in,peak}}$=50 L min^{-1} ($\sim$41% increase in $Q_{\text{in,peak}}$ relative to that of NC), and with the same RR as that of NC (Table 4.1). IT/BT=33.3% (used for NC) was unchanged across all abnormal breathing patterns (i.e., TC, BC, SC, HC).

For abnormal breathing conditions, TVs for TC, BC, SC and HC were calculated using a modified form of eqn (1) with prescribed $Q_{\text{in,peak}}$ and RR values (TV=$Q_{\text{in,peak}}$(2 IT/π), values in Table 4.1). Reynolds number (Re) was calculated at the inlet and trachea during peak inhalation and peak exhalation phases (Table 4.1) using the equation:

$$Re = \frac{VD}{\nu}, \tag{4.5}$$

where V is the average velocity through the airway region of interest, ν is the kinematic viscosity of air (1.46×10^{-5} m^2 s^{-1}) and D is the hydraulic diameter of the airway region

Table 4.1: Velocity profile parameters for each breathing condition in the current study. NC=normal condition, TC=tachypnea condition, BC=bradypnea condition, SC=hypopnea condition, HC=hyperpnea condition, RR=respiratory rate, BT=breathing time (BT=60/RR), IT=inhalation time (IT=33.3% BT), ET= exhalation time (ET=BT-IT), $Q_{\text{in,peak}}$= peak inhalation flow rate, $Q_{\text{ex,peak}}$=peak exhalation flow rate, TV=tidal volume, $Re_{\text{I,in,peak}}$=Reynolds number of flow through the inlet at peak inhalation, $Re_{\text{T,in,peak}}$=Reynolds number of flow through the trachea at peak inhalation, $Re_{\text{I,ex,peak}}$=Reynolds number of flow through the inlet at peak exhalation, and $Re_{\text{T,ex,peak}}$=Reynolds number of flow through the trachea at peak exhalation, MV=minute volume.

Parameter	**NC**	**TC**	**BC**	**SC**	**HC**
RR [bpm]	15	22.5	10	15	15
BT [s]	4	2.667	6	4	4
IT [s]	1.332	0.888	1.998	1.332	1.332
ET [s]	2.668	1.779	4	2.668	2.668
$V_{\text{in,peak}}$ [m s^{-1}]/$Q_{\text{in,peak}}$ [L min^{-1}]	1.877/35.38	1.877/35.38	1.877/35.38	1.061/20	2.653/50
$V_{\text{ex,peak}}$ [m s^{-1}]/$Q_{\text{ex,peak}}$ [L min^{-1}]	0.937/17.66	0.937/17.66	0.937/17.66	0.53/9.99	1.324/24.96
TV [mL]	500	333	750	283	707
$Re_{\text{I,in,peak}}$/$Re_{\text{T,in,peak}}$	2570/2856	2570/2856	2570/2856	1453/1615	3633/4036
$Re_{\text{I,ex,peak}}$/$Re_{\text{T,ex,peak}}$	1283/1426	1283/1426	1283/1426	725/806	1814/2015
MV [L]	7.5	7.5	7.5	4.24	10.6

of interest. Minute volume (MV), defined as the volume of air inhaled or exhaled in one minute, was calculated for each breathing pattern using the following equation:

$$\text{MV} = (\text{TV})(\text{RR}). \tag{4.6}$$

Though TVs for NC, TC, and BC were different, MVs were equal for these three conditions. MV was highest for HC and lowest for SC (Table 4.1).

Boundary conditions include prescribed inlet velocity profiles, zero pressure outlets, and no-slip walls. All the velocity profiles consists of positive inhalation velocities (θ=0-180° in Figure 4.1B) and negative exhalation velocities (θ=180-360° in Figure 4.1B). The solution method includes a coupled scheme, second-order spatial discretization, and second-order upwind scheme for turbulence kinetic energy. A uniform time step (δt) equal to 2% BT was used for simulations. Mesh independence and time step independence tests were performed for NC on 3 different meshes similar to those described in Gaddam and Santhanakrishnan (2021). The final mesh used for this study consisted of 2.5×10^6 tetra-

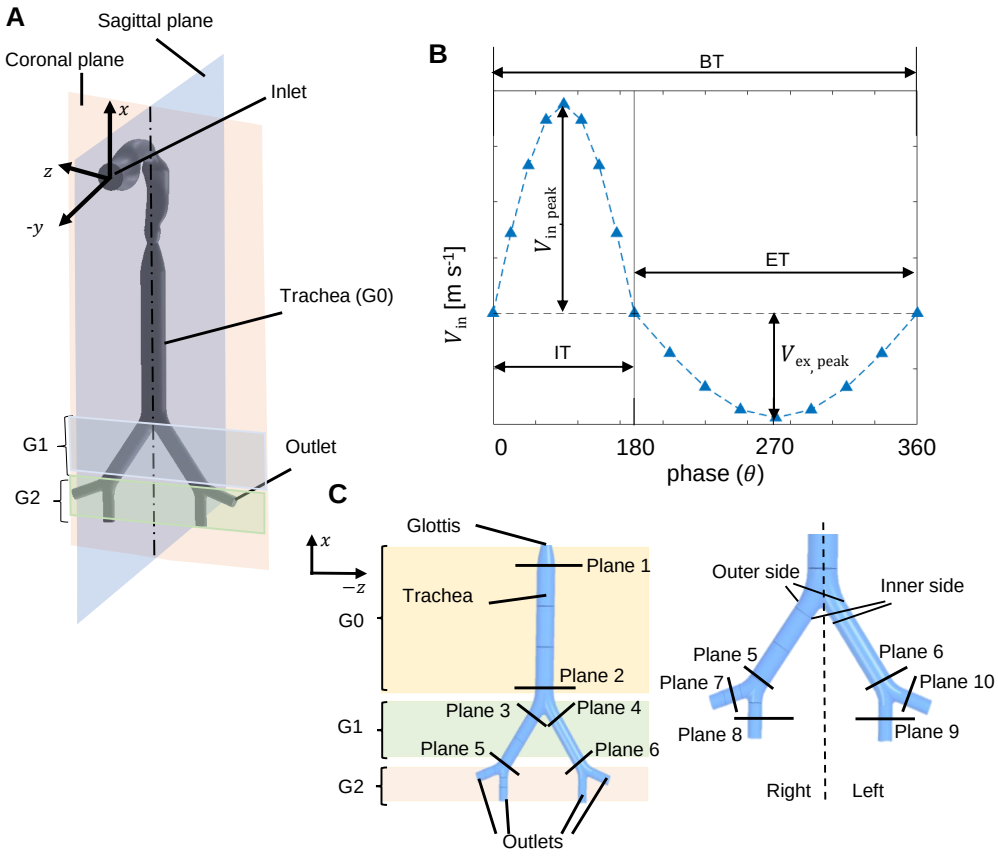

Figure 4.1: (A) Airway geometry used in this study, consisting of a mouth, glottis, and 2 generations (G) that include a trachea (G0) and symmetric double bifurcation (G1, G2). Locations of the sagittal plane, coronal plane, inlet and outlets are shown. (B) Oscillatory velocity profile prescribed at the inlet (V_{in}). BT=breathing time, IT=inhalation time, ET=exhalation time, $V_{in,peak}$=peak inhalation velocity at the inlet, $V_{ex,peak}$=peak exhalation velocity at the inlet. Values of the different breathing parameters are provided in Table 4.1. (C) Airway generations G0-G2 showing locations of Planes 1–10 (coordinates given in Table 4.2), and anatomical left and right sides.

hedral elements. Three different time steps (0.5% BT, 2% BT, 4% BT) were used in time independence tests (for NC), and the final time step of 2% BT was used for all studies due to lower computational costs and better accuracy. All simulations were auto-saved at θ=12.5°. Solution files were then exported and processed in Tecplot 360 EX 2018 R1 for analysis of secondary flow fields, and in CFD-Post (ANSYS 2020 R2) for analysis of inhalation jet lengths. For all the test conditions, velocity magnitude contours were exported and analyzed along multiple planes (Table 4.2) at various inhalation and exhalation phases.

To validate the simulations, pressure drop (Δp) across the airway model was calculated

Table 4.2: Geometric planes used for analysis of the airway model used in this study.

Plane	**Description**	(x, y, z) **[mm]**	$(\theta_x, \theta_y, \theta_z)$ $[^o]$	**Diameter [mm]**
Sagittal	-	(0, 0, 0)	(0, 0, 90)	
Coronal	-	(0, 72, 0)	(0, 90, 0)	
Plane 1	Upper trachea (G0)	(-77, 0, 0)	(90, 0, 0)	18
Plane 2	Lower trachea (G0)	(-172, 0, 0)	(90, 0, 0)	18
Plane 3	Generation 1 (G1)	(-189, 72, 7)	(-55, 0, 35)	12.2
Plane 4	Generation 1 (G1)	(-189, 72, -7)	(-55, 0, -35)	12.2
Plane 5	Generation 1 (G1)	(-228, 72, 34)	(-55, 0, 35)	12.2
Plane 6	Generation 1 (G1)	(-228, 72, -34)	(-55, 0, -35)	12.2
Plane 7	Generation 2 (G2)	(-234, 72, 44)	(-30, 0, 70)	8.3
Plane 8	Generation 2 (G2)	(-240, 72, 36)	(90, 0, 0)	8.3
Plane 9	Generation 2 (G2)	(-240, 72, -36)	(90, 0, 0)	8.3
plane 10	Generation 2 (G2)	(-234, 72, -44)	(30, 0, 70)	8.3

at peak inhalation and compared to those reported in previous studies of idealized, subject-specific and upper airway truncated airway models. Also, mean pressures were calculated across the airway at the inlet, glottis, lower trachea, G1 (average of Planes 5–6) and G2 (average of Planes 7–10) at peak inhalation and peak exhalation. Velocity profiles at Planes 2,5–10 were extracted along the coronal plane during inhalation (θ=45°, 90° and 135°) and at peak exhalation for axial flow analysis. Velocity magnitude isosurface of 50% of average in-plane velocity at glottis from NC during peak inhalation was generated at all inhalation phases to measure the inflow jet length (L_{j}), defined as the distance between Plane X (plane through the glottis) and Plane A (plane parallel to Plane X and cutting through the tip of the isosurface in the trachea). The peak jet lengths were non-dimensionalized using peak jet length of NC to measure jet streaming (J_{S}).

Four non-dimensional parameters were used for analysis of particle transport, including instantaneous inhaled particle deposition (R_1), cumulative inhaled particle deposition (R_2), instantaneous exhaled particle ratio (R_3) and cumulative exhaled particle ratio (R_4). Instantaneous inhaled particle deposition (R_1) was defined as the ratio of number of inhaled particles at outlets during an instant in the inhalation to the total number of particles introduced at the inlet. Cumulative inhaled particle deposition (R_2) was defined as the ratio of cumulative inhaled particles (accumulated at the outlets) at an instant to the total number

of particles introduced at the inlet. Similarly, instantaneous exhaled particle ratio (R_3) was defined as the ratio of number of exhaled particles at an instant in the exhalation to the total number of particles introduced at the outlets. Cumulative exhaled particle ratio (R_4) was defined as the ratio of cumulative exhaled particles (accumulated at the mouth) at an instant to the total number of particles introduced at the outlets.

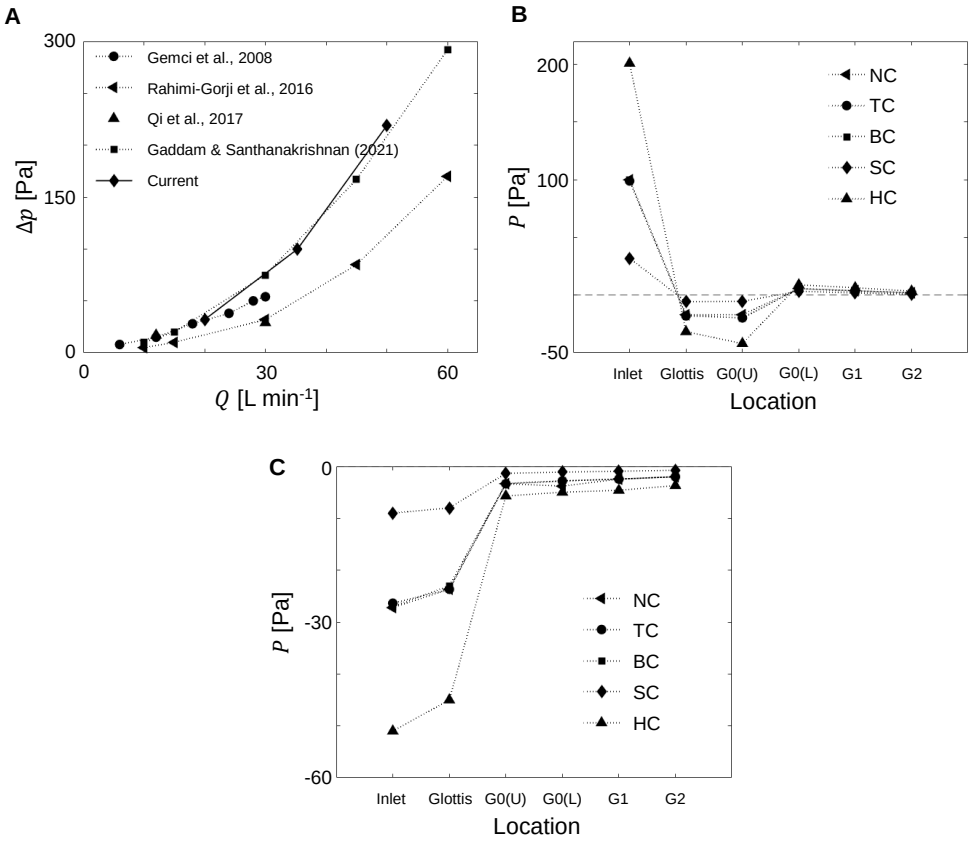

Figure 4.2: (A) Airflow rate (Q) vs. pressure drop (Δp) for current study at peak inhalation compared to those reported in previous studies. Mean pressure (P) across airway generations for all test conditions from transient 3D simulations in the current study, at (B) peak inhalation, and (C) peak exhalation.

4.4 Results and Discussion

4.4.1 Model validation

Pressure drop (Δp) was measured during peak inhalation for all the breathing conditions to validate the current airway model. Δp was compared with those reported in previous stud-

ies with whole airway model (Rahimi-Gorji et al., 2016), truncated airway model (Gemci et al., 2008), subject-specific airway model (Qi et al., 2017), and mouth-to-glottis rotated model (similar geometry) in Figure 4.2A. Our results showed an identical trend of pressure drop as a function of airflow rate as compared to previous studies, such that increase in airflow rate (Q) increased Δp. The variations in the pressure drop values are likely due to differences in the airway geometry across the different studies, similar to our recent study with nearly similar mouth-to-glottis rotated along coronal plane geometry (Gaddam and Santhanakrishnan, 2021). For all breathing conditions, mean pressure across each generation was measured at peak inhalation and peak exhalation (Figures 4.2B,C). Mean pressure at peak inhalation decreased sharply across the mouth-to-glottis section, followed by increased mean pressure until lower trachea, later decreased with increasing generation and finally reached 0 Pa in the last generation. Figure 4.2C showed an increase in mean pressure from mouth to upper trachea and further slightly increased until G2, facilitating exhalation airflow for all breathing conditions.

Comparing across NC, TC and BC conditions, mean pressure across the airway remained the same at peak inhalation and peak exhalation with increasing BT (i.e., decreasing RR). With varying peak flow rates, HC showed a significant decrease in mean pressure than NC and SC showed a lesser decrease in mean pressure than NC, at both peak inhalation and peak exhalation.

4.4.2 Velocity Profiles

Radial distribution of 3D velocity magnitude during inhalation, extracted along the coronal plane, was examined for all breathing conditions at the lower trachea (Plane 2; Figure 4.3(A)–(C)), G1 (Planes 5–6; Figure 4.3(D)–(I)), and G2 (Planes 7–10; Figure S1). For NC, velocity magnitude distribution across Plane 2 increased uniformly from early inhalation until peak inhalation and later decreased in magnitude (refer to Figure 4.3(A)–(C)). Similar trends as NC were observed for all conditions across inhalation at plane 2. The

radial distribution of velocity magnitude at early inhalation was more uniform for BC and HC as compared to NC, TC and SC.

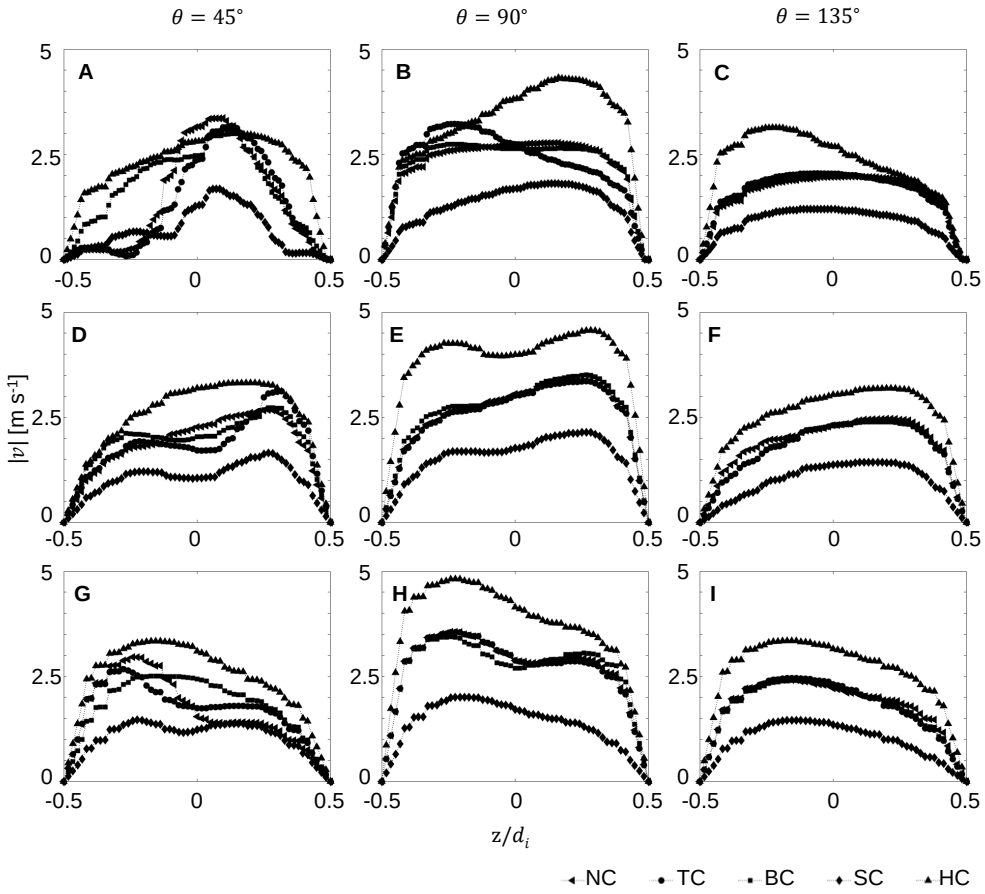

Figure 4.3: Three-dimensional velocity magnitude ($|v|$) extracted along the coronal plane at (A)–(C) Plane 2 (top row), (D)–(F) Plane 5 (middle row) and (G)–(I) Plane 6 (bottom row) at early inhalation (θ=45° corresponding to 25% IT in (A), (D), (G)), peak inhalation (θ=90^o corresponding to 50% IT in (B), (E), (H)) and late inhalation (θ=180^o corresponding to 75% IT in (C), (F), (I)). d_i indicates airway diameter of a particular plane.

Velocity distribution at Plane 5 (Figure 4.3(D)–(F)) was nearly identical for all conditions and followed the inlet velocity profile, i.e., increasing from early inhalation until peak inhalation and later decreasing until late inhalation. In addition, velocity profiles were skewed towards the anatomical right side (z/d_i=0.5) throughout inhalation at Plane 5. Similar trends were observed in velocity profiles at Plane 6 for all breathing conditions (Figures 4.3(G)–(I)), but with anatomical left (z/d_i=-0.5) skewed profiles throughout inhalation.

Velocity profiles at planes 7–10 (Figure S1 in the Supplementary Material) showed similar trends as those observed at Plane 5 for all breathing conditions. Velocity profiles were skewed to the anatomical right side at Plane 7 (Figure S1(A)–(C) in the Supplementary Material) and Plane 9 (Figure S1(G)–(I) in the Supplementary Material), and skewed to the anatomical left side at Plane 8 (Figure S1(D)–(F) in the Supplementary Material) and Plane 10 (Figure S1(J)–(L) in the Supplementary Material).

Comparing across all the planes, airflow at the lower trachea (Plane 2) was narrowly distributed during early inhalation (θ=45°) for NC, TC and SC. Axial flow changed from narrow distribution in the lower trachea to skewed flow in the higher generations with changing RR (TC, NC, BC; refer to Figure 4.3A,D,G and Figure S1A,D,G,J in the Supplementary Material). At both peak and late inhalation, velocity magnitude was unaffected with changing RR across NC, TC and BC at a given plane and phase. Further, axial flow decreased in strength from the lower trachea to higher generations at all the inhalation phases. Comparing SC, NC and HC, with an increase in $Q_{\text{in,peak}}$, axial flow increased in strength for a given plane and phase. At early inhalation in the lower trachea, axial flow changed from narrow to uniform flow with an increase in inhalation flow rate (Figure 4.3A). In addition, within left (Planes 7,8) and right (Planes 9,10) bifurcations, each bifurcation showed oppositely skewed velocity profiles.

Radial distribution of 3D velocity magnitude at peak exhalation are shown at Planes 2,5–10 in Figure 4.4. At Plane 2, nearly uniform velocity profiles of similar magnitude were observed for NC, TC, BC and HC (Figure 4.4A). In comparison, SC showed a uniform velocity profile but of lower magnitude. The velocity distribution for a given breathing pattern remained the same across Generation 1 (Plane 5, Figure 4.4B), with slightly larger magnitude as compared to Plane 2 but with narrower radial extent of constant magnitude. At Generation 2 (Planes 7–10, Figures 4.4C–4.4F), the strongest velocity magnitude was observed for NC. TC and BC showed no differences in velocity magnitude and distribution in Generation 2. While the velocity magnitude increased from SC to NC, and decreased

in HC with an increase in peak exhalation flow rates in Planes 7–10. Overall, NC showed the largest velocity magnitude at peak exhalation when moving from the lower trachea to higher generations.

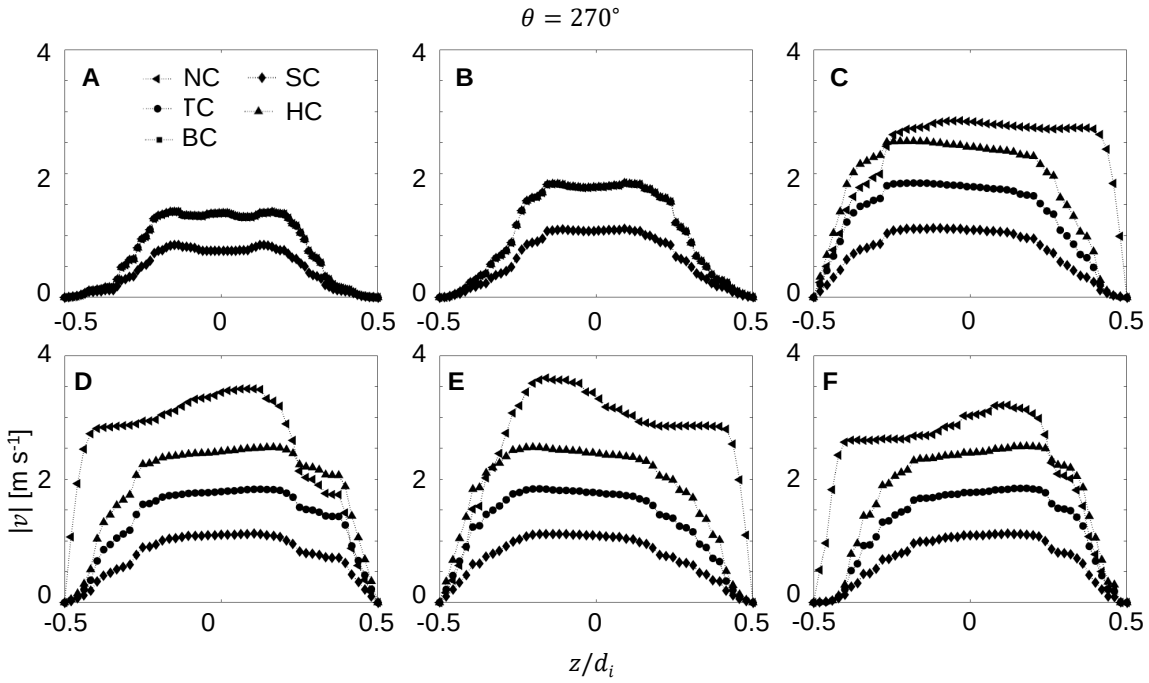

Figure 4.4: Three-dimensional velocity magnitude ($|v|$) extracted along the coronal plane at (A) Plane 2, (B) Plane 5, (C) Plane 7, (D) Plane 8, (E) Plane 9 and (F) Plane 10 at peak exhalation (θ=270° corresponding to peak exhalation. d_i indicates airway diameter of a particular plane.

4.4.3 Tracheal Jet Characteristics During Inhalation

Figure 4.5A shows the jet length in the trachea during inhalation for all breathing conditions. Jet length of NC followed time variation similar to the prescribed inflow velocity profile, i.e., L_j for NC increased from the start of inhalation (θ=0°) until peak inhalation (θ=90°) and later decreased until the end of inhalation (refer to **Movie SA2** in Supplementary Material). Increasing RR from NC to TC advanced the time to peak L_j to θ=67.5°, and decreasing RR from NC to BC delayed the time to peak L_j to θ=112.5°. Peak L_j was essentially unchanged between NC and BC, but decreased for TC. Increasing peak inhalation flow rate from NC to HC markedly increased peak L_j but did not modify the time to

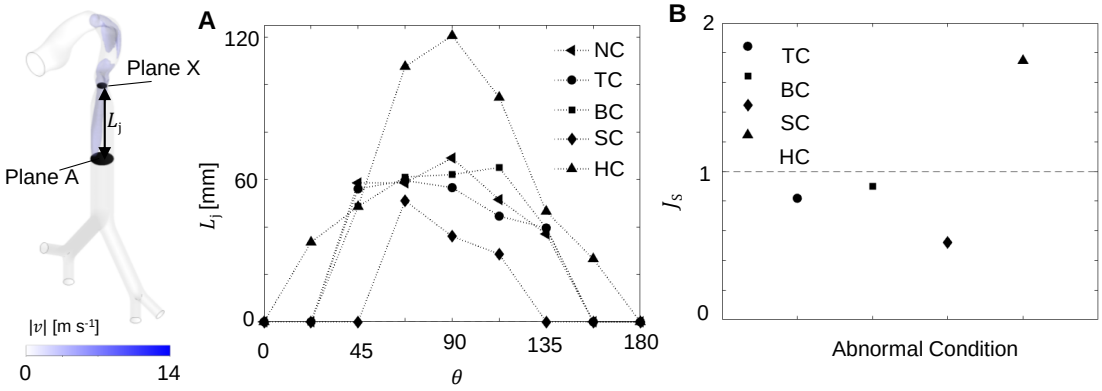

Figure 4.5: Tracheal jet characteristics during inhalation (θ=0°–90°) for all breathing conditions. (A) Jet length (L_j). (B) Jet streaming (J_S) at peak inhalation (θ=90°), defined as the ratio of L_j of an abnormal breathing condition at θ=90° relative to L_j of NC at θ=90° (dashed line). Inset shows isosurface of velocity magnitude, Plane X and Plane A (used for measuring jet length (L_j)).

peak L_j (i.e., θ=90°). Decreasing peak inhalation flow rate from NC to SC lowered peak L_j value and advanced time to peak L_j to θ=67.5°. Overall, jet lengths at peak inhalation (θ=90°) followed the order $L_{j,HC} > L_{j,NC} > L_{j,BC} > L_{j,TC} > L_{j,SC}$.

Jet lengths at peak inhalation (i.e., θ=90°) were non-dimensionalized with jet length of NC at peak inhalation ($L_{j,NC}|_{\theta=90°}$) to characterize jet streaming in abnormal breathing conditions relative to NC (J_S in Figure 4.5B). Jet streaming of $J_{S,HC}$ was greater than those of other abnormal breathing conditions. For a fixed RR, HC has the most jet penetration and SC has the least jet penetration. This can be expected to affect particle deposition during inhalation. For a fixed peak inhalation flow rate, increasing breathing time (decreasing RR) from TC to BC moderately increased jet streaming in the trachea.

4.4.4 Particle Deposition During Inhalation

To characterize the effects of the observed flow fields on particle deposition during inhalation, non-dimensional inhaled particle deposition (instantaneous, R_1 and cumulative, R_2) were determined at the outlets (Figure 4.6A,B). All breathing conditions showed increased inhaled particle deposition during early inhalation ($\theta < 90°$ in Figure 4.6A), followed by a decrease until the end of inhalation (θ=180° in Figure 4.6A). At peak inhala-

tion (θ=90°), inhaled particle deposition (R_1) followed the order of $R_{1,TC} > R_{1,SC} \approx R_{1,NC} > R_{1,HC} > R_{1,BC}$. However, peak values of R_1 followed the order $R_{1,BC} > R_{1,NC} > R_{1,HC} > R_{1,TC} > R_{1,SC}$. This suggests that differences in unsteady flow patterns between peak and late inhalation can markedly alter particle deposition at the outlets.

Cumulative particle count at a given phase was non-dimensionalized by the prescribed inlet particle count to examine cumulative inhaled particle deposition (R_2) across all breathing conditions (Figure 4.6B). All breathing conditions showed a similar trend, i.e., no particle was inhaled until early inhalation (θ=45°), followed by increased particle deposition until the end of inhalation (θ=180°). R_2 at peak inhalation (θ=90°) followed the order of $R_{2,NC} > R_{2,BC} > R_{2,HC} > R_{2,TC} > R_{2,SC}$. At the end of inhalation, R_2 was largest for NC and lowest for SC. The other breathing conditions (TC, BC, HC) showed almost the same R_2 at θ=180°.

Comparing between NC and HC, the particles deposited during NC in inhalation was higher than HC and minute ventilation for NC is lower than HC, which would be an efficient in drug delivery system, where large amount of drug need to be deposited at target for less volume of inhaled drug. The inhalation deposition was higher in BC during early inhalation phase compared to NC, which was higher than TC showing that though the minute ventilation was same, smaller RR can increase the particle deposition during inhalation.

4.4.5 Particle release during exhalation

To characterize the effects of the observed flow fields on particle exhalation, non-dimensional exhaled particle ratios were calculated at the mouth. Figure 4.6C,D shows the instantaneous (R_3) and cumulative (R_4) exhaled particle ratios, respectively. Similar to inhalation (R_1), instantaneous exhaled particle ratio (R_3) increased during early exhalation, followed by decrease until the end of exhalation phase (θ=360°) for all breathing conditions. At peak exhalation (θ=270°), R_3 was largest for SC, followed by TC, and essentially equal for NC, BC and HC. Comparing peak values of R_3, the following order was observed: $R_{3,TC} > R_{3,SC}$

$>R_{3,\mathrm{NC}} >R_{3,\mathrm{BC}} >R_{3,\mathrm{HC}}$.

Cumulative exhaled particle count at a given phase during exhalation was nondimensionalized by the prescribed outlet particle count to calculate cumulative exhaled particle ratio (R_4 in Figure 4.6D). All breathing conditions showed an identical trend, i.e., increase in total exhaled particle ratio from start to peak exhalation followed by essentially constant exhaled particle deposition until the end of exhalation. R_4 was largest in BC and smallest in TC during peak exhalation (θ=270°). At the end of exhalation, R_4 remained constant across all breathing conditions. With increasing breathing time (TC, NC, BC) for a constant peak exhalation flow rate, R_4 showed higher particle exhalation during the early exhalation phase ($\theta = 180°$) until peak exhalation ($\theta = 270°$) in BC and lower in TC. Since the minute ventilation for all conditions were equal, breathing with BC can increase particle exhaled ratio compared to other conditions and need to be investigated further.

With an increase in peak exhalation flow rate (SC, NC, HC), the particle exhalation ratio (R_4) was higher in NC during early exhalation ($\theta = 180°$) until peak exhalation ($\theta = 270°$) and lower in SC. Among SC, NC and HC, NC has better exhaled particle ratio compared to SC and has a lower minute volume than HC, exhaling at normal peak exhalation flow rate can increase the particle exhaled ratio and this need to be investigated further. It is important to note that particle deposition and particle exhaled ratios were calculated for airway geometry up to 2$^{\mathrm{nd}}$ generations. The effects of including higher generation airways will be needed to further characterize the particle exchange.

Previous studies showed increased deposition with an increase in particle size, for micro particles, and also increased deposition with a decrease in particle size, for nano particles (Tsuda et al., 2013). Smaller the nano particle, flow characteristics such as in bradypnea, can deposit higher percentages of particles during the early inhalation phase compare to other breathing patterns. Stronger jet streaming potential (as seen in hyperpnea) has higher inertial impaction on larger (macro) particles increasing potential for deposition near carnial ridges at the bifurcation. While the nano particles can be easily carried to higher

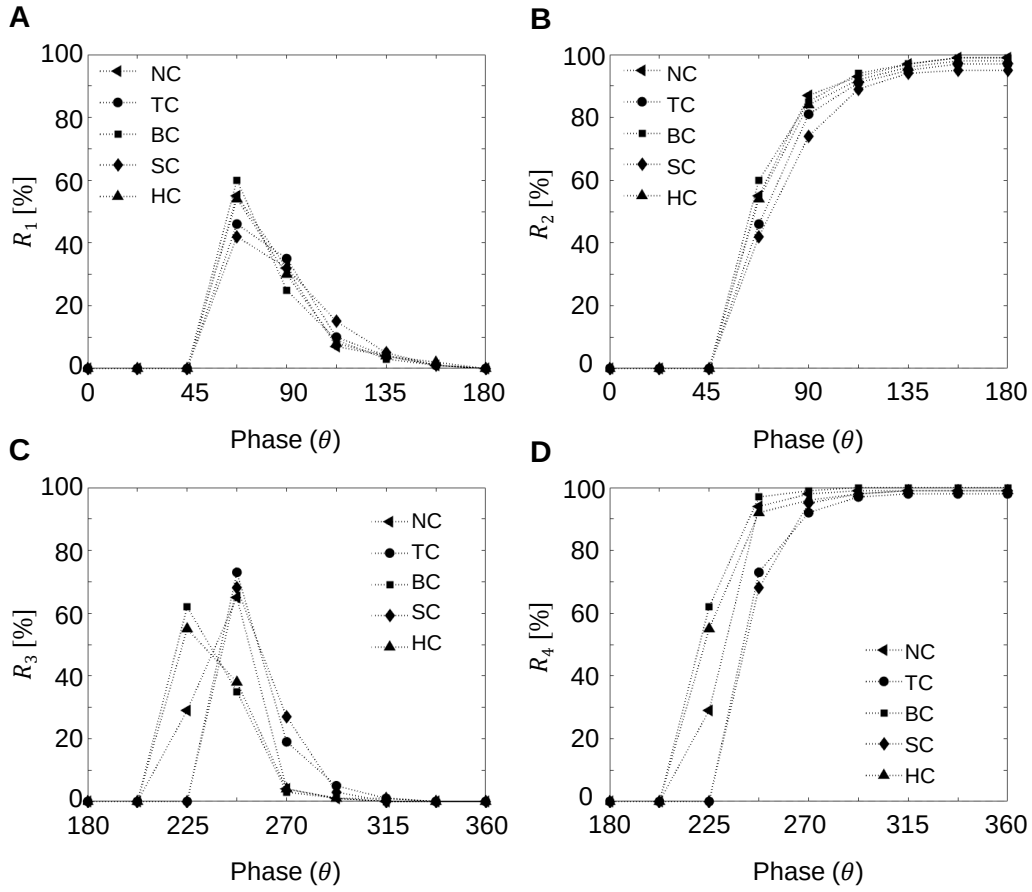

Figure 4.6: Transport characteristics of massless particles. (A) Instantaneous inhaled particle deposition (R_1). (B) Cumulative inhaled particle deposition (R_2). (C) Instantaneous exhaled particle ratio (R_3). (D) Cumulative exhaled particle ratio (R_4).

generations during hyperpnea breathing pattern.

Particles in the deposition study consists of massless properties with one–way coupled and resultant fate of particles was mainly due to the continuous flow. But the particles inhaled in realistic scenarios consists of wide range of diameters with varying densities and other chemical properties, effecting the drag force and consequently the deposition or exhalation fate. Current results can provide an estimate of gas–uptake/particle deposition behavior for various abnormal conditions. However, adding chemical and physical properties to existing models are needed for realistic estimation such as for gas exchange, target drug deposition, pollutants and other aerosol depositions.

4.5 Conclusions

Flow through an idealized, symmetric human airway model until 2^{nd} bifurcation was examined using CFD simulations to understand the effects of abnormal breathing patterns wherein either RR or airflow rate is altered from normal conditions.

Change in inhalation duration (tachypnea, normal and bradypnea) showed jet length in normal was greater than tachypnea and bradypnea conditions. In addition, time to peak jet length during inhalation increased with increase in breathing time. Cumulative inhaled particle deposition and exhaled particle ratio were lower in tachypnea and higher in normal condition at peak inhalation.

Changes in peak inhalation flow rate (hypopnea, normal and hyperpnea) at constant RR showed increased velocity magnitude with increase in peak inhalation flow rate for a given plane and phase. At peak inhalation, both jet length and jet streaming increased with an increase in peak inhalation flow. Cumulative inhaled particle deposition increased from hypopnea to normal condition with increasing peak inhalation flow rate throughout inhalation phase. For a constant RR (normal, hypopnea, hyperpnea) at peak exhalation phase, increasing peak exhalation flow rate showed increased cumulative exhaled particle ratio from hypopnea to normal, which was same as in hyperpnea.

4.6 Supplementary Material

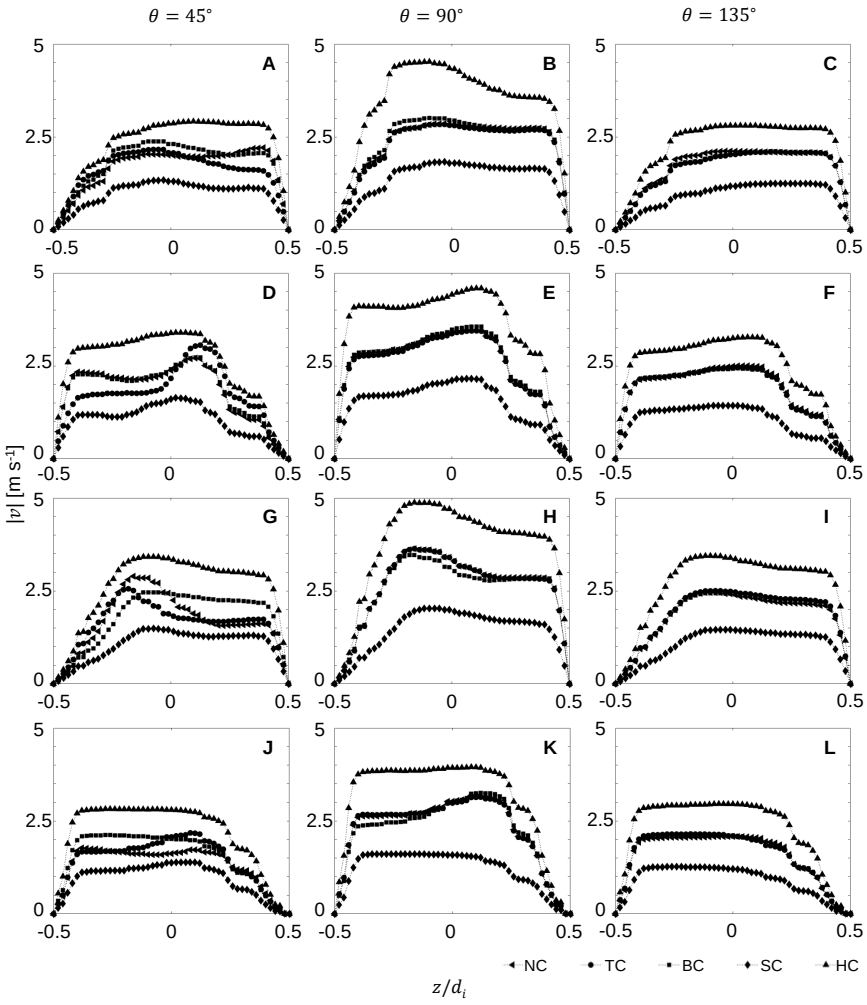

Figure SA2.1. Three-dimensional velocity magnitude ($|v|$) extracted along the coronal plane at (A)–(C) Plane 7 (first row), (D)–(F) Plane 8 (second row), (G)–(I) Plane 9 (third row) and (J)–(L) Plane 10 (last row) at early inhalation (θ=45° corresponding to 25% IT in (A), (D), (G), (J)), peak inhalation (θ=90^o corresponding to 50% IT in (B), (E), (H), (K)) and late inhalation (θ=180^o corresponding to 75% IT in (C), (F), (I), (L)). d_i indicates airway diameter a particular plane.

CHAPTER V

SA3: SINGLE vs. DOUBLE NOSTRIL INHALATION

5.1 Abstract

Previous spirometry studies showed an increase in lung efficiency for people undergoing yoga breathing techniques. Yoga breathing patterns consists of a long inhalation, breath hold and a long exhalation either through a single or double nostrils to ensure proper ventilation for higher airway generations. Fluid dynamics of yoga inhalation remains unknown. Using three dimensional computational fluid dynamics (CFD) simulations on idealized human airway model, we examine airway flow characteristics for single and double nostril breathing. Gas exchange in breathing technique was defined using ANSYS User Defined Scalar to estimate the oxygen deposition at higher airway. At peak inhalation, velocity contours at upper trachea showed anatomical right concentrated airflow during single nostril breathing, while centrally concentrated strong flow during double nostril breathing in idealized symmetric airway. Both single and double nostril breathing attained equal axial flow distribution from first generation (G1). Our results showed both single and double nostril inhalation in symmetric airway has equal gas exchange at higher airways, while the deposition increased in double nostril breathing method during breath hold. Steady simulations of single and double nostril inhalation on asymmetric airway model were conducted to see the flow distribution between G1. Steady simulations showed increased unequal flow distribution between G1 of asymmetric geometry compared to symmetric airway. Recommendations for futures studies were discussed.

5.2 Introduction

In the modern world, humans are victims of increased stress. Globally, about 265 million people suffer from stress, and anxiety symptoms which are leading causes of disability. About $ 1 trillion global economy loss was estimated by WHO for every year. Studies suggested yogic exercises can support to withstand such stress stimuli. Yoga is combination of both physical postures, breathing, and meditation (Barnes-Holmes et al., 2004). Yogic exercise such as *pranayama*, breathing exercise, is good to maintain proper health effecting the pulmonary function (Muktibodhananda, 2002; Taimni, 1961; Saoji et al., 2019).

Pranayama is combination of voluntarily controlled inhalation (*puraka*), breath hold (*anthar kumbhaka*) and exhalation (*rechaka*) (Reddy et al., 2015). Inhalation helps to stimulate the system, breath hold helps to distribute the air, and exhalation releases the vitiated air from the body (Sonne and Davis, 1982). Various number of *pranayama* techniques are known, such as *Surya bhedan* (continuous breathing with inhalation through left nostril, followed by exhalation through left nostril), *Nadi Shuddi* (alternate left nostril breathing cycle and right nostril breathing cycles), *Ujjayini* (inhalation through left nostril and followed by exhalation through right nostril in each cycle), and *Anulom vilam* (inhalation through left nostril, followed by exhalation through right nostril, inhalation through right nostril followed by exhalation through left nostril and so on). Effects of *pranayama* were investigated in large number of individuals (Reddy et al., 2015; Panwar et al., 2012); to compare effects between different yoga techniques of *suryanamakara* (body postures based exercise) and *pranayama* (Kondam et al., 2017, 2020), and slow over fast *pranayama* (Dinesh et al., 2015). Also, *pranayama* in chronic obstructive pulmonary disease (COPD) subjects (Meenakshi, 2017; Kaminsky et al., 2017) and young swimmers (Hakked et al., 2017) found a better lung functioning. All these studies investigated the effect of breathing techniques using spirometry while fluid dynamics inside airway was never investigated.

Unsteady oscillating breathing cycles were investigated in idealized airways, with and without oral cavities to investigate the flow regimes. Banko et al. (2015, 2016) conducted

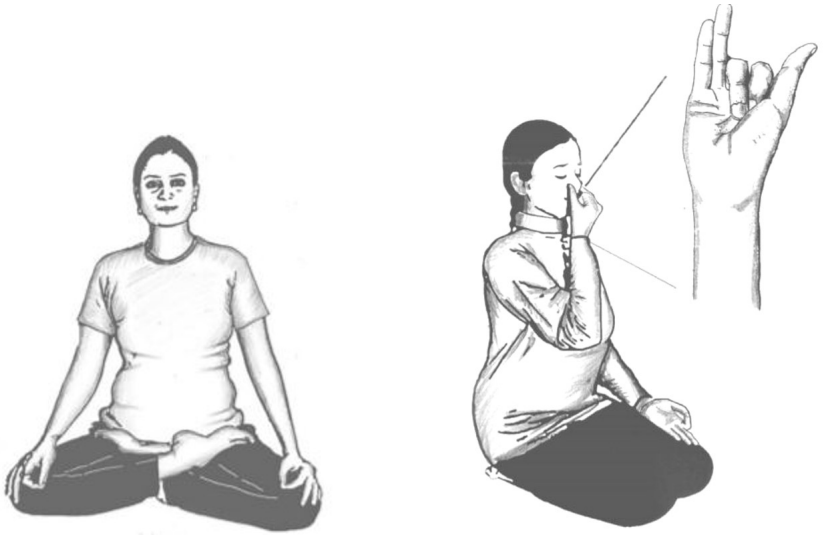

Figure 5.1: Representation of pranayama breathing postures and *nasika mudra* (hand posture) (Hakked et al., 2017).

experiments in subject specific airways, Gaddam and Santhanakrishnan (2021); Jalal et al. (2016, 2018, 2020) conducted CFD and experimental studies in idealized airways. In addition, all these studies showed the presence of stronger secondary flows, and it has a stronger mechanism for particle deposition. However all these studies did not include nasal cavity or mentioned for a need to include it, which would impact the flow inside trachea to higher generations. Liu et al. (2009) developed a standard nasal cavity based on inter subject variability, in addition to left to right asymmetry. Studies on flow through double nasal cavity showed nonuniform axial flow distribution along the length of nasal cavity Wen et al. (2008). Computational studies including steady flow, or unsteady flow through single nasal cavity during inhalation and breath hold were never studied.

Current study aims to characterize the effects of single vs double nostril breathing on gas exchange at higher generations using an oscillatory inhalation phase followed with a pause (no flow condition). Weibel's idealized airway model (trachea to 2^{nd} generation) with Liu et al. (2009) standardized nasal cavity was used for the current transient simulations. User defined scalar was used to estimate the gas deposition in higher generations in ANSYS Fluent 2020 R2. Finally, the effects of single over double nostril breathing and breath hold was discussed.

5.3 Methods

Idealized upper airway consisting of symmetric nostrils to pharynx was attached to idealized Weibel's idealized airway of trachea to 2nd Generation (G) with a glottis. An idealized nasal cavity geometry was reconstructed using standard nasal model from Liu et al. (2009), in Solidworks 2020. This geometry file was later converted to .IGS format and imported to ANSYS Fluent with meshing to generate multiple mesh files consisting of polyhedral cells and prism layers along the walls.

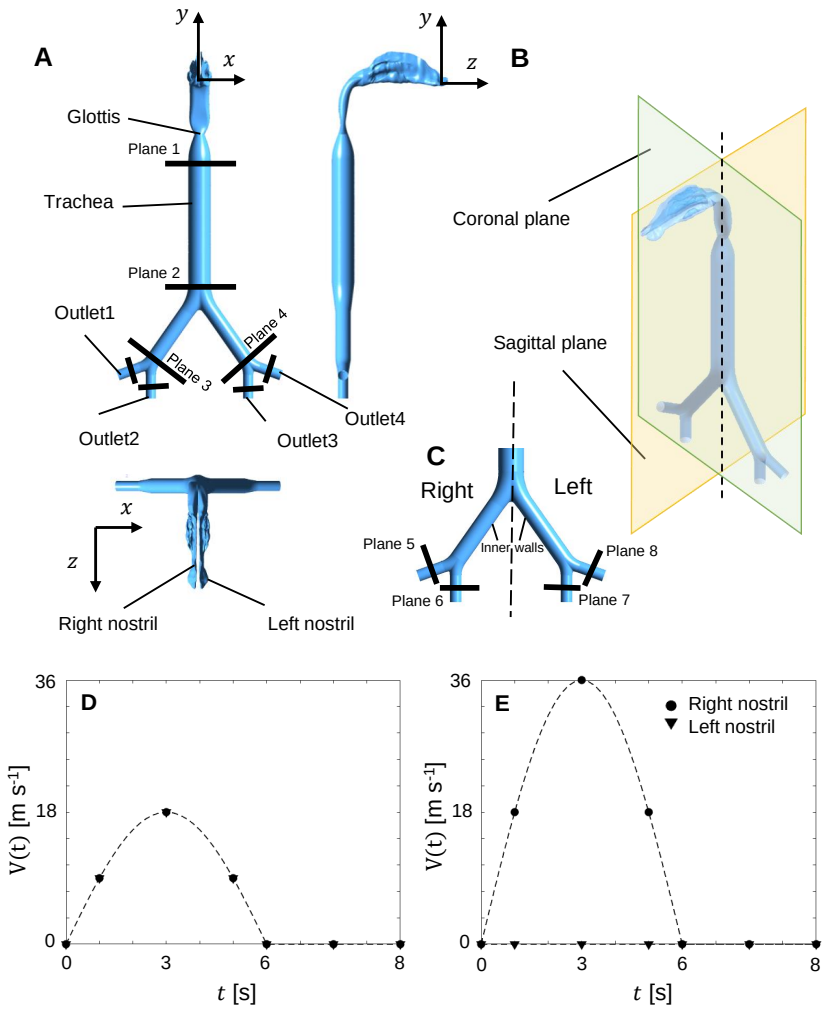

Figure 5.2: (A) Idealized airway geometry used for current test conditions in front view, side view and top view, with Planes 1-4 (B) Sagittal and coronal planes of airway geometry (C) Planes 5-8 in airway higher generations. Velocity profiles prescribed at left an right nostril during (D) double nostril inhalation and (E) single nostril inhalation. Refer Table 1 for geometric details of Planes 1-8.

Three-dimensional CFD simulations of transient, incompressible flow through the above airway geometry were performed in ANSYS Fluent. k-ω SST turbulence model, used in previous studies of flow through the human airway (Cui and Gutheil, 2017; Zhang and Kleinstreuer, 2011), was chosen for all simulations in this study. A normal breathing consists of flow through two nostrils (nostril inlet area A_N= 3.67 x 10^{-6} m^2) with tidal volume (TV) of 500 mL. For current test conditions inhalation time (IT)=6 s and breath hold time (BHT)= 2 s was maintained. Corresponding peak inhalation flow rate ($Q_{in,peak}$) when using oscillatory profile is calculated using

$$Q_{\text{in,peak}} = \left(\pi \frac{\text{TV}}{2.\text{IT}}\right) \tag{5.1}$$

Velocity profiles through both nostrils can be calculated using:

$$V_{\text{in,LR}}(t) = \frac{Q_{\text{in,peak}}}{2A_{\text{N}}} \sin\left(\frac{\pi t}{\text{IT}}\right),\ 0 < t \leq \text{IT} \tag{5.2}$$

$$V_{\text{in,LR}}(t) = 0,\ IT < t \leq \text{BHT} \tag{5.3}$$

where $V_{\text{in,LR}}$ is velocity through both left and right nostril, A_N is nostril area.

For velocity through single nostril, velocity profile for left nostril = 0 m s^{-1}, and velocity for right nostril ($V_{\text{in,R}}$) is calculated using:

$$V_{\text{in,R}}(t) = \frac{Q_{\text{in,peak}}}{A_{\text{N}}} \sin\left(\frac{\pi t}{\text{IT}}\right),\ 0 < t \leq \text{IT} \tag{5.4}$$

$$V_{\text{in,R}}(t) = 0,\ IT < t \leq \text{BHT} \tag{5.5}$$

Velocity profile (V(t)) corresponding to above equations is shown in Figure 3.1. Boundary conditions included zero pressures at the outlets and no-slip walls. To characterize the

oscillatory flow relative to viscous effects, Wo was calculated for each condition using

$$Wo = \frac{D}{2}\sqrt{\frac{\omega}{\nu}}, \tag{5.6}$$

where $\omega = 2\pi/\mathrm{BT}$ is the angular frequency based on breathing time (BT, where BT = 60/RR seconds), RR is respiratory rate =4.28 bpm (based on IT/BT = 1/2, with BHT= 2 s), D is the tracheal diameter, ν = 1.46 $\times$ 10^{-5} m^2 s^{-1} was used as the kinematic viscosity of air. For current test conditions Wo=1.58. In addition, the Reynolds number at the trachea during peak inhalation (Re) was defined as

$$Re = \left(\frac{V_\mathrm{T}\, D}{\nu}\right), \tag{5.7}$$

where V_T is the mean flow speed in the trachea, ν is the kinematic viscosity of air (1.46 $\times$ 10^{-5} m^2 s^{-1}), and D is the tracheal diameter = 18 mm and corresponding Re= 640 in trachea. Based on flow regime map, the current test conditions are in viscous region as shown in the Figure.

User defined scalar (UDS) was used to measure the oxygen deposition at higher generation with diffusivity = 2.3e-05 kg m^{-1} s^{-1} (diffusivity units are different than conventional definition, which is defined as density times diffusion coefficient). Air consisting of 30% of oxygen was inputted at inlet nostrils. The solution method includes a coupled scheme, second-order spatial discretization, and second-order upwind scheme for turbulence kinetic energy. A uniform time step δt = 0.2% of IT was used for running simulations for all breathing cycles. Mesh and time independence tests (similar to method prescribed in Gaddam and Santhanakrishnan (2021)) were performed on various meshes and final mesh consisting of 2.5 x 10^6 elements was finalized for all tests in this study. Three different time steps (0.001, 0.01, 0.1 s) were used in time independence tests of double nostril breathing, and final time step of 0.01 s was used for all studies due to lower computational costs and better accuracy. All simulations were auto-saved at inhalation phase (θ) = 60°. Solution

files were then exported and processed in CFD-Post (ANSYS 2020 R2) for analysis of axial flow and velocity profiles. For all the test conditions, velocity magnitude contours were exported and analyzed along various planes mentioned in Table 2 at various inhalation and exhalation phases. In addition, cumulative particle deposition at outlets for each breathing technique was nondimensionalized with inlet particle concentration to get particle deposition. Finally, effects of breathing pattern in given idealized symmetric airway were discussed.

5.4 Results

5.4.1 Axial Flow

Axial flow inside upper trachea (Plane 1) and lower trachea (Plane 2) is shown through contours of velocity magnitude with in-plane velocity vectors (refer Figure 5.3,5.4). For single nostril inhalation at Plane 1, the axial flow increased until peak inhalation and later decreased until late inhalation. Axial flow was concentrated on anatomical right side of the trachea during the early inhalation. In double nostril breathing, similar to single nostril breathing, axial flow increased from early inhalation until peak inhalation followed by decrease until end inhalation. But, the axial flow inside the double nostril breathing was concentrated along the sagittal plane during early inhalation unlike the single nostril breathing, which has axial flow concentrated on anatomical right side. After the peak inhalation axial flow was similar to that of single nostril breathing was observed i.e., strong axial flow concentrated towards the anatomical right side and decreased with inhalation phase.

At Plane 2, similar to Plane 1, axial flow increased until peak inhalation and later decreased until late inhalation in both single and double nostril breathing. In addition, the axial flow zones at each phase were similar in single and double nostril breathing showing no effect of type of breathing in current airway model (refer Figure 5.4).

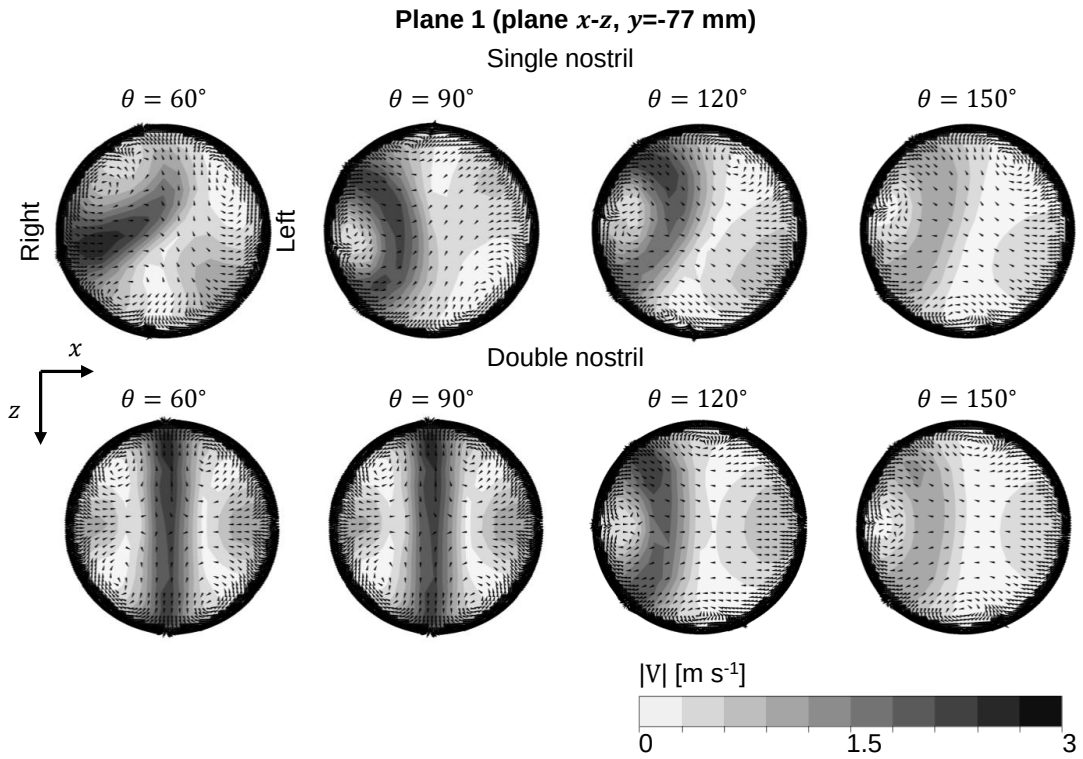

Figure 5.3: Velocity contours with in-plane velocity vectors at Plane 1 with varying inhalation phases (θ) for single nostril breathing (top) and double nostril breathing (bottom).

5.4.2 Velocity Profiles

Velocity profiles were extracted in the coronal plane for both single and double nostril breathing at peak inhalation phase ($\theta = 90°$) in Planes 1-8 and is shown in the Figure 5.5. At peak inhalation, both single and double nostril breathing has higher axial velocity at Plane 1 which later decrease at lower trachea (Plane 2). A small increase in peak axial velocity was observed at Planes 3-4 than Plane 2. In Planes 2-4, velocity distribution peaked at the center of the plane, while Planes 5-8 has skewed velocity distribution profiles. Planes 5,7 has a anatomical-left skewed profiles, and Planes 6,8 has anatomical-right skewed profiles such that flow through 2nd bifurcations have flow skewed towards the inner walls of airway.

Comparing between single and double nostril breathing, the flow at upper plane during single nostril breathing has lower velocity on anatomical left side. Also at Plane 2, single nostril breathing has more uniform flow compared to double nostril breathing. For current

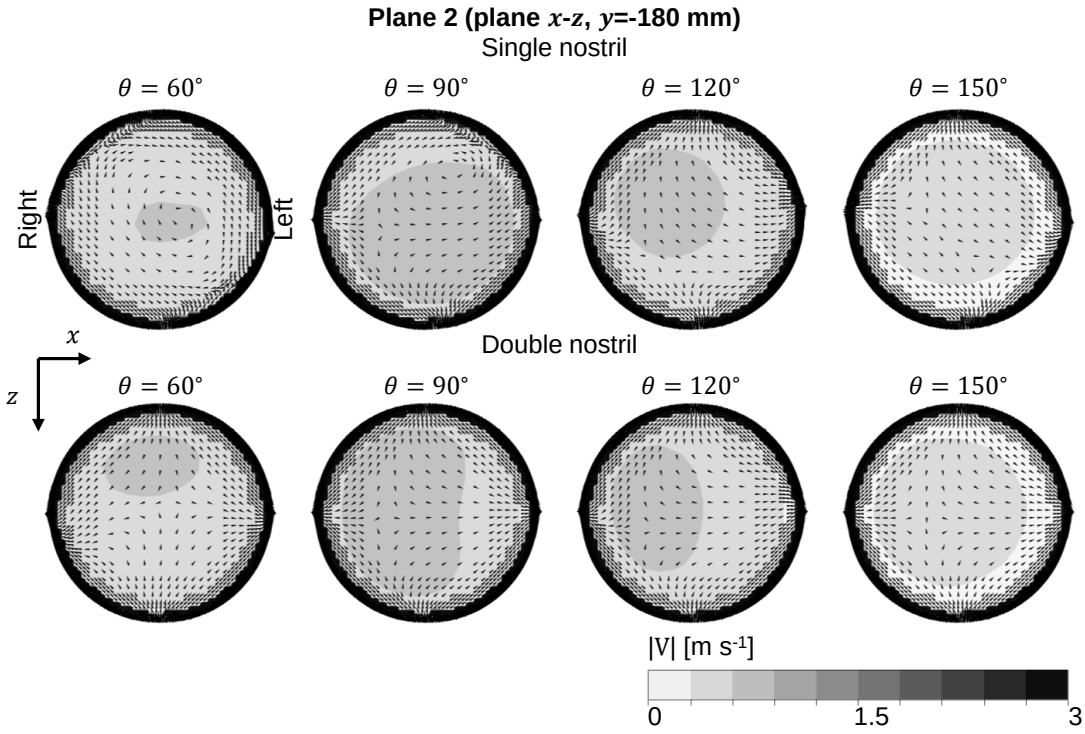

Figure 5.4: Velocity contours with in-plane velocity vectors at Plane 2 with varying inhalation phases (θ) for single nostril breathing (top) and double nostril breathing (bottom).

test conditions, both single and double nostril breathing has effected the upper tracheal flow and remained same in higher generations (G1 and G2).

Velocity profiles extracted along coronal plane at late inhalation phase (θ=150°), for Planes 1-8 is shown in the Figure 5.6. During late inhalation at Plane 1, velocity distribution at anatomical right was higher in single nostril breathing than in double nostril breathing. While for Planes 2-8, velocity profiles for single and double nostril breathing were equal in a given plane. In Plane 2, a nearly uniform velocity profile was observed, which later converted to centrally skewed velocity profile in G1 (Planes 3, 4). Velocity profile in G2 was skewed towards the inner walls of bifurcation such that Planes 5, 7 were anatomical left skewed and Planes 6, 8 were anatomical right skewed. Velocity magnitude decreased in each plane compared to peak inhalation phase, respectively for single and double nostril breathing. In addition, single and double nostril breathing in symmetric airway did not effect late inhalation in higher airway generations.

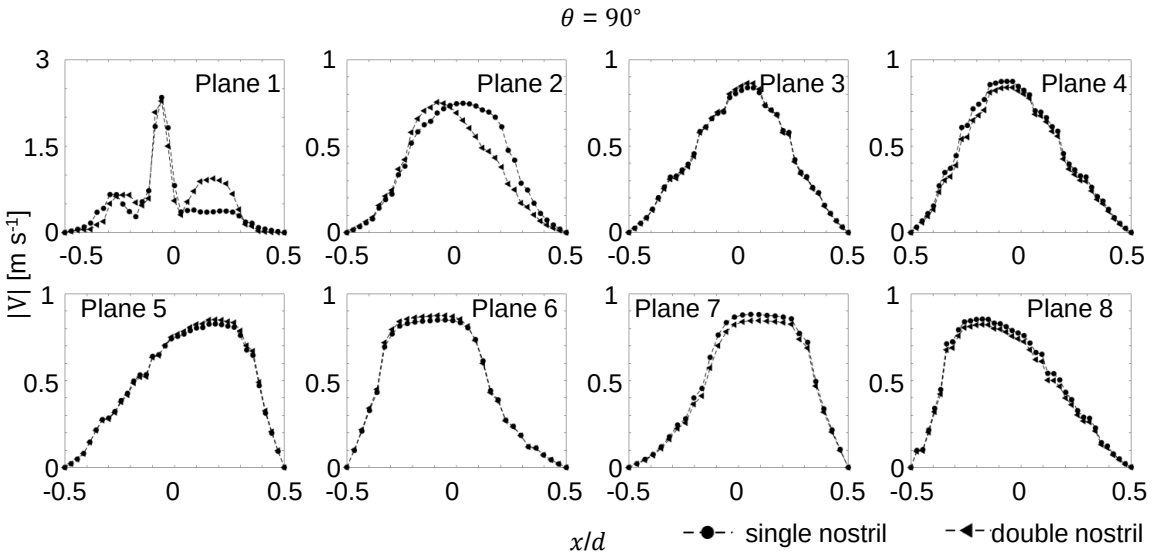

Figure 5.5: Three-dimensional velocity magnitude (|V|) extracted along coronal plane at Planes 1-8 for single (–●–) and double (–◄–) nostril breathing at peak inhalation phase (θ)=90°.

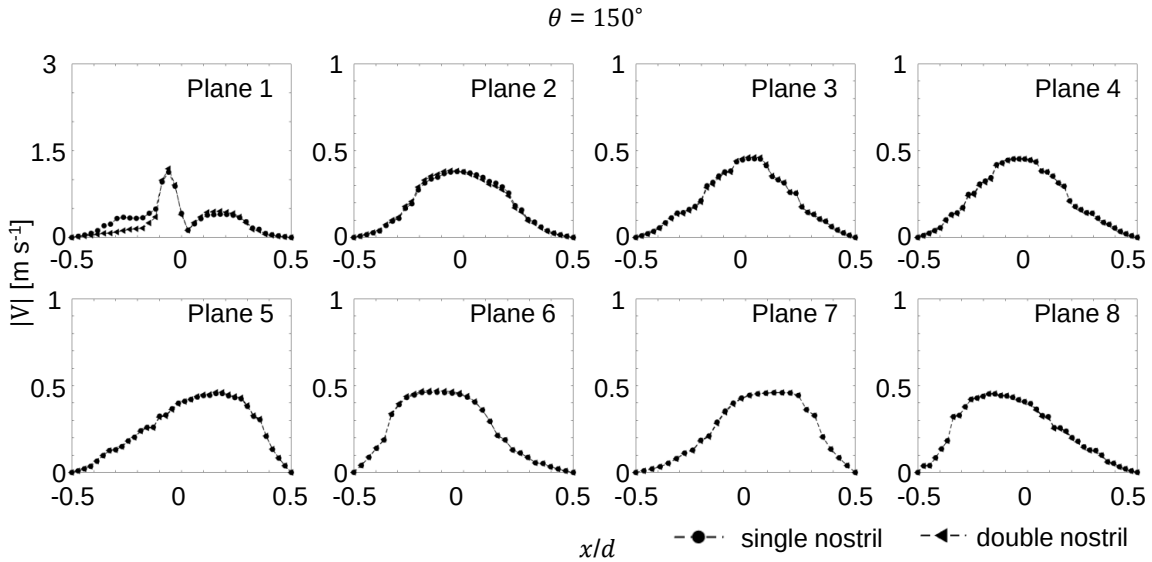

Figure 5.6: Three-dimensional velocity magnitude (|V|) extracted along coronal plane at Planes 1-8 for single (–●–) and double (–◄–) nostril breathing at late inhalation phase (θ)=150°.

5.4.3 Particle Deposition

Particle deposition ratio of user defined scalar was calculated for all outlets during single and double nostril breathing. Particle deposition increased with increase in inhalation phase for both single and double nostril breathing. In addition, particle deposition at higher generations was same in single and double nostril breathing techniques during inhalation. While during the late inhalation and breath hold, the particle deposition in single nostril breathing was slightly lower than double nostril breathing (refer Figure 5.7). The breathing pattern did not effect the particle deposition inside symmetric airways.

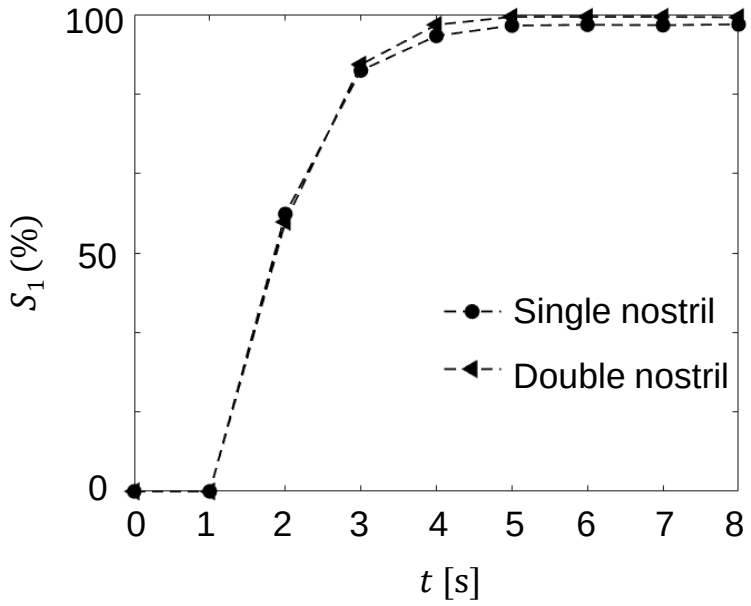

Figure 5.7: Particle deposition in single (–●–) and double (–◄–) nostril breathing during inhalation.

5.5 Discussion

5.5.1 Implications on Yoga Breathing

Although, axial flow was influenced in the upper trachea due to type of breathing pattern, both single and double nostril has equal axial flow from lower trachea to higher generations.

This observations were mainly done based on equal flow rates at peak inhalation in trachea with a normal tidal volume. But conditions has in yoga breathing involves slow breathing at higher tidal volume compare to normal breathing which would proportionately effect the axial flow inside trachea and higher generations.

Most yoga breathing patterns include a single nostril breathing, followed with head rotation. Our previous studies on rotated head showed biased airflow towards right side compared to left side of symmetry generations. Including such head rotation for current simulations need to be investigated. Future scope on a parametric study for yoga simulations must include varying inhalation duration, breath hold time, asymmetric geometry, exhalation time, head rotation, subject specific geometries, and finally varying breathing patterns with alternate nostrils to characterize the particle deposition at higher generations.

Current study showed no effect of single over double nostril breathing in higher generations in symmetric airway, showing no importance of such breathing technique. The possible reason could be idealization of airway and maintaining symmetry in higher generations. To validate an asymmetry in higher generation was developed and investigated under steady state three-dimensional computational fluid dynamic simulations.

5.5.2 Asymmetric Geometry

An asymmetric airway geometry was designed to test the effect of single nostril breathing. This geometry consists of asymmetry in the Generation 1. The asymmetric airway was designed with details of diameters and length from symmetric geometry, with additional details of angle between G0 and anatomical left G1 at $\beta = 120^{\circ}$ (angle was observed in subject specific airway of Banko et al. (2015)). Steady simulations with simulations method prescribed for transient setup were used to obtain three conditions, namely (A) breathing through both left and right nostrils (*LR*), (B) breathing through left nostril (*L*), and (C) breathing through right nostril (*R*). Asymmetric and symmetric geometry were tested for tidal volumes (TV)=500 mL and 600 mL. During condition *LR*, velocities for both left

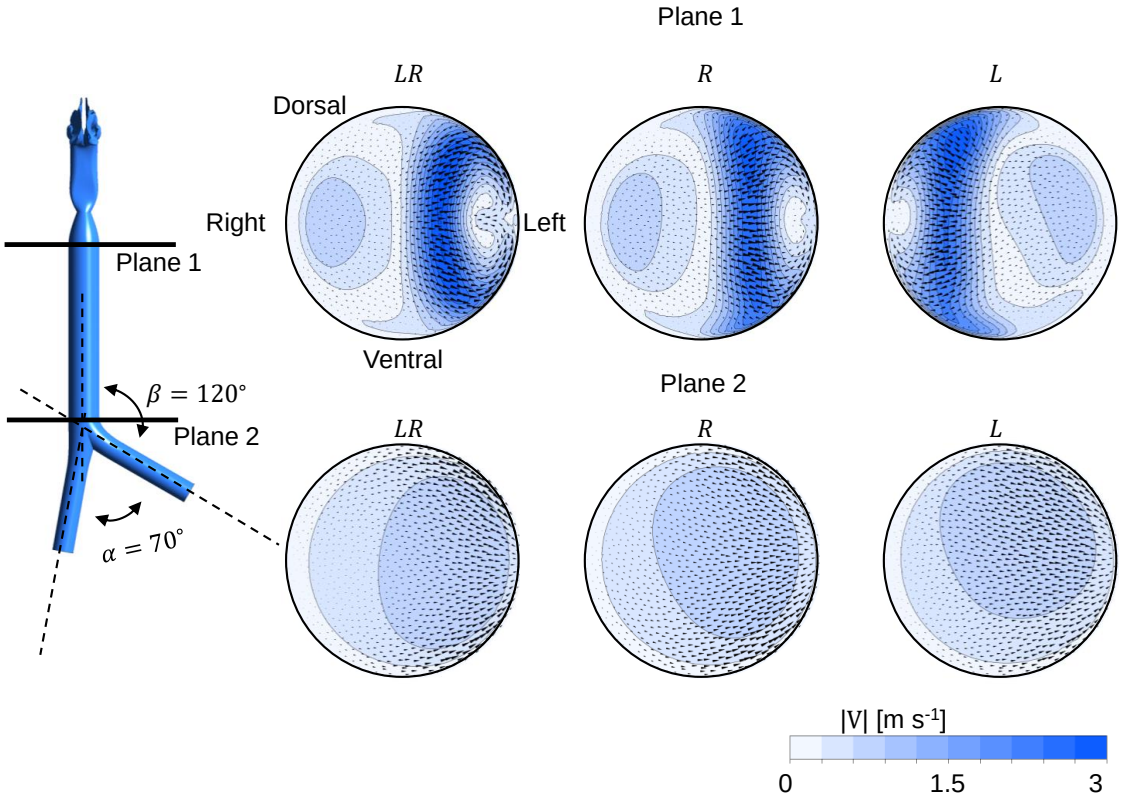

Figure 5.8: Velocity magnitude contours with in-plane velocity vectors at Planes 1 and 2 for conditions *LR*, *R*, and *L* of steady state simulations. Inset shows the asymmetric airway with geometrical plane locations with β=angle between trachea and left generation (G1), and α=bifurcation angle.

and right nostril V=17.834 m s $^{-1}$ (corresponding TV=500 mL), and V=21.4 m s $^{-1}$ (corresponding TV=600 mL). During condition *R*, velocities for left nostril V=0 m s $^{-1}$ and right nostril V=35.667 m s $^{-1}$ (corresponding TV=500 mL), and V=42.8 m s $^{-1}$ (corresponding TV=600 mL). During condition *L*, velocities for left nostril V=35.667 m s $^{-1}$ (corresponding TV=500 mL), and V=42.8 m s $^{-1}$ (corresponding TV=600 mL); and for right nostril V=0 m s $^{-1}$. Velocity magnitude contours at Planes 1,2 are shown in Figure 5.8 for TV=500 mL and nondimensional flow rate (ratio of flow rate at each outlet (left G1 and right G1) divided with flow rate in trachea at Plane 2) was measured for each condition (refer Table 5.1) at TV=500 mL and 600 mL.

Velocity magnitude contours at Plane 1 showed a peak magnitude zone on anatomical

Table 5.1: Steady flow distribution between left and right generation (G1) from trachea (G0) in symmetric and asymmetric airway model. Nondimensional flow rates (Q_r/Q_o, defined as ratio of flow through right G1 to flow through trachea (G0)) and Q_l/Q_o, defined as ratio of flow through left G1 to flow through trachea (G0)) were shown in table. Q_r=flow rate through the right G1, Q_l= flow rate through the left G1, and Q_o=flow rate through the trachea.

Condition	Geometry					
	Symmetric (TV=500 mL)		Asymmetric (TV=500 mL)		Asymmetric (TV=600 mL)	
	Q_r/Q_o	Q_l/Q_o	Q_r/Q_o	Q_l/Q_o	Q_r/Q_o	Q_l/Q_o
LR	48.5	51.5	50.2	49.8	55.99	44.01
R	50.1	49.9	51.8	48.2	51.98	48.02
L	49.9	50.1	52.3	47.7	52.57	47.43

left side for *LR* and *R* condition, and anatomical right side for *L* condition. At plane 2, the peak magnitude zone was on anatomical left side for all conditions (*LR*, *R* and *L*). Comparing these velocity magnitudes to peak inhalation in symmetric airway (refer $t = 3$ s at Plane 1), the peak velocity magnitude zone was concentrated mostly on the anatomical left. In addition, symmetric geometry has nearly equal flow distribution in *R* and *L* conditions, while the asymmetric geometry showed a large variations in the flow distribution. Also, all test conditions (*LR*, *R*, and *L*) showed increased flow rates from symmetric geometry to asymmetric geometry test conditions for TV=500 mL. Preliminary steady flow analysis on higher generation symmetry over asymmetry, showed effects of single over double nostril breathing, which need to be investigated further during unsteady breathing patterns. While with increase in TV, during *LR* along with unequal flow distribution between left to right generation (also seen in TV=500 mL), the right distribution has higher flow distribution compared to right distribution of TV=500 mL. While nearly equal distribution was seen for left and right generations during single nostril breathing at TV=500 mL and 600 mL.

5.6 Conclusions

Idealized airway model consisting of nasal cavity, pharynx, glottis, trachea to higher generations until 2nd bifurcation was tested with simple oscillatory inhalation profiles through single and double nostrils followed by breath hold. Velocity contours showed strong axial

flow region towards the anatomical right side of upper trachea during single nostril breathing, while centrally concentrated axial flow during the double nostril breathing. Velocity profiles showed decrease in strength of axial flow from upper trachea to the lower trachea in both single and double nostril breathing. In addition, for the given symmetric geometry the breathing patterns did not has effect on flow through higher airways. Increased particle deposition from single nostril breathing due to double nostril breathing techniques during breath hold for given airway geometry. Early studies with idealized asymmetric airway showed unequal flow distribution from trachea to left and right generations which need to be investigated further with unsteady breathing patterns for implications of yoga breathing patterns.

CHAPTER VI

SUMMARY

6.1 Discussion

Airflow through human airways is characterized by unsteady flows, with flow separations at airway bifurcations. The oscillatory nature of airflow, unequal durations of inhalation time (IT), and exhalation time (ET) can facilitate gas exchange in higher generations of the human airway. Normal respiratory rate (RR) in adults ranges between 10-15 breaths per minute (bpm). RR varies in exercise conditions, mechanical ventilation strategies such as high-frequency oscillatory ventilation (HFOV), metabolic activities and pathological state to facilitate alveolar gas exchange. Previous studies characterized flows at steady inhalation and exhalation through airways. The effects of varying inhalation duration and breathing flow rate on flow through airways remains unknown. Our study focuses on various unsteady breathing patterns inside idealized airway models. The goal of this study is to characterize the effects of unsteady internal airflow through idealized airway geometries. Various scenarios of unsteady breathing patterns were simulated in ANSYS 2020 R2 to characterize the fluid dynamics involved in such an unsteady airflow mechanism. The first study includes unsteady breathing patterns such as normal, moderate, and high-frequency ventilation were investigated with variation in inhalation time (IT) to breathing time (BT) ratio. The second study includes abnormal breathing patterns such as tachypnea ($\approx$ 1.5x increase in RR), bradypnea ($\approx$ 1.5x decrease in RR), hyperpnea (deep breathing with abnormally large peak flow rate), and hypopnea (shallow breathing with abnormally low peak flow rate); and final study includes alternate breathing patterns as in yoga pranayama breathing techniques. Simulations were performed for each breathing pattern as in internal airflow studies.

Jan et al. (1989) developed a diagram to classify the flow regime within different human airway sections, using an order of magnitude analysis starting from the Navier–Stokes' equations. This diagram was used to characterize the influence of fluid viscosity, unsteadiness, and convective acceleration in an idealized airway bifurcation for Wo ranging from 2.3 to 21.3. Their flow map examined Wo^2 versus non-dimensional stroke length $2L/D$, where L is the stroke length (i.e., the axial length of travel of a fluid particle) that can be calculated as the ratio of stroke volume (SV) swept in a cycle to the tracheal cross-sectional area) and D is the tracheal diameter. For a sinusoidal waveform (as considered in this study), Jan et al. (1989) showed that Re is related to dimensionless stroke length ($2L/D$) and Wo as $Re/Wo^2 = 2L/D$. However, their classification was restricted to oscillatory (sinusoidal) breathing cycle with IT/BT = 50%. Table 3.3 shows the SV, L, $2L/D$ evaluated for this study at the upper tracheal cross-section (Plane 1) across the various conditions of Wo and IT/BT, where Re = 4200, based on U_{T} and D. It can be seen that Re/Wo^2 does not equal $2L/D$ when IT/BT $\neq$ 50%.

To include the effect of IT/BT $\neq$ 50%, we examined the use of a modified dimensionless stroke length, where the parameter (BT/2 IT) is included as a multiple of $2L/D$ (i.e., $(2L/D)$(BT/2 IT)). The modified dimensionless stroke length matched Re/Wo^2 for all Wo and IT/BT conditions considered in this study. The flow map for all categories in the current study was shown in Figure 6.1.

Conditions such as in moderate and HFOV breathing were mainly dominated by unsteady and convective forces over the viscous forces. Breathing conditions such as normal, bradypnea, tachypnea hypopnea and hyperpnea were dominated by viscous convective forces over the unsteady forces. Yoga breathing pattern as more viscous dominated over unsteady forces inside the trachea. Changing the peak inhalation and decreasing the Wo would make more viscous domination, which can be seen in yoga breathing techniques. All these conditions were characterized for peak inhalation.

Axial flow inside trachea in all conditions during oscillatory inhalation increased from

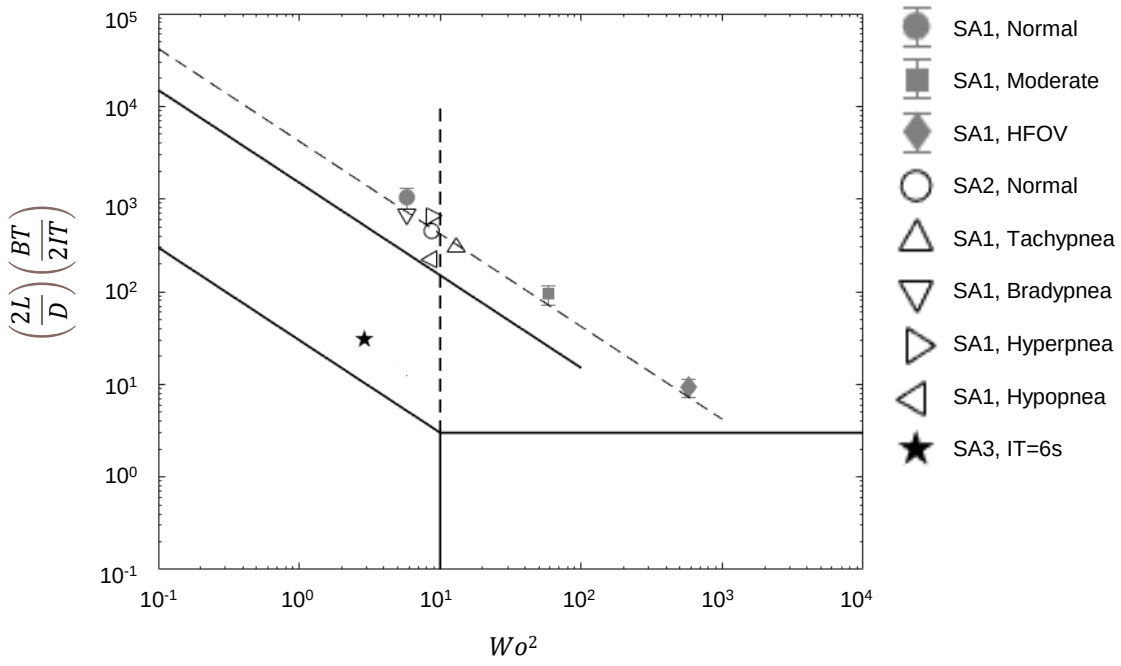

Figure 6.1: Airflow regime with current study conditions for normal (circle), moderate (square), HFOV (diamond), tachypnea (triangle), bradypnea (downward-pointing triangle), hyperpnea (right-pointing triangle), hypopnea (left-pointing triangle) and single nostril (five-pointed star) breathing conditions.

early inhalation until peak inhalation and later decreased until late inhalation. Similar to inhalation, axial flow during exhalation increased in strength from early exhalation until peak exhalation and later decreased until end exhalation. In addition, axial flow was higher in the upper trachea, and the flow became more uniform in the higher generations. In addition, with increase in *Wo*, the jet streaming decreased and axial flow in the higher generations was more uniform. Axial flow inside airways of head inside coronal plane showed a unequal axial flow distribution in higher airway generations. Also situation of abnormal and yoga breathing must to be investigated further with head rotation as our initial study from (SA1) showed unequal axial flow distribution.

6.2 Clinical Significance

Secondary flows are generated inside airways due to abrupt geometrical changes, and uneven contraction and expansions in airway. Secondary flow inside the idealized airways was found higher compared to the axial flow for normal, moderate and high frequency oscillatory ventilation. These secondary flow was expected to impact particle deposition in applications of targeted drug delivery. Chemical properties of aerosols or drug, provides early estimate of deposition mechanism such has due to inertial impaction, gravity or suspension based deposition. But, the secondary flow transport mechanism potentially affect the particle deposition due to higher strength than axial flow and promotes to upper airway deposition compared to lower airway.

6.3 Prospective Studies

Current study results were mainly based on simulations and need to be validated with experiments. In addition, all these simulations has computational costs and time for running each simulation was huge. A respiratory syringe pump can be used to investigate the flows for various breathing conditions as shown in the Figure 6.2. Here are the suggestions for future studies for each specific aim.

6.3.1 Specific Aim 1: Effects of Varying Inhalation Duration and Respiratory Rate on Human Airway Flow.

The study was investigated with constant *Re* =4200, across various breathing frequencies (*Wo*=2.41,7.61, and 24.1) for varying inhalation to breathing time. Additional studies conducting a sweep of *Re* would better characterize the flow inside various age groups or people with different trachea diameter. Previous studies showed a *Re*=500-1000 can be expected in children. Conducting more simulations for various *Re* number would be more helpful to characterize the air flow across age groups and airway geometries.

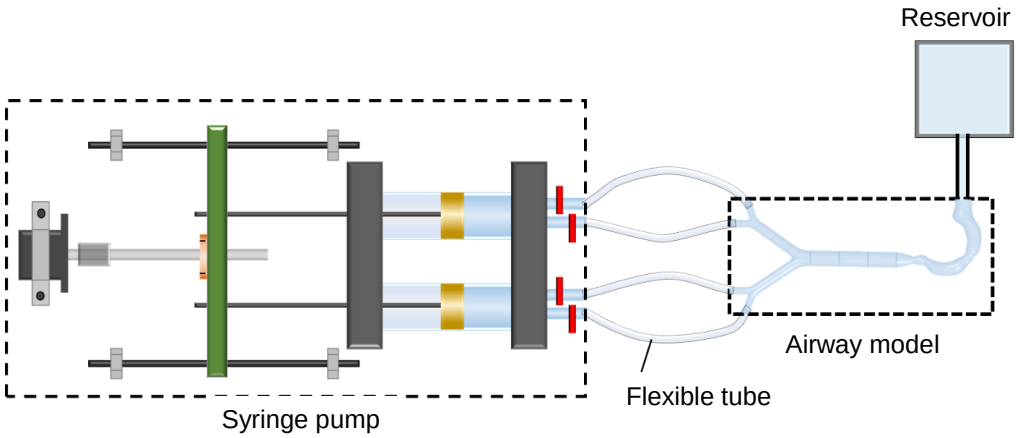

Figure 6.2: Schematic showing a syringe pump for experimental oscillatory flow studies.

6.3.2 Specific Aim 2: Fluid Dynamics of Abnormal Breathing Patterns

This study used a normal breathing parameters and compared against varying breathing parameters to characterize the effect of abnormal breathing patterns in idealized airways. Since the study was conducted for varying breathing parameters, the only limitation includes lack of using subject specific airways, which could help to characterize subject level treatment for estimating the acid-base disorders. Also, studies such as user defined scalar could potential address the gas exchange at higher generations at each abnormal condition.

6.3.3 Specific Aim 3: Single vs. Double Nostril Breathing with a Breath Hold

Current study aims to investigate the effect of single nostril breathing against double nostril breathing for a peak inhalation flow rate corresponding to normal tidal volume. This study mainly included idealized symmetric geometry, with a 6 s of inhalation duration and 2 s of breath hold duration. This study can be extended further such as:

- varying peak inhalation flow rates.
- including exhalation condition with varying peak exhalation flow rates and exhalation durations.

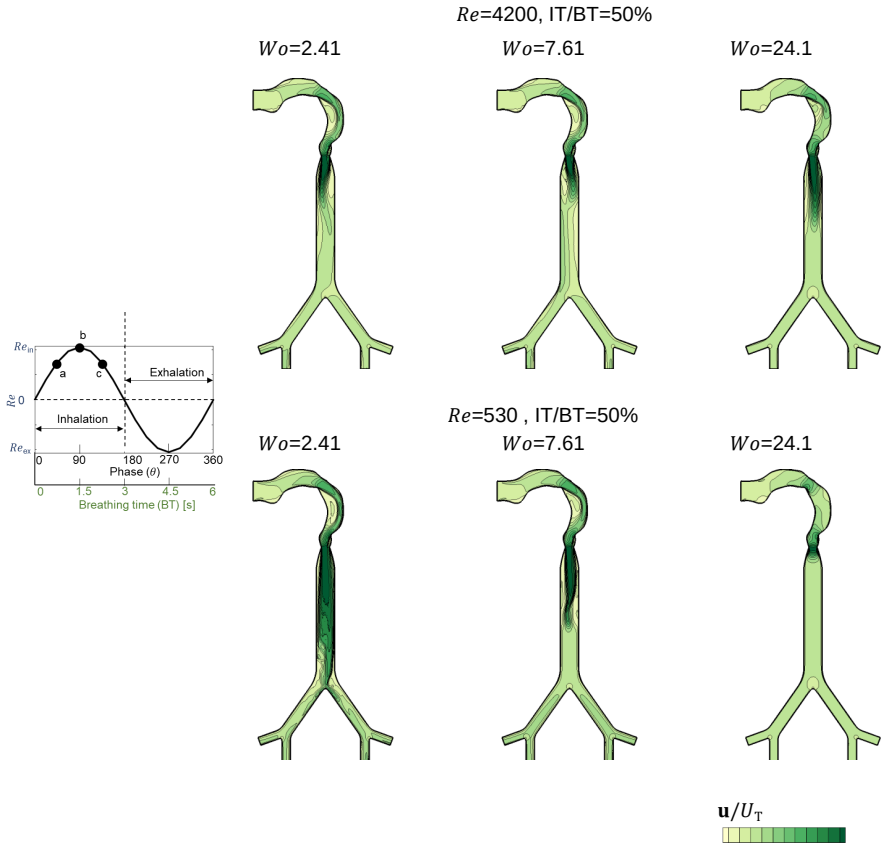

Figure 6.3: Three dimensional velocity contours (non-dimensionalized with mean flow speed in trachea, U_{T}) at peak inhalation for Wo = 2.41-24.1 at IT/BT = 50% for Re=4200 and 500. Inset shows the variation of Re inside trachea for a breathing cycle at peak inhalation Reynolds number (Re_{in}) and peak exhalation Reynolds number (Re_{ex}). For top row, Re_{in}=Re_{ex}=4200, and for bottom row Re_{in}=Re_{ex}=530.

- conducting simulations on various geometries (subject specific, idealized asymmetric).

- various breathing patterns of yoga conditions (include alternate nasal breathing).

- upper airway rotation

Varying these breathing conditions would definitely quantify the effects of breathing techniques for a subject based treatments.

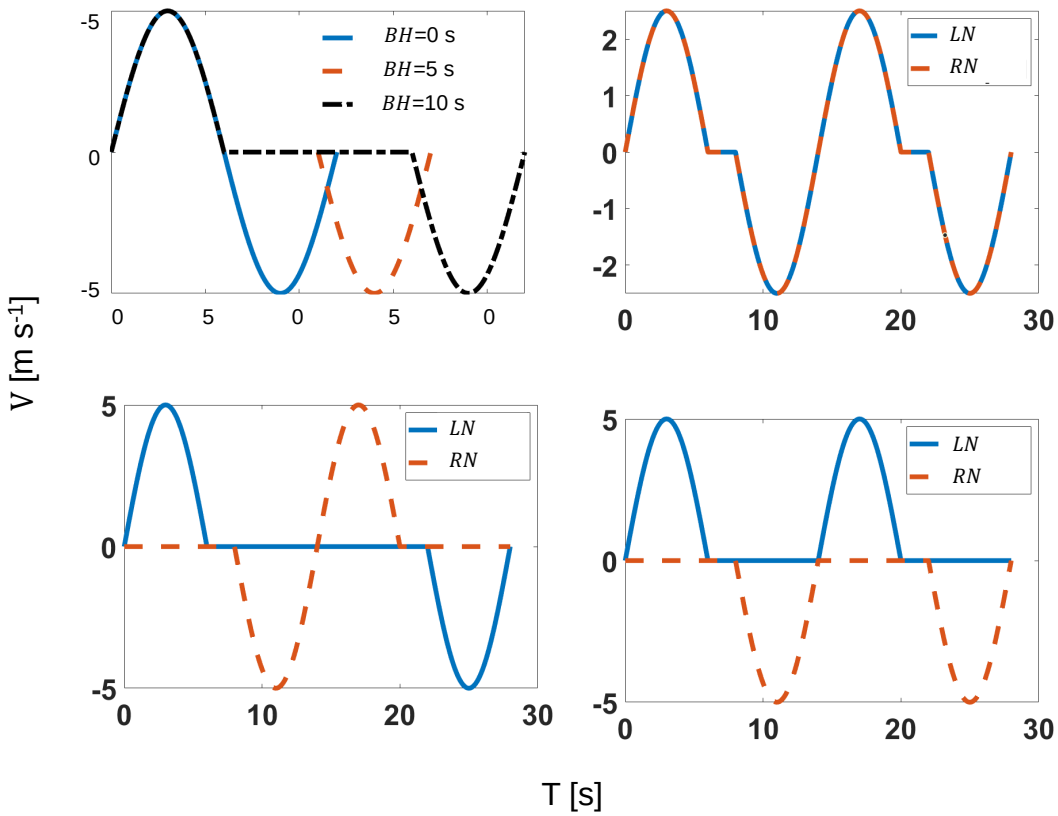

Figure 6.4: Velocity profiles for varying (A) breath hold durations and (B-D) yoga breathing patterns. *BH*=breath hold, *LN*=left nostril and *RN*=right nostril.

6.4 Limitations

A central limitation of our studies is the simplification of our model geometries. A range of morphological complexities observed from G0-G2, including (but not limited to) asymmetric branching and non-circular lumen of the airway branches, are expected to alter the respiratory flows. Additional model simplifications, such as the use of rigid walled vessels and a sinusoidal flow profile, should also be noted as limitations of this study. While changes to waveform shapes have shown to modestly impact the flow physics (Choi et al., 2010), including airway wall motion has been reported to influence axial and secondary flows compared to rigid-walled airways (Wall and Rabczuk, 2008). Finally, RANS models (such as in this study) have well-known limitations in modeling unsteady turbulent flows, and comparisons of our study findings with higher-fidelity turbulence models (e.g., large

eddy simulations) are needed to examine how the choice of turbulence model impacts time-varying flow physics.

In specific aim 1, the general trends reported here relative to *Wo* and IT/BT, specifically the importance of secondary flows with increasing *Wo* as well as the modified dimensionless stroke length accounting for IT/BT, are expected to be applicable in anatomically realistic airways. In specific aim 2, implications on gas exchange need to be investigated with varying parameters. Finally in specific aim 3, mainly parametric studies consisting of inhalation flow rates, exhalation flow rates, realistic and idealized airway models, breath hold time, and yoga breathing patterns can estimate the airflow nature inside airways for subject specific treatment.

6.5 Conclusion

In all the breathing conditions, axial flow increased in strength from early inhalation until peak inhalation and later decreased until late inhalation. Similarly, during the oscillatory exhalation conditions axial flow increased in strength from early exhalation to peak exhalation and later decreased in strength until late exhalation. In addition, axial flow in inhalation decreased in strength from upper trachea to lower trachea in all breathing conditions. Secondary flow was found higher in strength compared to axial flow across varying breathing frequencies. Change in breathing frequency, peak inhalation flow rates at inhalation and exhalation affected the jet streaming and axial flow strength inside airways, which indeed affect the gas exchange. Studies from single to double nostril breathing effected the axial flow inside the upper airways. Future studies consisting of yoga breathing parameters were suggested for characterizing the effect of yoga breathing inside airways.

References

Adler, K. and Brücker, C. (2007), 'Dynamic flow in a realistic model of the upper human lung airways', *Experiments in Fluids* **43**(2-3), 411.

Ahmed, S. M. and Athar, M. (2015), 'Mechanical ventilation in patients with chronic obstructive pulmonary disease and bronchial asthma', *Indian Journal of Anaesthesia* **59**(9), 589.

Augusto, L., Lopes, G. and Goncalves, J. (2016), 'A cfd study of deposition of pharmaceutical aerosols under different respiratory conditions', *Brazilian Journal of Chemical Engineering* **33**(3), 549–558.

Balásházy, I. and Hofmann, W. (1995), 'Deposition of aerosols in asymmetric airway bifurcations', *Journal of Aerosol Science* **26**(2), 273–292.

Banko, A. J., Coletti, F., Elkins, C. J. and Eaton, J. K. (2016), 'Oscillatory flow in the human airways from the mouth through several bronchial generations', *International Journal of Heat and Fluid Flow* **61**, 45–57.

Banko, A. J., Coletti, F., Schiavazzi, D., Elkins, C. J. and Eaton, J. K. (2015), 'Three-dimensional inspiratory flow in the upper and central human airways', *Experiments in Fluids* **56**(6), 117.

Barnes-Holmes, Y., McHugh, L. and Barnes-Holmes, D. (2004), 'Perspective-taking and theory of mind: A relational frame account.', *The Behavior Analyst Today* **5**(1), 15.

Belka, M., Lizal, F., Jedelsky, J., Elcner, J., Hopke, P. K. and Jicha, M. (2018), 'Deposition of glass fibers in a physically realistic replica of the human respiratory tract', *Journal of Aerosol Science* **117**, 149–163.

Benavides-Pinzón, W. F. and Torres, J. L. (2017), 'Effects of yoga (pranayama) on lung function and lactate kinetics in sedentary adults at intermediate altitude', *Revista de la Facultad de Medicina* **65**(3), 467–472.

Borojeni, A. A., Garcia, G. J., Moghaddam, M. G., Frank-Ito, D. O., Kimbell, J. S., Laud, P. W., Koenig, L. J. and Rhee, J. S. (2020), 'Normative ranges of nasal airflow variables in healthy adults', *International Journal of Computer Assisted Radiology and Surgery* **15**(1), 87–98.

Boros, S. J., Matalon, S. V., Ewald, R., Leonard, A. S. and Hunt, C. E. (1977), 'The effect of independent variations in inspiratory-expiratory ratio and end expiratory pressure during mechanical ventilation in hyaline membrane disease: the significance of mean airway pressure', *The Journal of Pediatrics* **91**(5), 794–798.

Boulding, R., Stacey, R., Niven, R. and Fowler, S. J. (2016), 'Dysfunctional breathing: a review of the literature and proposal for classification', *European Respiratory Review* **25**(141), 287–294.

Calay, R., Kurujareon, J. and Holdø, A. E. (2002), 'Numerical simulation of respiratory flow patterns within human lung', *Respiratory Physiology & Neurobiology* **130**(2), 201–221.

Chen, Z., Parameswaran, S., Hu, Y., He, Z., Raj, R. and Parameswaran, S. (2014), 'Numerical simulations of high-frequency respiratory flows in 2d and 3d lung bifurcation models', *International Journal for Computational Methods in Engineering Science and Mechanics* **15**(4), 337–344.

Cheng, Y.-S., Zhou, Y. and Chen, B. T. (1999), 'Particle deposition in a cast of human oral airways', *Aerosol Science & Technology* **31**(4), 286–300.

Cherniack, N. S. and Fishman, A. P. (1975), 'Abnormal breathing patterns', *Disease-a-Month* **21**(7), 1–45.

Choi, J., Tawhai, M. H., Hoffman, E. A. and Lin, C.-L. (2009), 'On intra-and intersubject variabilities of airflow in the human lungs', *Physics of Fluids* **21**(10), 101901.

Choi, J., Xia, G., Tawhai, M. H., Hoffman, E. A. and Lin, C.-L. (2010), 'Numerical study of high-frequency oscillatory air flow and convective mixing in a ct-based human airway model', *Annals of Biomedical Engineering* **38**(12), 3550–3571.

Cui, X. and Gutheil, E. (2017), 'Three-dimensional unsteady large eddy simulation of the vortex structures and the mono-disperse particle dispersion in the idealized human upper respiratory system', *Journal of Aerosol Science* **114**, 195–208.

Darquenne, C., Paiva, M. and Prisk, G. K. (2000), 'Effect of gravity on aerosol dispersion and deposition in the human lung after periods of breath holding', *Journal of Applied Physiology* **89**(5), 1787–1792.

Dhami, P. S., Chopra, G. and Shrivastava, H. (2015), *A Textbook of Biology*, Vol. 101, Pradeep Publications.

Dinesh, T., Gaur, G., Sharma, V., Madanmohan, T., Kumar, K. H. and Bhavanani, A. (2015), 'Comparative effect of 12 weeks of slow and fast pranayama training on pulmonary function in young, healthy volunteers: A randomized controlled trial', *International Journal of Yoga* **8**(1), 22.

Doorly, D., Taylor, D. and Schroter, R. (2008), 'Mechanics of airflow in the human nasal airways', *Respiratory Physiology & Neurobiology* **163**(1-3), 100–110.

Eichenholz, A. (1965), 'Respiratory alkalosis', *Archives of Internal Medicine* **116**(5), 699–708.

Elcner, J., Lizal, F., Jedelsky, J., Jicha, M. and Chovancova, M. (2016), 'Numerical investigation of inspiratory airflow in a realistic model of the human tracheobronchial airways and a comparison with experimental results', *Biomechanics and Modeling in Mechanobiology* **15**(2), 447–469.

Feng, Y., Kleinstreuer, C., Castro, N. and Rostami, A. (2016), 'Computational transport, phase change and deposition analysis of inhaled multicomponent droplet–vapor mixtures in an idealized human upper lung model', *Journal of Aerosol Science* **96**, 96–123.

Feng, Y., Kleinstreuer, C. and Rostami, A. (2015), 'Evaporation and condensation of multicomponent electronic cigarette droplets and conventional cigarette smoke particles in an idealized G3-G6 triple bifurcating unit', *Journal of Aerosol Science* **80**, 58–74.

Fort, P., Farmer, C., Westerman, J., Johannigman, J., Beninati, W., Dolan, S. and Derdak, S. (1997), 'High-frequency oscillatory ventilation for adult respiratory distress syndrome-a pilot study', *Critical Care Medicine* **25**(6), 937–947.

Fredberg, J. J., Keefe, D. H., Glass, G. M., Castile, R. G. and 3rd, I. D. F. (1984), 'Alveolar pressure nonhomogeneity during small-amplitude high-frequency oscillation', *Journal of Applied Physiology* **57**(3), 788–800.

Frederix, E., Kuczaj, A. K., Nordlund, M., Bělka, M., Lizal, F., Jedelskỳ, J., Elcner, J., Jícha, M. and Geurts, B. (2018), 'Simulation of size-dependent aerosol deposition in a realistic model of the upper human airways', *Journal of Aerosol Science* **115**, 29–45.

Gaddam, M. G. and Santhanakrishnan, A. (2021), 'Effects of varying inhalation duration and respiratory rate on human airway flow', *Fluids* **6**(6), 221.

Gemci, T., Ponyavin, V., Chen, Y., Chen, H. and Collins, R. (2008), 'Computational model of airflow in upper 17 generations of human respiratory tract', *Journal of Biomechanics* **41**(9), 2047–2054.

Gilbert, C. (2014), 'Chapter 5-interaction of psychological and emotional variables with breathing dysfunction'.

Gregoriano, C., Dieterle, T., Breitenstein, A.-L., Dürr, S., Baum, A., Maier, S., Arnet, I., Hersberger, K. E. and Leuppi, J. D. (2018), 'Use and inhalation technique of inhaled

medication in patients with asthma and copd: data from a randomized controlled trial', *Respiratory Research* **19**(1), 1–15.

Grimby, G. and Stiksa, J. (1970), 'Flow-volume curves and breathing patterns during exercise in patients with obstructive lung disease', *Scandinavian Journal of Clinical and Laboratory Investigation* **25**(3), 303–313.

Große, S., Schröder, W., Klaas, M., Klöckner, A. and Roggenkamp, J. (2007), 'Time resolved analysis of steady and oscillating flow in the upper human airways', *Experiments in Fluids* **42**(6), 955–970.

Grotberg, J. B. (2001), 'Respiratory fluid mechanics and transport processes', *Annual Review of Biomedical Engineering* **3**(1), 421–457.

Haghnegahdar, A., Feng, Y., Chen, X. and Lin, J. (2018), 'Computational analysis of deposition and translocation of inhaled nicotine and acrolein in the human body with e-cigarette puffing topographies', *Aerosol Science and Technology* **52**(5), 483–493.

Hakked, C. S., Balakrishnan, R. and Krishnamurthy, M. N. (2017), 'Yogic breathing practices improve lung functions of competitive young swimmers', *Journal of Ayurveda and Integrative Medicine* **8**(2), 99–104.

Han, B., Hirahara, H. and Yoshizaki, S. (2016), 'Streaming caused by oscillatory flow in peripheral airways of human lung', *Open Journal of Fluid Dynamics* **6**(3), 242–261.

Hofmann, W., Balásházy, I. and Koblinger, L. (1995), 'The effect of gravity on particle deposition patterns in bronchial airway bifurcations', *Journal of Aerosol Science* **26**(7), 1161–1168.

Holsbeke, C. S. V., Verhulst, S. L., Vos, W. G., Backer, J. W. D., Vinchurkar, S. C., Verdonck, P. R., van Doorn, J. W. D., Nadjmi, N. and Backer, W. A. D. (2014), 'Change in upper airway geometry between upright and supine position during tidal nasal breathing', *Journal of Aerosol Medicine and Pulmonary Drug Delivery* **27**(1), 51–57.

Horsfield, K., Dart, G., Olson, D. E., Filley, G. F. and Cumming, G. (1971), 'Models of the human bronchial tree.', *Journal of Applied Physiology* **31**(2), 207–217.

Imai, Y., Miki, T., Ishikawa, T., Aoki, T. and Yamaguchi, T. (2012), 'Deposition of micrometer particles in pulmonary airways during inhalation and breath holding', *Journal of Biomechanics* **45**(10), 1809–1815.

Islam, M. S., Saha, S. C., Sauret, E., Gemci, T. and Gu, Y. (2017), 'Pulmonary aerosol transport and deposition analysis in upper 17 generations of the human respiratory tract', *Journal of Aerosol Science* **108**, 29–43.

Jafari, S., Arabalibeik, H. and Agin, K. (2010), Classification of normal and abnormal respiration patterns using flow volume curve and neural network, *in* 'Health Informatics and Bioinformatics (HIBIT), 2010 5th International Symposium On', IEEE, pp. 110–113.

Jalal, S., Nemes, A., Van de Moortele, T., Schmitter, S. and Coletti, F. (2016), 'Three-dimensional inspiratory flow in a double bifurcation airway model', *Experiments in Fluids* **57**(9), 148.

Jalal, S., Van de Moortele, T., Amili, O. and Coletti, F. (2020), 'Steady and oscillatory flow in the human bronchial tree', *Physical Review Fluids* **5**(6), 063101.

Jalal, S., Van de Moortele, T., Nemes, A., Amili, O. and Coletti, F. (2018), 'Three-dimensional steady and oscillatory flow in a double bifurcation airway model', *Physical Review Fluids* **3**(10), 103101.

Jan, D. L., Shapiro, A. H. and Kamm, R. D. (1989), 'Some features of oscillatory flow in a model bifurcation', *Journal of Applied Physiology* **67**(1), 147–159.

Kaminsky, D. A., Guntupalli, K. K., Lippmann, J., Burns, S. M., Brock, M. A., Skelly, J., DeSarno, M., Pecott-Grimm, H., Mohsin, A., LaRock-McMahon, C. et al. (2017),

'Effect of yoga breathing (pranayama) on exercise tolerance in patients with chronic obstructive pulmonary disease: a randomized, controlled trial', *The Journal of Alternative and Complementary Medicine* **23**(9), 696–704.

Kleinstreuer, C. and Feng, Y. (2013*a*), 'Computational analysis of non-spherical particle transport and deposition in shear flow with application to lung aerosol dynamics—a review', *Journal of Biomechanical Engineering* **135**(2).

Kleinstreuer, C. and Feng, Y. (2013*b*), 'Lung deposition analyses of inhaled toxic aerosols in conventional and less harmful cigarette smoke: a review', *International Journal of Environmental Research and Public Health* **10**(9), 4454–4485.

Kleinstreuer, C., Feng, Y. and Childress, E. (2014), 'Drug-targeting methodologies with applications: A review', *World Journal of Clinical Cases: WJCC* **2**(12), 742.

Kleinstreuer, C. and Zhang, Z. (2010), 'Airflow and particle transport in the human respiratory system', *Annual Review of Fluid Mechanics* **42**, 301–334.

Kleinstreuer, C., Zhang, Z. and Li, Z. (2008), 'Modeling airflow and particle transport/deposition in pulmonary airways', *Respiratory Physiology & Neurobiology* **163**(1-3), 128–138.

Kolanjiyil, A. V. and Kleinstreuer, C. (2017), 'Computational analysis of aerosol-dynamics in a human whole-lung airway model', *Journal of Aerosol Science* **114**, 301–316.

Kondam, A. G., Nagadeepa, W., Jagan, N., Jyothinath, K., Suresh, M. and Chandrasekhar, M. (2017), 'The effect of yoga in improved cognitive functions in medical students: A comparative study', *National Journal of Physiology, Pharmacy and Pharmacology* **7**(1), 38.

Kondam, A., Suresh, M., Netaji, K. N. and Chandrasekhar, M. (2020), 'A comparative study on effect of pranayama and suryanamaskar yogic exercise on static spirometry values in normal young healthy individuals'.

Kraut, J. A. and Madias, N. E. (2010), 'Metabolic acidosis: pathophysiology, diagnosis and management', *Nature Reviews Nephrology* **6**(5), 274.

Lin, C.-L., Tawhai, M. H., McLennan, G. and Hoffman, E. A. (2007), 'Characteristics of the turbulent laryngeal jet and its effect on airflow in the human intra-thoracic airways', *Respiratory Physiology & Neurobiology* **157**(2-3), 295–309.

Liu, Y., Johnson, M. R., Matida, E. A., Kherani, S. and Marsan, J. (2009), 'Creation of a standardized geometry of the human nasal cavity', *Journal of Applied Physiology* **106**(3), 784–795.

Liu, Y., So, R. and Zhang, C. (2003), 'Modeling the bifurcating flow in an asymmetric human lung airway', *Journal of Biomechanics* **36**(7), 951–959.

Lízal, F., Elcner, J., Jedelskỳ, J. and Jícha, M. (2010), 'Experimental study of aerosol deposition in a realistic lung model'.

Lizal, F., Jedelsky, J., Lippay, J., Halasova, T., Mravec, F. and Jicha, M. (2012), Aerosol transport in a model of human lungs, *in* 'EPJ Web of Conferences', Vol. 25, EDP Sciences, p. 01050.

Lizal, F., Jedelsky, J., Morgan, K., Bauer, K., Llop, J., Cossio, U., Kassinos, S., Verbanck, S., Ruiz-Cabello, J., Santos, A. et al. (2018), 'Experimental methods for flow and aerosol measurements in human airways and their replicas', *European Journal of Pharmaceutical Sciences* **113**, 95–131.

Loring, S. H., Mead, J. and Waggener, T. B. (1990), 'Determinants of breathing frequency during walking', *Respiration Physiology* **82**(2), 177–188.

Lunkenheimer, P. P., Rafflenebell, W., Keller, H., Frank, I., DICHUT, H. H. and Fuhrmann, C. (1972), 'Application of transtracheal pressure oscillations as a modification of "diffusion respiration"', *BJA: British Journal of Anaesthesia* **44**(6), 627–627.

Ma, B. and Lutchen, K. R. (2009), 'Cfd simulation of aerosol deposition in an anatomically based human large–medium airway model', *Annals of Biomedical Engineering* **37**(2), 271.

Meenakshi, S. (2017), 'Impact of yoga therapy on anxiety and depression', *PULSE* **130**, 115.

Muktibodhananda, S. (2002), 'Hatha yoga pradipika: Light on hatha yoga', *Bihar School of Yoga, India* pp. 202–205.

Neves, I., Redondo, M., Cunha, R., Pereira, J. M., Magalhães, A., Fernandes, G. et al. (2015), 'Influence of emphysema distribution on pulmonary function parameters in copd patients', *Jornal Brasileiro de Pneumologia* **41**(6), 489–495.

Nicolaou, L. and Zaki, T. (2016), 'Characterization of aerosol stokes number in 90° bends and idealized extrathoracic airways', *Journal of Aerosol Science* **102**, 105–127.

Nowak, N., Kakade, P. P. and Annapragada, A. V. (2003), 'Computational fluid dynamics simulation of airflow and aerosol deposition in human lungs', *Annals of Biomedical Engineering* **31**(4), 374–390.

Ott, L. (1912), 'The clinical significance of abnormal respiration and deglutition click or fremitus; the pneumonic-respiration-pause-cycle', *American Journal of Diseases of Children* **4**(1), 7–12.

Panwar, S., Chourishi, A. and Makwana, J. (2012), 'Effect of pranayama (yoga) on pulmonary function test of young healthy students', *International Journal of Pharma and Bio Sciences* **3**(4), 12–6.

Papazian, L., Gainnier, M., Marin, V., Donati, S., Arnal, J.-M., Demory, D., Roch, A., Forel, J.-M., Bongrand, P., Brégeon, F. et al. (2005), 'Comparison of prone positioning and high-frequency oscillatory ventilation in patients with acute respiratory distress syndrome', *Critical Care Medicine* **33**(10), 2162–2171.

Patton, J. S. and Byron, P. R. (2007), 'Inhaling medicines: delivering drugs to the body through the lungs', *Nature Reviews Drug Discovery* **6**(1), 67.

Pedley, T., Schroter, R. and Sudlow, M. (1971), 'Flow and pressure drop in systems of repeatedly branching tubes', *Journal of Fluid Mechanics* **46**(2), 365–383.

Qi, S., Zhang, B., Teng, Y., Li, J., Yue, Y., Kang, Y. and Qian, W. (2017), 'Transient dynamics simulation of airflow in a ct-scanned human airway tree: more or fewer terminal bronchi?', *Computational and Mathematical Methods in Medicine* **2017**.

Rahimi-Gorji, M., Gorji, T. B. and Gorji-Bandpy, M. (2016), 'Details of regional particle deposition and airflow structures in a realistic model of human tracheobronchial airways: two-phase flow simulation', *Computers in Biology and Medicine* **74**, 1–17.

Ramuzat, A. and Riethmuller, M. (2002), Piv investigation of oscillating flows within a 3d lung multiple bifurcations model, *in* '11th International Symposium on Applications of Laser Techniques to Fluid Flows, Lisbon, Portugal, July', Citeseer, pp. 8–11.

Reddy, L. R., Sreehari, P. and Khan, M. I. (2015), 'Effect of yogic exercises (pranayama) on pulmonary function tests', *Journal of Contemporary Medicine and Dentistry* **3**(1).

Russo, J., Robinson, R. and Oldham, M. J. (2008), 'Effects of cartilage rings on airflow and particle deposition in the trachea and main bronchi', *Medical Engineering & Physics* **30**(5), 581–589.

Saoji, A. A., Raghavendra, B. and Manjunath, N. (2019), 'Effects of yogic breath regulation: A narrative review of scientific evidence', *Journal of Ayurveda and Integrative Medicine* **10**(1), 50–58.

Segal, R. A., Kepler, G. M. and Kimbell, J. S. (2008), 'Effects of differences in nasal anatomy on airflow distribution: a comparison of four individuals at rest', *Annals of Biomedical Engineering* **36**(11), 1870–1882.

Shanholtz, C. and Brower, R. (1994), 'Should inverse ratio ventilation be used in adult respiratory distress syndrome?', *American Journal of Respiratory and Critical Care Medicine* **149**(5), 1354–1358.

Silverthorn, D. (2015), *Human Physiology: An Integrated Approach, Global Edition*, Pearson Education Limited.

Soni, B. and Aliabadi, S. (2013), 'Large-scale cfd simulations of airflow and particle deposition in lung airway', *Computers & Fluids* **88**, 804–812.

Sonne, L. J. and Davis, J. A. (1982), 'Increased exercise performance in patients with severe copd following inspiratory resistive training', *Chest* **81**(4), 436–439.

Soodt, T., Pott, D., Klaas, M. and Schröder, W. (2013), 'Analysis of basic flow regimes in a human airway model by stereo-scanning piv', *Experiments in Fluids* **54**(6), 1562.

Soodt, T., Schröder, F., Klaas, M., van Overbrüggen, T. and Schröder, W. (2011), 'Experimental investigation of the transitional bronchial velocity distribution using stereo scanning piv', *Experiments in Fluids* **52**, 709–718.

Stancak Jr, A., Kuna, M., Vishnudevananda, S., Dostalek, C. et al. (1991), 'Kapalabhati–yogic cleansing exercise. i. cardiovascular and respiratory changes.', *Homeostasis in Health and Disease: International journal devoted to integrative brain functions and homeostatic systems* **33**(3), 126–134.

Stylianou, F. S., Sznitman, J. and Kassinos, S. C. (2016), 'Direct numerical simulation of particle laden flow in a human airway bifurcation model', *International Journal of Heat and Fluid Flow* **61**, 677–710.

Taimni, I. K. (1961), *The science of yoga*, Quest Books.

Tiller, J., Pain, M. and Biddle, N. (1987), 'Anxiety disorder and perception of inspiratory resistive loads', *Chest* **91**(4), 547–551.

Tsuda, A., Henry, F. S. and Butler, J. P. (2013), 'Particle transport and deposition: basic physics of particle kinetics', *Comprehensive Physiology* **3**(4), 1437.

Tu, J., Inthavong, K. and Ahmadi, G. (2012), *Computational fluid and particle dynamics in the human respiratory system*, Springer Science & Business Media.

Varnholt, V., Lasch, P., Suske, G., Kachel, W. and Brands, W. (1992), 'High frequency oscillatory ventilation and extracorporeal membrane oxygenation in severe persistent pulmonary hypertension of the newborn', *European Journal of Pediatrics* **151**(10), 769–774.

Wall, W. A. and Rabczuk, T. (2008), 'Fluid-structure interaction in lower airways of ct-based lung geometries', *Int. J. Numer. Methods Fluids* **57**, 653–675.

Walsh, J. H., Maddison, K. J., Platt, P. R., Hillman, D. R. and Eastwood, P. R. (2008), 'Influence of head extension, flexion, and rotation on collapsibility of the passive upper airway', *Sleep* **31**(10), 1440–1447.

Weibel, E. R., Cournand, A. F. and Richards, D. W. (1963), *Morphometry of the human lung*, Vol. 1, Springer.

Wen, J., Inthavong, K., Tu, J. and Wang, S. (2008), 'Numerical simulations for detailed airflow dynamics in a human nasal cavity', *Respiratory Physiology & Neurobiology* **161**(2), 125–135.

Whited, L. and Graham, D. D. (2019), 'Abnormal respirations'.

Yang, M.-C., Hsu, J.-F., Hsiao, H.-F., Yang, L.-Y., Pan, Y.-B., Lai, M.-Y., Chu, S.-M., Huang, H.-R., Chiang, M.-C., Fu, R.-H. et al. (2020), 'Use of high frequency oscillatory ventilator in neonates with respiratory failure: the clinical practice in taiwan and early multimodal outcome prediction', *Scientific Reports* **10**(1), 1–9.

Zhang, Y. and Finlay, W. H. (2005), 'Measurement of the effect of cartilaginous rings on particle deposition in a proximal lung bifurcation model', *Aerosol Science and Technology* **39**(5), 394–399.

Zhang, Z. and Kleinstreuer, C. (2002), 'Transient airflow structures and particle transport in a sequentially branching lung airway model', *Physics of Fluids* **14**(2), 862–880.

Zhang, Z. and Kleinstreuer, C. (2011), 'Computational analysis of airflow and nanoparticle deposition in a combined nasal–oral–tracheobronchial airway model', *Journal of Aerosol Science* **42**(3), 174–194.

Zhang, Z., Kleinstreuer, C. and Kim, C. S. (2009), 'Comparison of analytical and cfd models with regard to micron particle deposition in a human 16-generation tracheobronchial airway model', *Journal of Aerosol Science* **40**(1), 16–28.

APPENDICES

DESCRIPTION OF THE HUMAN RESPIRATORY SYSTEM

Human respiratory system (Fig.A.5) consists of extra-thoracic region (oral and nasal airways), tracheobronchial and alveolar regions. Gas exchange is the primary function of respiratory system. Respiration consists of inspiration of oxygen rich air and exhalation of carbon-di-oxide rich air. Functionally respiratory system is a passage for inhaled air into deep lung system. Human airways consists of nasal, pharynx, larynx, and tracheobronchial tree.

A.1 Nasal

Anatomy: Human nose differs from person to person based on race, ethnic groups, etc. Ideally, structure of nose divided into external portion named nose, and internal portions are nasal cavities. Nose is made of bony section (consists of pair of nasal bones sitting side to side) at the superior location (superior location includes dorsal, cephalic and posterior) and with a cartilaginous section on the inferior side (locations include anterior and caudal portions). Air enters through openings of nose called nostrils and these are separated through nasal septum. Air then passes through anterior nasal valve consisting of constricted cross sectional area and enters into main nasal passage. Choanae at the end of the nasal cavity helps the inhaled air to enter into the nasopharynx.

Physiology: Nose and Nasal passage provide a passage to the inhaled air to lungs. During this, air is filtered from the foreign particles and is humidified. Also, airflow is asymmetrical in nostrils which is due to swelling of cavernous tissue. A flow rate of 24 L/min was observed in the middle to inferior main passage with laminar flow and no proper details were revealed in the experiments so far Doorly et al. (2008).

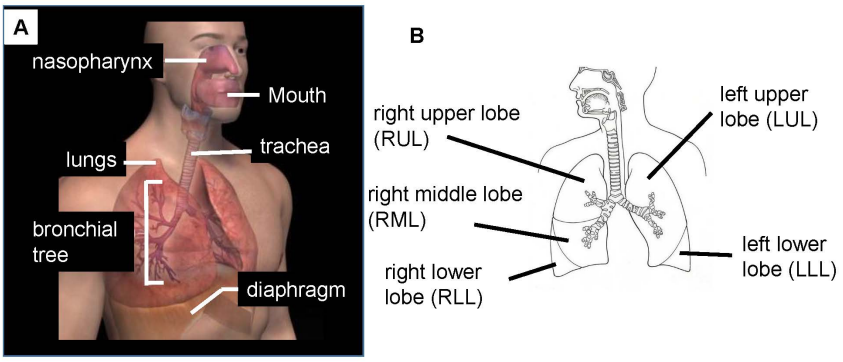

Figure A.5: A) Human respiratory system B) Lobes in lungs (labelled).

A.2 Pharynx

Anatomy: Pharynx is tube like structure connecting the nasal and oral cavities to larynx and oesophagus. Structurally this region is divided into nasopharynx, oropharynx and laryngopharynx.

Physiology: Pharynx serves as a passage for both digestive and respiratory system. The food is directed to oesophagus while the air is directed to larynx by controlling epiglottis (an elastic tissue acts like a lid to cover the trachea during food passage).

A.3 Larynx

Anatomy: Larynx consists of three single laryngeal cartilages, three paired laryngeal cartilages connected by membranes and ligaments. Larynx hold the vocal cords and it serves as a guard in transmitting air from pharynx to trachea. Airway cavity of larynx extends from triangular shaped inlet at the pharynx to circular shaped at the trachea. Interiors of larynx is made up of epithelium tissue with ciliated columnar directing mucus to pharynx through muco-ciliary action.

Physiology: Larynx helps to remove the foreign particles due to presence of mucus and humidify the inhaled air. If any items such as food particles enters into respiratory system then larynx helps in cough reflex and prevent particle in entering into lungs.

A.4 Tracheobronchial tree

Trachea is a hollow tube with average diameter of 18 mm for male while slightly smaller for females. This trachea divides into main bronchi or two branches with different diameters, namely left bronchus and right bronchus. Each bronchus leads into lung and divides into branches. Left bronchus divide into two lobular bronchi, Left upper lobe (LUL) and left lower lobe (LLL), and right bronchus divides into three lobular bronchi, right lower lobe (RLL), right middle lobe (RML) and right upper lobe (RUL).

Trachea was named as Generation number 0, first bifurcation branches as G1, next branches to be G2 and so on up to G23. Based on functional view- point, respiratory system consists of conducting and respiratory zones. Conducting zones include G0 through G16, while the respiratory zones include G17 through G23. Gas exchange takes place in the respiratory zone [Silverthorn (2015)].

'C' shaped cartilaginous rings about 15-20 are present on the trachea and they are connected by muscular membrane. Mechanical properties of this tracheal structure effects the airflow properties. A coat of mucus is found on the inner walls of airway. Mucus layer is found up to G16 and it moves outward or in direction of exhalation. This mucus layer acts as a primary protection layer and protects the airway preventing deposition of toxic materials and pathogens. Cilia present beneath the mucus layer drives the mucus against gravitational direction. In a healthy subject, the mucus layer thickness is around 0.5-1 mm and it moves at rate of 0.05 mm/min. Increase in mucus layers results in diseased conditions such as asthma, bronchitis,and emphysema.

A.5 Breathing mechanics

During inhalation, the muscles in the thorax pull the anterior end of each rib outward causing increase in lung volume. During this, the pressure inside the lungs decreases relative to the outside atmospheric pressure causing air to enter into lungs. During exhalation, the lung and ribs reaches equilibrium position pressurizing air inside the lung and pushing the air out.

Lung is measured in different lung volumes. Lung volumes are generally measured using spirometer, and its capacity is inferred from the measurements. Lung volumes helps to calculate the flow rates in experiments. There are 4 Lung volumes and 4 lung capacities to define the lung space.

Lung volumes:

1. Tidal volume (TV) is defined as total amount of air inhaled and exhaled during quiet breathing.
2. Inspiratory Reserve Volume (IRV) is defined as maximum volume that can be inhaled after tidal volume
3. Expiratory Reserve Volume (ERV) is defined as maximum volume that can be exhaled after tidal volume.
4. Residual Volume(RV) is the amount of volume left in the lungs after maximum expiration.
5. Dead Volume (DV) is defined as air volume that remains in the conducting zone. This portion of lung volume does not contribute to gas exchange.

Lung capacities:

1. Functional Residual Capacity (FRC) is the volume of air left that can be exhaled after nomal exhalation.
2. Inspiratory Capacity (IC) is the volume of maximum inhalation.
3. Vital Capacity (VC) is the volume of maximum inhalation and exhalation.
4. Total Lung Capacity (TLC) is maximum volume in the lungs.

VITA

Manikantam G. Gaddam

Candidate for the Degree of

Doctor of Philosophy

Dissertation: FLOW CHARACTERIZATION INSIDE AIRWAYS WITH UNSTEADY BREATHING PATTERNS

Major Field: Mechanical and Aerospace Engineering

Biographical:

Personal Data: Born in Hyderabad, Telangana, India in March 1993.

Education:
Completed the requirements for the degree of Doctor of Philosophy with a major in Mechanical and Aerospace Engineering at Oklahoma State University in July 2021.
Received a Masters of Science in Mechanical and Aerospace Engineering at Oklahoma State University in Dec 2016.
Received a Bachelors of Engineering in Mechanical Engineering at University College of Engineering, Osmania University in May 2010.

Experience:
Graduate Teaching Assistant Aug 2014 – May 2021
Oklahoma State University
Graduate Research Assistant Dec 2014 – May 2021
Oklahoma State University

Professional Membership:
American Physical Society (APS)
International Society of Automation (ISA)
Association for the Sciences of Limnology and Oceanography (ASLO)
Society for Integrative and Comparative Biology (SICB)